## ABSTRACT

WANG, JIUYANG. Scanning Probe Microscopy of Intrinsic and Extrinsic Disorder in Organic Semiconductors. (Under the direction of Dr. Daniel Dougherty).

This dissertation is devoted to develop an understanding of intrinsic and extrinsic disorder, both structural and electronic, in organic semiconductors. Atomic force microscopy (AFM) and conducting atomic force microscopy (CAFM) were used to study the percolation characteristics of charge transport in disordered poly-3-hexylythiophene (P3HT): fullerene-$C_{60}$ heterojunction thin films. Organic semiconductors N,N'-Di-[(1-naphthyl)- N,N'-diphenyl]-1,1'-biphenyl)-4,4'-diamine (α-NPD) deposited on Au(111) and α-sexithiophene (α-6T) on $C_{60}$/Au(111) substrates were studied by scanning tunneling microscopy (STM) and scanning tunneling spectroscopy (STS) to investigate the intrinsic and extrinsic disorder, respectively. The observations can provide insights for the working principle of organic devices and help to improve the performance of future organic electronic applications.

Mixed films of P3HT and $C_{60}$ were grown by vacuum codeposition. Films were characterized by ultraviolet-visible absorption spectroscopy, AFM, and CAFM. Absorption spectra show evidence for diminished crystallinity in mixed films. CAFM measurements show small local currents and only a limited number of charge percolation pathways through the film, especially when compared with related solution-processed bulk heterojunctions.

α-NPD thin films with different conformations grown on Au(111) substrate were studied by STM and STS. Three-lobe, windmill, ordered narrow-single-row and broad-single-row, and disordered patterns have been explored. Models of molecule conformation for these pattern have also been given. By utilizing STS, highest occupied molecular orbital (HOMO) level of disordered structures shifts to higher binding energy than the HOMO level

of ordered broad-single-row structures has been observed, which can be explained by the change of the overlap of π states of the backbone and phenyl/naphthyl groups.

Lastly, STM and STS measurements were carried out on α-6T films grown on $C_{60}$/Au(111) substrates. The sexithiophene molecules adopt an upright orientation on this substrate with a unit cell that reflects both bulk-like α-6T packing and $C_{60}$ substrate templating effects. Random apparent height variations in these films are assigned as molecular sliding defects but are observed to have negligible electronic impact on the energy of HOMO. However, the HOMO is observed to vary significantly in response to random changes in probe tip, implying that the origin of electronic disorder in this system is extrinsic to the molecular film.

Scanning Probe Microscopy of Intrinsic and Extrinsic Disorder in Organic Semiconductors

by
Jiuyang Wang

A dissertation submitted to the Graduate Faculty of
North Carolina State University
in partial fulfillment of the
requirements for the degree of
Doctor of Philosophy

Physics

Raleigh, North Carolina

2014

APPROVED BY:

| | |
|---|---|
| _____ | _____ |
| Daniel Dougherty<br>Committee Chair | Harald Ade |
| _____ | _____ |
| Laura Clarke | Christopher Roland |
| _____ | |
| Charles Balik | |

## DEDICATION

This dissertation is dedicated to my parents

Ziwei Wang

Baozhu Liu

## BIOGRAPHY

Jiuyang Wang was born in Zhengzhou, Henan Province, P.R.China on May 20th, 1984. He spent his childhood in hometown until he enrolled into the department of physics at University of Science and Technology of China (USTC) in Hefei, Anhui Province, from September 2003. In June 2007, Jiuyang graduated from USTC and received his Bachelor of Science degree. Jiuyang enrolled in the department of physics at North Carolina State University (NCSU) as a Ph.D. student from August 2007. He joined Daniel Dougherty's group since August 2009, and worked on conducting AFM of organic semiconductor films and STM/STS study on organic semiconductors.

## ACKNOWLEDGMENTS

First of all, I would like to thank my research advisor, Dr. Daniel Dougherty. Dan has such a solid, broad and deep understanding of physics, and he is very pleased and patient to transfer me these knowledge and attitude for doing research. He is so responsible and devoted to tutor my research work and always gave me warm encouragements when I came across difficulties. His optimism and passion greatly influence me and I am so grateful to be under Dan' direction during my graduate student years.

I would also like to thank my committee members, Dr. Harald Ade, Dr. Laura Clarke, Dr. Christopher Roland and Dr. Charles Balik, for their support and time helping me with my work.

Further I would like to thank the other members in Dougherty group who provide me a free and warm atmosphere for my research. I would like to thank Alex Pronschinske, who is so warm-hearted to help me both in academic and life areas. His Python programs for analyzing spectra data is amazing and very helpful for my research. I would like to thank Zhengang Wang, who gave me so many useful suggestions in both research and future career life. Great thanks also to my other colleagues, Terry McAfee , Jingying Wang, Tianshuai Guan and Andrew Hewitt, without your support, my work would not have been possible.

Lastly, I would like to thank my family and friends. I would like to give my inmost thanks to my parents, Ziwei Wang and Baozhu Liu. They are not well educated, worked in low positions, but they gave me all what they have. My phone call to home each week is the power for me to overcome every difficulty and reach where I am . I would also like to thank my two sequential roommates, Chunda Zhou and Hao Lu. It is so joyful for us to play games,

cook delicious food and chat together. Great thanks to the group members Shu Xu and Ruoyi Qiu, in the QQ chat group “Scientific Outlook on Development”, even though only us three inside, this chat group provides me a lot of laughs and release from daily busy work. I would like to thank the members of “A&C Market Gang”, Shuming Hu and Bikan Tan, who always carpool with me to have lunch in A&C Market. Not only the nice traditional Chinese food, but also the pleasuring talk gave me a wonderful lunch time break. I would also like to thank my previous high school classmate and good friend, Wenzhou Li, even though we are at different universities in USA and different majors, he always encourages me, provides me useful ideas and gives me warm hands when I need them. At last I would like to thank my girlfriend, thanks to you not showing up during my Ph.D. period, I can devote my full strength to research. Without your cooperation, I cannot make this dissertation happen. However, hope to see you soon.

## TABLE OF CONTENTS

## LIST OF FIGURES

# Chapter 1

# Introduction, Background and Motivation for Organic Electronics and Surface Science

## 1.1 State-of the-Art Organic Electronics---small molecules and polymers

### 1.1.1 History

The first example of a macroscopic electrical effect in organic materials is electroluminescence, first observed in molecular crystals during the 1960s[1], which triggered intensive investigations by many researchers.

In 1977, Shirakawa et al. reported that polyacetylene conductivity increases markedly with exposed to chlorine, bromide or iodine vapor[2], and this discovery not only brought them the 2000 Nobel prize in chemistry "for the discovery and development of conductive polymers", but also attracted significant attention to conductive polymer research.

During the 1980s, the first organic light emitting diode (OLED) and organic photovoltaic (OPV) cell were invented by C.W.Tang[3,4]. Initial illustration of organic thin film transistors (OTFT) were also reported[5,6]. All this progress showed the possibility of utilizing organic semiconductors in electronics development and industrial production.

Nowadays, techniques of fabricating OTFTs are quite mature: top- and bottom-contact configurations (source and drain electrodes are above or below organic semiconducting layer) are widely used in OTFTs[7]; doped silicon with a thermally grown layer of $SiO_2$ (200-500nm thick) is commonly adopted as a substrate in the scientific research on OTFTs. Vacuum-deposition is a common technique for growing organic films in OTFTs, with the merit of allowing fabrication of flat and uniform organic semiconducting films[8]. With progress in molecular design and device fabrication, solution-processing methods were invented and utilized as an approach to establishing lost-cost processing[9,10], which has attracted more and more attention. A very high mobility (23.2 $cm^2 V^{-1}s^{-1}$) in solution-processed pentacene-based OTFT has been reported by Hwang et al.[11].

Another kind of FETs is single crystal based and shows great potential for revealing the basic charge transport mechanisms and limitations in organic electronic materials. Organic single crystal FETs were first fabricated using rubrene by Podzorov et al.[12] and single crystal FETs were subsequently fabricated with the acene-type organic molecules, pentacene and tetracene[13,14]. These FETs showed p-channel FET characteristics with mobilities higher than those of organic thin film FETs. Currently the highest mobility among organic single crystal FET is 94 $cm^2 V^{-1}s^{-1}$ on a pressure-sensitive organic superconductor $\kappa$-$(BEDT\text{-}TTF)_2Cu[N(CN)_2]Br$ reported by Kawasugi et al.[15].

Following Tang's 1% organic photovoltaic cell[4], there has been a lot of progress in the field of OPV's, where the possibility of low-cost processing compared to Si PVs is a major motivation. By incorporating new active layer materials and optimizing device architectures and morphologies, efficiencies of OPVs have reached a new height for both

small-molecule OPV and polymer-based OPV. The highest OPV efficiency by now is 12% reported by Heliatek in Jan 2013[16].

Since Kodak developed the first low voltage OLED using a bilayer structure[3], the OLED field has flourished and resulted in commercial viable display technologies. The Kido group has demonstrated the first white OLED by mixing of different colored emitters[17]. Thompson and co-workers have developed a platform for the synthesis of currently predominant Ir-based phosphors[18]. The Leo group has further doubled the device efficiency for white phosphorescent OLEDs (~ 90 lm/W)[19], which even surpassed that of the fluorescent tubes (~70 lm/W). Recently, the Lu group has developed a unique light out-coupling approach that can further boost the device efficiency, which leads to a record performance green OLED (~ 290 lm/W)[20].

### 1.1.2 Key Features of Organic Electronic Materials

Organic electronic materials can often be classified into two categories: Small molecules and Polymers. Small molecule indicates a molecule with a well-defined molecular weight. One famous example is Tris(8-hydroxyquinoline) aluminum (Alq3) (Figure 1.1 left), which is mostly used as an emissive material in OLED research[21]. In contrast, polymers are long-chain molecules consisting of a large number of molecular repeat units called monomers. For instance, the polymer poly(3-hexylthiophene) (P3HT) (Figure 1.1 right), plays an important role in organic photovoltaic cells as an electron donor material[22]. These materials often have strong optical absorption that makes them useful in dye materials, inks, and in more sophisticated optoelectronic devices.

Optical properties are generally dominated by the excitonic state formed by the Coulomb interaction between photoexcited electrons and holes[23]. The excitons are thought to be localized on one molecule, with a binding energy of typically 0.5 to 1 eV. This exciton binding energy is large compared to exciton binding in inorganic materials (e.g. Si, GaAs) and must be overcome to create a pair of independent positive and negative carriers in a photovoltaic device. The exciton can hop from molecule to molecule or from chain to chain, as well as along the polymer backbone in the case of polymers, until it either dissociates to generate a photocurrent or recombines to generate light or heat.

In addition to excitonic optical properties, the electrical transport properties of small molecules and polymers are quite unique. Depending on the degree of crystalline order, the charge transport in organic semiconductors can be divided into two categories: band or hopping transport. Band transport is usually observed in highly ordered molecular crystals at room temperature and the mobility can only reach 1 to 100 $cm^2\ V^{-1}s^{-1}$ [15,24]. The band transport mobility $\mu$ follows a power law dependence on temperature T[25]

$$\mu \propto T^{-n} \quad . \tag{1.1}$$

In the other case, the carrier transport mechanism in disordered organic semiconductors is described by hopping transport, which typically results in much smaller mobility values of $10^{-3}$ to $10^{-5}$ $cm^2\ V^{-1}s^{-1}$ [26,27]. The mobility $\mu$ will be not only related to temperature T, but also to applied electric field F, as shown by the empirical equation[28]

$$\mu(F,T) \propto \exp(-\Delta E / kT) \cdot \exp(\beta\sqrt{F} / kT), \tag{1.2}$$

Small molecules and polymers have similar optical and electronic properties, and their difference mainly resides in how thin film and devices are prepared. Small-molecule devices are usually fabricated by thermal evaporation in vacuum due to their poor solubility, to be introduced in chapter 2. On the other hand, polymer devices are typically processed from solution by spin-coating that takes advantage of the high solubility of many polymers.

### 1.1.3 Organic Electronic and Optoelectronic Devices

There are mainly three organic electronic devices being extensively studied and commercialized to take advantage of light weight, mechanically flexibility, low-cost fabrication and large area device production: Organic Light Emitting Diodes (OLEDs), Organic Photovoltaic Devices (OPVs) and Organic Field Effect Transistors (OFETs), as shown in Figure 1.2 schematically.

The operation of OLEDs involves charge injection from a high-work-function anode (usually ITO) and a low-work-function cathode into the adjacent organic layers, transport of injected electrons and holes inside organic layers under the apparent electric field in opposite directions, recombination of them to generate excitons with a ratio of 25:75 for singlet excitons/triplet excitons[29]. Finally excitons deactivate by electron-hole recombination, in the process emitting light or generating heat. To achieve high efficiency for OLEDs, the ratio of injected electrons and holes $\gamma$ should be 1 ideally, in order to minimize electrical power losses. There are two physical parameters influencing $\gamma$, the injection barrier height and the charge carrier mobility. The injection barrier height is the difference in energy between the electrode Fermi level and the organic transport levels at the interface. For low working

voltages of OLEDs, the barriers need to be minimized to increase the current across this barrier in the injection-limited regime. Therefore, developing an understanding of organic/electrode interface energetics and rational methods for controlling injection barriers are quite important topics for organic electronics. These interfacial energetics are the primary topic of interest in several chapters of this thesis.

OPVs consist of a thin film of organic photoactive materials sandwiched between two metal electrodes. The processes of OPVs are just opposite to those of OLEDS, including sequentially (a) light absorption by organic materials to generate excitons, (b) diffusion of excitons to the interface of two different organic materials, (c) charge separation at the interface, (d) charge transport through organic materials and (e) charge collection at both electrodes. In step (b), specific requirements on the thin-film morphology are imposed to optimize desired diffusion of excitons towards an organic donor-acceptor interface. The typical exciton diffusion lengths in polymer films and disordered small molecules are in the range of a few nanometers or a few tens of nanometers. Consequently, the average domain size of donor or acceptor materials in organic heterojunctions should be on the length scale of the exciton diffusion lengths. The techniques to explore thin-film morphology, such as atomic force microscopy (AFM) and scanning tunneling microscopy (STM), will provide very useful information to guide thin-film fabrication for optimizing OPV morphology. In addition, step (e), charge collection also demand detailed characterization of metal-organic interface energetic as described above.

OFET's consist of source, drain, gate electrodes and an organic semiconductor as active channel element. When there is no voltage applied to the gate, only small current

flows between the source and drain electrodes; this state is called the "off" state. When there is a negative voltage applied at the gate electrode, hole carriers in the organic semiconductors will accumulate near the gate dielectric and charge will transport from the source to the drain electrode; this state is called the "on" state. Charge-carrier mobility is a crucial physical parameter for the function of OFETs. While carrier mobility generally increases with decreasing temperature in high quality organic single crystals, indicative of band-like transport, mobility increases for increasing temperatures in thin-film samples, where hopping transport prevails. This temperature dependence of mobility arises from the thermal activation that is required for each hopping event as can be seen in the first exponential factor in Eq. 1.2. Thus the structural details of thin films are the key to a qualitative understanding of transport in these organic molecular solids. Even band transport within single crystals can be hindered by charge-carrier trapping at structural defects, such as dislocations or grain boundaries. Moreover, the growth and structure of organic films is strongly dependent on the substrate[30,31]. Charge transport in OFETs is confined to the first few nanometers away from the gate insulators[32], so research should focus on understanding of the growth of the first several monolayers described in the following chapters of this thesis.

## 1.2 Electronic structures at the molecule-metal interface

As stated above, transport of charge carriers through interfaces is crucial to organic electronic and optoelectronic devices, which is controlled by the energetics of molecule-metal interfaces. In order to transfer charge carriers from a metal electrode into an active organic layer, charge carriers must move between metal energy bands and molecular orbitals.

Unlike the electronic bands of the metal, molecules have discrete energy orbitals. The highest occupied molecular orbital (HOMO) and the lowest unoccupied molecular orbital (LUMO), also known as the "frontier orbitals", are the molecular orbitals most relevant to charge transport. Electron affinity (EA) is the energy obtained by moving an electron from the vacuum into the LUMO level. The ionization energy (IE) is the energy needed to move an electron from HOMO level into vacuum. The transport gap $E_t$ of organic film is the difference of IE and EA. In the approximation where adding or removing charge does not result in any rearrangement of remaining electrons or nuclear positions in the molecule, this is simply the energy difference between HOMO and LUMO of the molecule. In reality, the HOMO and LUMO are ground state orbitals and charge injection processes create transiently ionized excited states of the molecule where electrons and sometimes nuclear positions change in response to added charge. However, in this thesis we will use the acronyms HOMO and LUMO to refer to the transport levels from which electrons have been extracted or added respectively.

The electron and hole injection barriers $\Phi_e$ and $\Phi_h$ correspond to the energy difference between Fermi level $E_F$ and LUMO and HOMO, respectively. The work function of the metal $\Phi_M$ is defined as the energy needed to move an electron from its Fermi level to the vacuum level just outside of the surface. All the energies defined above are shown in Figure 1.3.

The so-called common vacuum level (CVL) approximation has been used to predict the relative positions of electronic states at the metal/molecule interface, which dates back to Mott[33] and Schottky[34]. However, at metal-organic interfaces, the energy level alignment most

often fails to obey this CVL approximation, due to the "interface dipole shift" at the metal-organic interface[35,36] , as indicated by Δ shown in Figure 1.3. The origin of interface dipole could be the result of mutual actions of several physical mechanisms including:

1. The rearrangement of charge at the interface. Even somewhat weak interactions involve the redistribution of electron density within the molecule and within the nearby region of the metal[37].
2. "Pauli repulsion" induced suppression of metal electron density tails at the interface[38]. There is an electron "spill out" region outside the clean metal surface in vacuum and during the adsorption of a molecular layer the spill out region can be pushed back into the metal causing an interface dipole layer; this is known as "Pauli repulsion". Anytime a molecular film is deposited on a metal surface, Pauli repulsion will occur and the suppression of the metal's natural surface dipole will decrease the metal work function.
3. Permanent molecular dipoles[35,39]. The permanent dipole of molecules can change the intrinsic dipole layer of the metal electrode.
4. Chemical reaction between metal and organic molecules[40,41]. This is a special case of 1 and includes the formation of a covalent bond with surface atoms, which causes partial charge transfer from metal to molecules; ionization of the molecule leaving the counter charge on the metal; replacement of atoms of metal surface to create a new organometallic complex.

Another commonly-observed phenomenon that should be mentioned is the broadening of molecular orbitals due to electronic mixing with continuum metal bands. When molecules are coupled with a metal substrate, molecular states will tend to spill over into the metal, leading to overlap. This orbital mixing imparts some of the band-like character of the metal states to the previously energetically-localized molecular orbital. Alternately, this broadening effect could be explained from consideration of the uncertainty principle associated with the lifetime of a molecular orbital state in contact with a metal surface. At the interface between molecules and metal substrate, the electron from the molecule will quite easily scatter into the conductive metal substrate, which shortens the electron life time inside the molecular orbital. According to the uncertainty principle, the product of molecular state lifetime and the energy level broadening width should be a constant, so the shorter the lifetime, the broader the state's energy width.

## 1.3 Charge transport in disordered organic semiconductors

### 1.3.1 Hopping induced charge transport in disordered organic semiconductors

Common fabrication technologies of organic semiconductor materials, such as high vacuum vapor deposition of small molecule based materials or solution spin-cast deposition of polymers, often lead to a disordered, amorphous structure[42]. In such systems, with only a weak intermolecular interaction, injected electrons or holes reside on distinct molecular sites or on distinct conjugated segments(in the case of polymers). The charge transport will be due to hopping, i.e., to thermally assisted quantum-mechanical tunneling between the localized

sites. The hopping rate between sites i and j is usually depicted by Miller-Abrahams expression[43,44] :

$$W_{ij} = \nu_0 \exp(-2\gamma |R_{ij}|) \begin{cases} \exp\left(-\frac{(\varepsilon_j - \varepsilon_i)}{kT}\right) & \forall \varepsilon_j > \varepsilon_i \\ 1 & else \end{cases}, \quad (1.3)$$

where $\nu_0$ is the phonon vibration frequency (can be intuitively understood as the "jump-attempt" rate), in the range of tens of $ps^{-1}$, $\gamma$ is the inverse localization radius (the result of overlap integral of the wave functions assuming exponential decay with distance), about several $nm^{-1}$, $\varepsilon_i$ and $\varepsilon_j$ are energy levels of the two sites respectively, k is Boltzmann constant and $R_{ij}$ is the spatial distance between these two sites, approximately several nm. The hopping rate varies with hopping distance and the site energy difference. Also the hopping rate increases with increasing temperature, which agrees with experimental evidence for disordered molecular solids.

### 1.3.2 Percolation view for disordered organic semiconductor charge transport in 3D

As a result of the energetic disorder inside organic materials, the current density is not uniform but filamentary, which was first brought out by Ambegaokar et al.[45]. The basic idea is that when a charge moves from one side of the sample to the other, it would try to use the fastest route, similar to water percolating through dry land. This model has been revealed from various 3D studies, e.g., for systems with a uniform field and a uniform carrier density[46,47], in studies of injection from a metallic electrode[48] and in devices with two metallic electrodes with varying injection conditions[49,50]. The filamentary effect is strongest

at small fields, decreases with increasing field and vanishes at very high fields when almost all forward hops are "downhill" so that disorder in energy no longer affects the hopping rates[47,48]. As a consequence of the filamentary view, we can think of the sample as if it was divided into subunits or pathways. Each subunit is characterized by its local density of states (DOS) and consequently by a typical local charge velocity or mobility, so the current through a certain small area varies statistically. In chapter 3 of this thesis, we will use conducting AFM (CAFM) to visualize current percolation pathways through organic semiconductor films.

### 1.3.3 Injection-limited charge transport in disordered organic semiconductors

As stated in section 1.1.3, organic materials are widely used as charge-transport layers in devices, such as OLED's and OTFT's. The injection of charge from a metal electrode into the disordered organic layer is one crucial step in the performance of these devices. The electron injection barrier arises largely from a difference between work function of the electrode and LUMO level of the organic molecules. Similarly, the hole injection barrier will depend on a difference between work function of the electrode and HOMO level of the organic molecules.

Typically, transport over this interface barrier at a metal/semiconductor interface is analyzed using one of two theories. For very large barriers or at low temperatures, charge-carrier tunneling[51] is thought to dominate the process. On the other side, if injection is thermally active at room temperature, thermionic emission over the barrier is used to depict transport characteristics, commonly known as Richardson-Schottky model[52],

$$J \propto T^2 \exp[-\left(\Phi_B - \sqrt{eE/4\pi\varepsilon}\right)/kT], \tag{1.4}$$

where T is the temperature, $\Phi_B$ is the injection barrier, e is the electron charge, E is the applied electric field, ε is the dielectric constant and k is Boltzmann's constant. Experimental and numerical studies[53,54] show quantitative differences from the Richardson-Schottky model. The proportionality coefficient is generally bigger than that from Richardson-Schottky model and varies with disordering of the material.

Burin and Ratner proposed a new model [55] in which the injection will occur through a particular pathways at sufficiently high electric field, which lowers the energetic barrier between the metal Fermi energy and molecular levels of the organic molecules. By assuming a Gaussian distribution of random molecular transport levels, the current density J was shown to follow

$$J \propto e^{-\Delta/T} \exp\left(\frac{2\sqrt{2}}{3}\sqrt{\frac{w^2 eaE}{T^3}}\right), \tag{1.5}$$

where Δ is the injection barrier, T is the temperature, w is the width of the Gaussian distribution, e is the electron charge, *a* stands for intermolecular distance and E is the applied electric field. This model indicates that injection efficiency increases with increasing disorder due to the formation of the rare low energy pathways and carrier transport occurs mostly along these pathways at sufficiently high voltages.

Meanwhile, Baldo and Forrest proposed another model in which charge injection into disordered organic semiconductor is limited by interface[56]. In this model, resulting from randomness in the interface morphology and the localization of charge in molecular

materials, there will be a dipole layer at the interface between the metal electrode and organic semiconductor. This injection model can be thought as a two-step process. Initially charges are injected into a thin interface region where the distribution of energy sites is dramatically-broadened by the interface dipole, and lowered due to image charge effect. In the next step, charges will hop from the interfacial region into the disordered bulk transport states with a narrower distribution of generally higher energy. This second step is the most energetically costly injection event.

A major aspect of this thesis is the identification of disorder very close to metal-organic interfaces relevant to organic electronics. We will report scanned probe microscopy observations of disorder at the molecular scale and characterize the possible impacts of this disorder on local electronic structure. So far, in this chapter, we have primarily discussed macroscopic transport measurements that indicate the importance of disorder for transport and charge injection in organic electronic materials. The goal of this thesis is to begin to reveal the microscopic details that underpin such macroscopic effects.

## 1.4 Review of important metal/organic interface studies

As indicated in previous discussions, the metal/organic interface will play an important role in organic device performance. The energy level alignment between metal and organic materials, morphology at the interface will both determine the charge transport process between metal and organic molecules. The rest of this chapter will be dedicated to review some of the important surface science studies at the metal/organic interface.

Ultraviolet photoelectron spectroscopy (UPS) is a common technique for studying ionization energy, which is the binding energy of HOMO state and vacuum level. Ishii and Seki observed abrupt shifts of the vacuum level at all the interfaces between metals and various organic-semiconductors ranging from donor to acceptor by UPS [57]. These findings have clearly demonstrated the invalidity of the assumption of the alignment of the vacuum levels at organic/metal interface formed in ultrahigh vacuum. A. Kahn and coworkers used UPS and current-voltage measurements to investigate the impact of electrode contamination on the α-NPD/Au hole injection barrier[58]. They found that the hole barrier with the contaminated Au electrode was smaller than the clean one. This result is due to induced density of interface states and reduction of direct interaction between metal and molecules with contaminations. A. Kahn' group has also shown by UPS that the hole injection barrier at the interface between three conjugated organic materials (α-NPD, 6P and pentacene) deposited on PEDOT/PSS is drastically smaller than on Au, due to the reduction of the electronic surface dipole contribution to the metal work function by adsorbed molecules[59].

X-ray photoemission spectroscopy (XPS), also known as electron spectroscopy for chemical analysis (ESCA), is a surface-sensitive quantitative spectroscopic technique that measures the elemental composition, empirical formula, chemical state and electronic state of elements that exists within a material. Y.Gao et al. have used XPS to study the formation of metal/organic interfaces in organic electroluminescent devices[60]. Both Ca/OPV and OPV/Ca interfaces XPS studies confirmed the energy level bending and allowed them to deduce the energy level diagram near the interface. T.Chasse and coworkers also used XPS to

investigate the interface between CoPc and Au substrate[61]. The experimental data indicated a quite strong interaction between the organic molecules and the metallic substrate.

To determine the electron affinity of organic materials is more difficult than ionization energy which can be easily measured by UPS. The main method nowadays is inverse photoemission electron spectroscopy (IPES), which directs a well-collimated beam of electrons of a well-defined energy (<20eV) to the sample. These electrons are coupled to high-lying unoccupied states and decay to low-lying unoccupied states. The emitted photons in the decay process are detected and an energy spectrum of photon counts vs. incident electron energy is generated. By using IPES and UPS, A.Kahn's group has investigated the exciton binding energy of five different organic semiconductor materials (CuPc, PTCDA, α-6T, α-NPD and $Alq_3$), and they found the energy difference between HOMO and LUMO of condensed phase molecules is smaller than that of gas phase[62]. S.R.Forrest et al. also made a great contribution to measurement of LUMO of molecular organic semiconductors by using IPES. They compared the IPES data with the data determined from optical energy gaps, electrochemical reduction potentials and density function theory (DFT) calculations. They concluded that care must be taken to ensure that the lowest energy value of optical energy gap represents the appreciate HOMO-LUMO transition[63].

Two photon photoelectron spectroscopy (2PPE) is another technique for probing empty states in organic semiconductors. 2PPE is suited for the investigation of heterogeneous electron transfer, and good for strong electronic interaction between molecules and metal surfaces. M.Wolf and his coworkers have used 2PPE spectroscopy to investigate the energetic and lifetimes of the unoccupied electronic states of $C_6F_6$ adsorbed on Cu(111) as a

model system for electron transfer at organic/metal interfaces[64]. They found a pronounced lowering in the energetic position of the lowest unoccupied state, which was accompanied by a strong increase in its life time and a decrease in the effective electron mass.

In addition, scanning probe microscopy (SPM) is a technique contributing greatly to the study of molecule/ metal interface. Different from the averaged energy levels obtained from UPS, XPS, IPES and 2PPE methods, SPM can investigate the electronic structures of one certain nanoscale range area on the surface, even on a certain molecule. Furthermore, SPM can probe the morphology of organic films and molecular assemblies on metal substrate.

Specially, scanning tunneling spectroscopy (STS) implemented by scanning tunneling microscopy (STM) can directly measure energy gap of organic molecules on the metal substrate. The Hipps group has used STM to identify occupied and unoccupied orbital energy levels of CoPc and CoTPP submonolayer on Au(111)/mica substrates[65]. They identified the transient oxidation of Co $d_z^2$ orbital in STM dI/dV curves just negative of the 0V sample bias for both molecules. Nearly identical constant-current contours were observed over the central $Co^{2+}$ ions of CoTPP and CoPc, indicating that the attenuation of the $d_z^2$ orbital-mediated tunneling current induced by the structure of TPP relative to Pc was at most a factor of about 10. The orbital-mediated tunneling spectra of CoTPP and CoPc were distinctly different and allow these structurally similar species to be differentially identified.

STM and STS is a powerful tool to study the relation between organic conformations and corresponding electronic structures. For instance, to investigate influence of conformation on conductance of biphenyl-dithiol single-molecule contacts, T.Wandlowski et

al. have used STM-break-junction method to measure the conductance of a family of biphenyl-dithiol derivatives with conformationally fixed torsion angle[66]. They found the conductance depending on the torsion angle between two phenyl rings. Detailed calculations of transport based on DFT calculation and two level model (TLM) supported the experimental results.

To unveil both the morphology and electronic disorder at the organic/metal interface, STM and STS will also play an important role. By using STM, X.-Y.Zhu and his coworkers showed that shallow traps in vapor-deposited crystalline pentacene thin films were due to local defects resulting from the sliding of pentacene molecules along their long molecular axis, while two-dimensional crystalline packing was maintained[67]. Electronic structural calculations suggested that these sliding defects were shallow-charge traps with energies ≤ 100 meV above (below) the valence band maximum (conduction band minimum). D.B.Dougherty et al. found similar molecule sliding induced disorder later on pentacene: $C_{60}$ interface[68]. They suggested the long range pattern of periodic pentacene displacements relative to the substrate was the response to stress induced in the pentacene film by its interaction with the rigid $C_{60}$ support.

F.S.Tautz and cowokers also contributed to the study of disordered electronic structures of organic molecules on metal substrate. Up to ~1.0eV energy level shifts from molecule to molecule was revealed in highly ordered molecular semiconductor films of tetracene[69]. This final state effect could be traced back to the polarization energy in organic materials with complex unit cells, caused by a combination of different molecular

environments, the intrinsically anisotropic molecular polarizability, and the influence of the substrate.

To study organic films of thicknesses larger than a few layers, scanning tunneling microscopy is not applicable due to low conductivity that will not allow stable tunneling currents (see chapter 2 for experimental details). To understand the local film morphology and transport properties, it requires the use of AFM for which conductive samples are not required. In recent years, cryogenic AFM in UHV has actually exceeded the spatial resolution possible with the best STM. G.Meyer and co-workers have used tuning-fork-based AFM to image the sigma-bond framework in organic molecules such as pentacene[70]. In essence, these tour-de-force experiments obtain single atom resolution within organic molecules.

In more routine experiments, AFM has resolution typically on the length scale of 10's of nanometers and can be used as an effective probe of film roughness and general morphology[71]. Moreover, a number of adaptations of the AFM instrument allow local probes of electrical properties of samples.

One of such adaptation is called scanning Kelvin probe microscopy (SKPM), also known as surface potential microscopy. SKPM is a SPM technique where the potential offset between a probe tip and a surface can be measured using the same principle as a macroscopic Kelvin probe. L.C.Teague and co-workers have used SKPM to study single crystal diF-TESADT organic transistors[72]. SKPM provided a direct measurement of the intrinsic charge transport in the crystals independent of contact effects and revealed that degradation of

device performance occurred over a time period of minutes as the diF-TESADT crystal became charged.

Electrostatic force microscopy (EFM) is one more variation of dynamic non-contact AFM where the electrostatic force is probed. T.D.Krauss and L.E.Brus have done early contribution to using EFM to study charge, polarizability and photoionization of single semiconductor nanocrystals on CdSe[73]. They determined that the static dielectric constant of CdSe nanocrystals with diameters~5 nm is uniform. However, the charge per nanocrystal is nonuniform, with some nanocrystals possessing a positive charge.

Another SPM technique widely used in interface studies is conducting atomic force microscopy (CAFM). By using a conducting tip in contact with the sample surface, current map of an area or on a certain position can be acquired simultaneously with morphology scanning. D.S.Ginger's group is quite famous in this CAFM domain and they have done a lot of research of CAFM on organic solar cells. They demonstrate that photoconductive atomic force microscopy (pcAFM) can be used to map local photocurrents with 20 nm resolution in donor/acceptor blend solar cells of the MDMO-PPV with the PCBM spin-coated from various solvents[74]. They found significant variation in the short-circuit current between regions that appeared identical in AFM topography. These variations occurred from one domain to another as well as on larger length scales incorporating multiple domains. These results suggested that the performance of polymer-fullerene blends could still be improved through better control of morphology. By using various scanning probe techniques: light beam induced current spectroscopy (LBIC), CAFM, and PC-AFM, they also demonstrate that solvent vapor annealing (SVA) improved the power conversion efficiency by 40% while

forming mesoscopic PCBM crystallites and a ~3nm copolymer-rich overlayer at the cathode interface[75]. They found that the large crystallites created during annealing did not directly improve the local performance of the device, but instead attributed the performance improvement to the ripened blend morphology and an increase in the hole mobility of the copolymer in comparison to the unannealed blend. The PCBM-rich aggregates acted as a sink for excess PCBM, although excess PCBM was initially required to form the appropriate structural features prior to the annealing process.

FIGURES

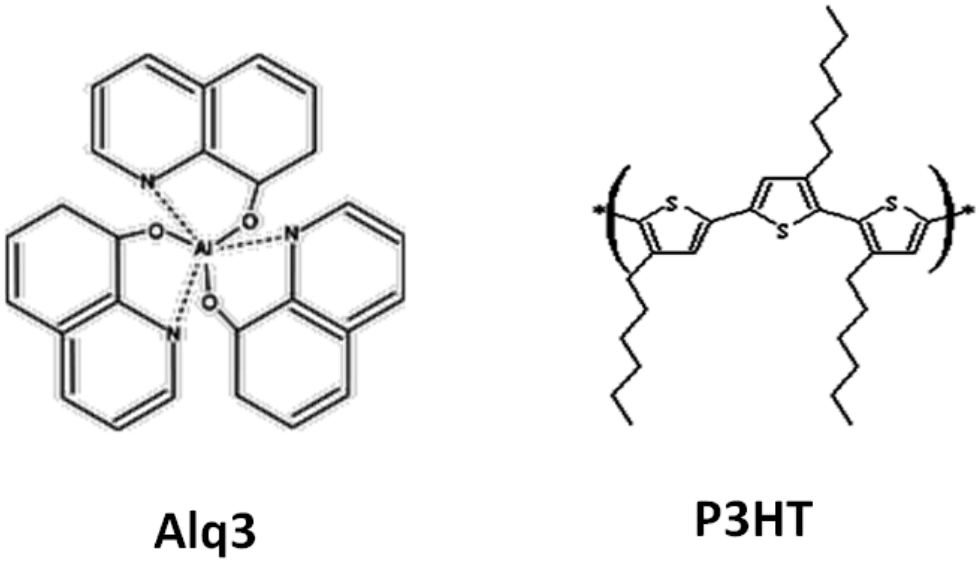


Figure 1.1 Chemical structures of Alq3 and P3HT.

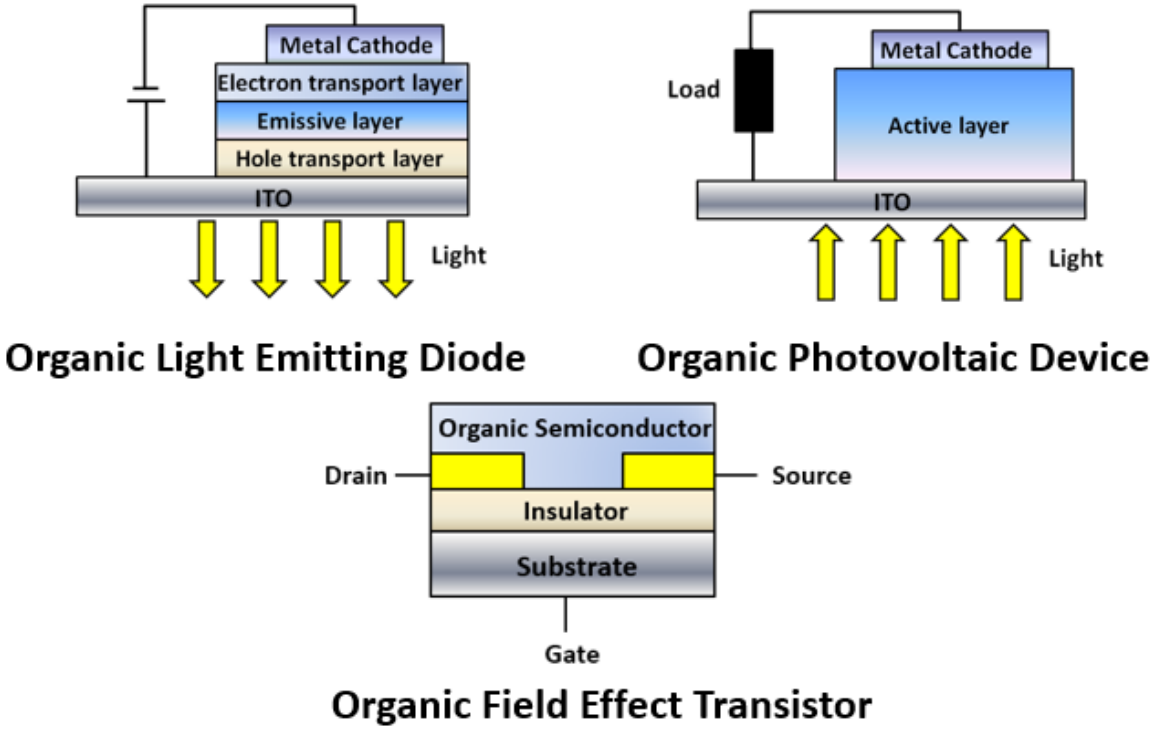


Figure 1.2 Schematic of OLED, OPV and PFET.

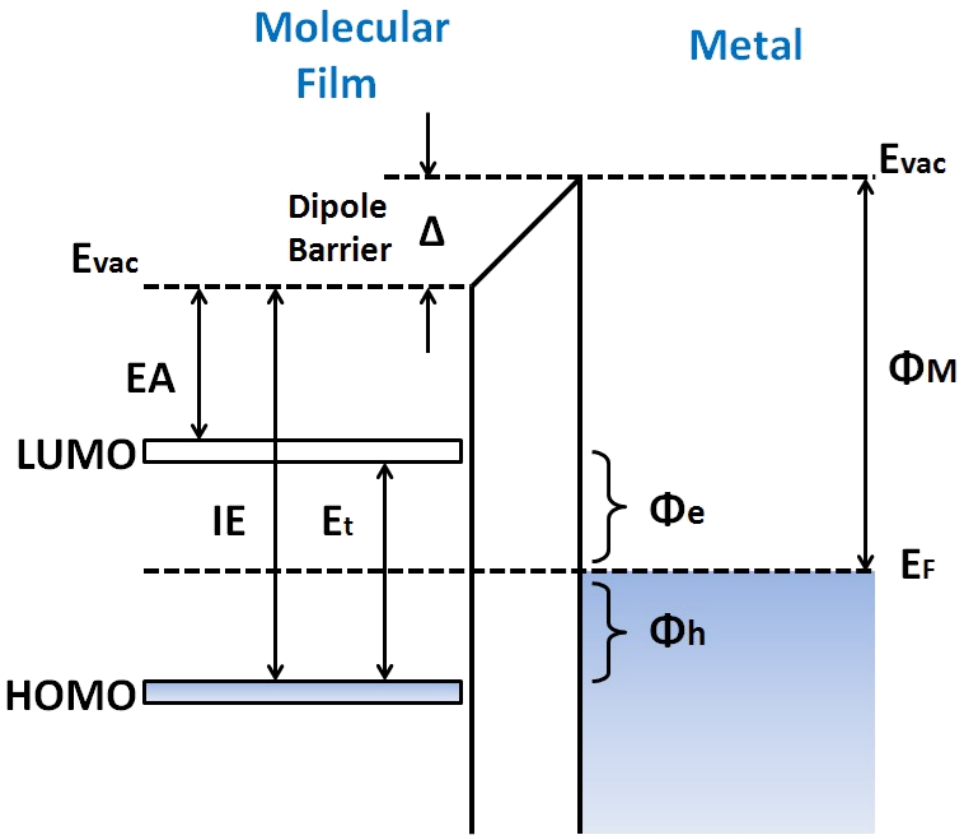


Figure 1.3 Energy diagram of an interface between a molecular film and a metal surface.

REFERENCES

(1)Pope, M.; Kallmann, H. P.; Magnante, P. *J.Chem.Phys.* **1963**, *38*, 2042.

(2)Shirakawa, H.; Louis, E. J.; MacDiarmid, A. G.; Chiang, C. K.; Heeger, A. J. *Journal of the Chemical Society, Chemical Communications* **1977**, 578.

(3)Tang, C. W.; VanSlyke, S. A. *Appl. Phys. Lett.* **1987**, *51*, 913.

(4)Tang, C. W. *Appl. Phys. Lett.* **1986**, *48*, 183.

(5)Ebisawa, F.; Kurokawa, T.; Nara, S. *J. Appl. Phys.* **1983**, *54*, 3255.

(6)Tsumura, A.; Koezuka, H.; Ando, T. *Appl. Phys. Lett.* **1986**, *49*, 1210.

(7)Zaumseil, J.; Sirringhaus, H. *Chem. Rev.* **2007**, *107*, 1296.

(8)Murphy, A. R.; Frechet, J. M. *Chem. Rev.* **2007**, *107*, 1066.

(9)Tsao, H. N.; Cho, D.; Andreasen, J. W.; Rouhanipour, A.; Breiby, D. W.; Pisula, W.; Müllen, K. *Adv. Mater.* **2009**, *21*, 209.

(10)Ito, Y.; Virkar, A. A.; Mannsfeld, S.; Oh, J. H.; Toney, M.; Locklin, J.; Bao, Z. *J.Am.Chem.Soc.* **2009**, *131*, 9396.

(11)Wang, C. H.; Hsieh, C. Y.; Hwang, J. C. *Adv. Mater.* **2011**, *23*, 1630.

(12)Podzorov, V.; Pudalov, V. M.; Gershenson, M. E. *Appl. Phys. Lett.* **2003**, *82*, 1739.

(13)Butko, V. Y.; Chi, X.; Lang, D. V.; Ramirez, A. P. *Appl. Phys. Lett.* **2003**, *83*, 4773.

(14)Boer, R. W. I. d.; Klapwijk, T. M.; Morpurgo, A. F. *Appl. Phys. Lett.* **2003**, *83*, 4345.

(15)Kawasugi, Y.; Yamamoto, H. M.; Hosoda, M.; Tajima, N.; Fukunaga, T.; Tsukagoshi, K.; Kato, R. *Appl. Phys. Lett.* **2008**, *92*, 243508.

(16)http://www.heliatek.com/newscenter/latest_news/neuer-weltrekord-fur-organische-solarzellen-heliatek-behauptet-sich-mit-12-zelleffizienz-als-technologiefuhrer/?lang=en

(17)Kido, J.; Kimura, M.; Nagai, K. *Science* **1995**, *267*, 1332.

(18)Lamansky, S.; Djurovich, P.; Murphy, D.; Abdel-Razzaq, F.; Lee, H.-E.; Adachi, C.; Burrows, P. E.; Forrest, S. R.; Thompson, M. E. *J.Am.Chem.Soc.* **2001**, *123*, 4304.

(19)Reineke, S.; Lindner, F.; Schwartz, G.; Seidler, N.; Walzer, K.; Lüssem, B.; Leo, K. *Nature* **2009**, *459*, 234.

(20)Wang, Z.; Helander, M.; Qiu, J.; Puzzo, D.; Greiner, M.; Hudson, Z.; Wang, S.; Liu, Z.; Lu, Z. *Nat. Photonics* **2011**, *5*, 753.

(21)Slyke, S. A. V.; Chen, C. H.; Tang, C. W. *Appl. Phys. Lett.* **1996**, *69*, 2160.

(22)Schilinsky, P.; Waldauf, C.; Brabec, C. J. *Appl. Phys. Lett.* **2002**, *81*, 3885.

(23)Peumans, P.; Yakimov, A.; Forrest, S. R. *J. Appl. Phys.* **2003**, *93*, 3693.

(24)Karl, N.; Marktanner, J. *Molecular Crystals and Liquid Crystals Science and Technology. Section A. Molecular Crystals and Liquid Crystals* **2001**, *355*, 149.

(25)Jurchescu, O. D.; Baas, J.; Palstra, T. T. M. *Appl. Phys. Lett.* **2004**, *84*, 3061.

(26)Campbell, A. J.; Bradley, D. D. C.; Antoniadis, H. *Appl. Phys. Lett.* **2001**, *79*, 2133.

(27)Blom, P. W. M.; de Jong, M. J. M.; van Munster, M. G. *Phys.Rev. B* **1997**, *55*, R656.

(28)Gill, W. D. *J. Appl. Phys.* **1972**, *43*, 5033.

(29)Baldo, M.; O'brien, D.; Thompson, M.; Forrest, S. *Phys.Rev. B* **1999**, *60*, 14422.

(30)Ruiz, R.; Nickel, B.; Koch, N.; Feldman, L. C.; Haglund, R. F.; Kahn, A.; Scoles, G. *Phys.Rev. B* **2003**, *67*, 125406.

(31)Witte, G.; Woll, C. *JOURNAL OF MATERIALS RESEARCH-PITTSBURGH THEN WARRENDALE-*. **2004**, *19*, 1889.

(32)Dinelli, F.; Murgia, M.; Levy, P.; Cavallini, M.; Biscarini, F.; de Leeuw, D. M. *Phys. Rev. Lett.* **2004**, *92*, 116802.

(33)Mott, N. In *Proc. Camb. Phil. Soc*; Cambridge Univ Press: 1938; Vol. 34, p 568.

(34)Schottky, W. *Zeitschrift für Physik A Hadrons and Nuclei* **1942**, *118*, 539.

(35)Kera, S.; Yabuuchi, Y.; Yamane, H.; Setoyama, H.; Okudaira, K.; Kahn, A.; Ueno, N. *Phys.Rev. B* **2004**, *70*, 085304.

(36)Yamane, H.; Yoshimura, D.; Kawabe, E.; Sumii, R.; Kanai, K.; Ouchi, Y.; Ueno, N.; Seki, K. *Phys.Rev. B* **2007**, *76*, 165436.

(37)Flores, F.; Ortega, J.; Vázquez, H. *Phys.Chem.Chem.Phys.* **2009**, *11*, 8658.

(38)Witte, G.; Lukas, S.; Bagus, P. S.; Woll, C. *Appl. Phys. Lett.* **2005**, *87*, 263502.

(39)Knupfer, M.; Paasch, G. *Journal of Vacuum Science & Technology A: Vacuum, Surfaces, and Films* **2005**, *23*, 1072.

(40)Ishii, H.; Sugiyama, K.; Ito, E.; Seki, K. *Adv. Mater.* **1999**, *11*, 605.

(41)Eremtchenko, M.; Bauer, D.; Schaefer, J.; Tautz, F. *New J. Phys.* **2004**, *6*, 4.

(42)Wang, Z.; Pronschinske, A.; Dougherty, D. B. *Org. Electron.* **2011**, *12*, 1920.

(43)Miller, A.; Abrahams, E. *Physical Review* **1960**, *120*, 745.

(44)Mott, N.; Twose, W. *Adv. Phys.* **1961**, *10*, 107.

(45)Ambegaokar, V.; Halperin, B.; Langer, J. *Phys.Rev. B* **1971**, *4*, 2612.

(46)Yu, Z.; Smith, D.; Saxena, A.; Martin, R.; Bishop, A. *Phys.Rev. B* **2001**, *63*, 085202.

(47)Meisel, K.; Pasveer, W.; Cottaar, J.; Tanase, C.; Coehoorn, R.; Bobbert, P.; Blom, P.; de Leeuw, D.; Michels, M. *physica status solidi (c)* **2006**, *3*, 267.

(48)Tutiš, E.; Batistić, I.; Berner, D. *Phys.Rev. B* **2004**, *70*, 161202.

(49)Van Der Holst, J.; Uijttewaal, M.; Ramachandhran, B.; Coehoorn, R.; Bobbert, P.; de Wijs, G.; de Groot, R. *Phys.Rev. B* **2009**, *79*, 085203.

(50)Van der Holst, J.; van Oost, F.; Coehoorn, R.; Bobbert, P. *Phys.Rev. B* **2011**, *83*, 085206.

(51)Parker, I. D. *J. Appl. Phys.* **1994**, *75*, 1656.

(52)Sze, S. M.; Ng, K. K. *Physics of semiconductor devices*; Wiley. com, 2006.

(53)Arkhipov, V.; Emelianova, E.; Tak, Y.; Bassler, H. *J. Appl. Phys.* **1998**, *84*, 848.

(54)Wolf, U.; Arkhipov, V.; Bässler, H. *Phys.Rev. B* **1999**, *59*, 7507.

(55)Burin, A. L.; Ratner, M. A. *J.Chem.Phys.* **2000**, *113*, 3941.

(56)Baldo, M.; Forrest, S. *Phys.Rev. B* **2001**, *64*, 085201.

(57)Ishii, H.; Seki, K. *Electron Devices, IEEE Transactions on* **1997**, *44*, 1295.

(58)Wan, A.; Hwang, J.; Amy, F.; Kahn, A. *Org. Electron.* **2005**, *6*, 47.

(59)Koch, N.; Kahn, A.; Ghijsen, J.; Pireaux, J.-J.; Schwartz, J.; Johnson, R. L.; Elschner, A. *Appl. Phys. Lett.* **2003**, *82*, 70.

(60)Park, Y.; Choong, V.-E.; Hsieh, B. R.; Tang, C. W.; Wehrmeister, T.; Müllen, K.; Gao, Y. *Journal of Vacuum Science & Technology A* **1997**, *15*, 2574.

(61)Petraki, F.; Peisert, H.; Biswas, I.; Chassé, T. *The Journal of Physical Chemistry C* **2010**, *114*, 17638.

(62)Hill, I. G.; Kahn, A.; Soos, Z. G.; Pascal, R. A. *Chem. Phys. Lett.* **2000**, *327*, 181.

(63)Djurovich, P. I.; Mayo, E. I.; Forrest, S. R.; Thompson, M. E. *Org. Electron.* **2009**, *10*, 515.

(64)Gahl, C.; Ishioka, K.; Zhong, Q.; Hotzel, A.; Wolf, M. *Faraday Discuss.* **2000**, *117*, 191.

(65)Barlow, D. E.; Scudiero, L.; Hipps, K. W. *Langmuir* **2004**, *20*, 4413.

(66)Mishchenko, A.; Vonlanthen, D.; Meded, V.; Bürkle, M.; Li, C.; Pobelov, I. V.; Bagrets, A.; Viljas, J. K.; Pauly, F.; Evers, F.; Mayor, M.; Wandlowski, T. *Nano Lett.* **2009**, *10*, 156.

(67)Kang, J. H.; Filho, D. d. S.; Bredas, J.-L.; Zhu, X.-Y. *Appl. Phys. Lett.* **2005**, *86*, 152115.

(68)Dougherty, D. B.; Jin, W.; Cullen, W. G.; Reutt-Robey, J. E.; Robey, S. W. *Appl. Phys. Lett.* **2009**, *94*, 023103.

(69)Soubatch, S.; Weiss, C.; Temirov, R.; Tautz, F. *Phys. Rev. Lett.* **2009**, *102*, 177405.

(70)Gross, L.; Mohn, F.; Moll, N.; Liljeroth, P.; Meyer, G. *Science* **2009**, *325*, 1110.

(71)Salleo, A.; Kline, R. J.; DeLongchamp, D. M.; Chabinyc, M. L. *Adv. Mater.* **2010**, *22*, 3812.

(72)Teague, L. C.; Jurchescu, O. D.; Richter, C. A.; Subramanian, S.; Anthony, J. E.; Jackson, T. N.; Gundlach, D. J.; Kushmerick, J. G. *Appl. Phys. Lett.* **2010**, *96*.

(73)Krauss, T. D.; Brus, L. E. *Phys. Rev. Lett.* **1999**, *83*, 4840.

(74)Coffey, D. C.; Reid, O. G.; Rodovsky, D. B.; Bartholomew, G. P.; Ginger, D. S. *Nano Lett.* **2007**, *7*, 738.

(75)Bull, T. A.; Pingree, L. S. C.; Jenekhe, S. A.; Ginger, D. S.; Luscombe, C. K. *ACS Nano* **2009**, *3*, 627.

# Chapter 2

# Experimental Methods

This chapter describes the experimental methods used in this dissertation. Firstly, organic molecular beam deposition (OMBD) as the most important deposition methods used in this dissertation will be introduced. Secondly, atomic force microscopy (AFM), conducting AFM (CAFM) and ultraviolet-visible absorption spectroscopy (UV-Vis) which are the main experimental methods to be used in chapter 3 will be reviewed. Finally, scanning tunneling microscopy (STM) and scanning tunneling spectroscopy (STS) will be described in detail due to they are the key techniques used in chapter 4 and 5.

## 2.1 Organic Molecular Beam Deposition

All the organic thin films studied in the following chapters are grown by organic molecular beam deposition (OMBD) in vacuum (P3HT:$C_{60}$ thin film to be discussed in chapter 3, α-NPD on Au(111) surface in chapter 4 and α-6T on $C_{60}$ monolayer in chapter 5). This technique has been used for many years and reviews by Forrest[1] and Schreiber[2] describe many important conceptual and practical details. Compared to the solution-processing method commonly used for polymer deposition, OMBD is mainly used for small-molecule thin film preparations and it has several advantages: (1) No restriction on organic material

solubility; (2) Easy to control the deposition rate; (3) Able to grow complex structure layer by layer. An organic molecule can be grown by OMBD in vacuum if it satisfies: (1) Its vapor pressure is less than the required background pressure of the chamber under ultra-high vacuum (UHV) and room temperature (RT); (2) Its sublimation temperature must be less than its chemical decomposition temperature; (3) It must allow for proper outgassing of its impurities.

A schematic diagram of OMBD is shown in Figure 2.1. Organic material is loaded in the crucible (usually made of quartz or boron nitride), which is tightly wrapped by tantalum wires. Direct current passes through the tantalum wire as a heater to cause source organic materials to sublimate. Vaporized material will flow towards the substrate at RT and condense there to form a molecular thin film. Quartz crystal micro-balance (QCM) is located near the position of substrate to monitor the nominal deposition rate and film thickness. The QCM measures a mass of per unit area on a quartz crystal resonator surface by measuring the change in frequency of the resonator. The thickness of the deposited film on surface of resonator can be calculated with knowing the density of deposited materials.

## 2.2 AFM and Conducting AFM Introduction

### 2.2.1 History

Atomic force microscopy (AFM) is a very useful tool for direct measurements of intermolecular forces with atomic-resolution characterization that can be employed in a broad area of applications such as electronics, semiconductors and materials. The first AFM was invented by Binnig, Quate and Gerber in 1986[3] and the first commercially available

AFM was introduced in 1989. While the true atomic resolution capability of AFM was anticipated from the beginning, it took five years before atomic resolution on inert surfaces could be demonstrated[4,5]. Resolving reactive surfaces by AFM with atomic resolution took almost a decade from the invention of the AFM. The Si(111) – (7 ×7) surface, a touchstone of the AFM's feasibility as a tool for surface science, was resolved with atomic resolution by dynamic atomic force microscopy[6]. In chapter 3, we will use AFM and conducting AFM as a main tool to study the topography and charge transport of P3HT:$C_{60}$ thin films.

### 2.2.2 AFM basic principles

As depicted in Figure 2.2A, a typical AFM system consists of a cantilever probe, a sharp tip mounted to a piezoelectric actuator and a position sensitive photodiode for receiving a laser beam reflected from the end-point of the cantilever to provide cantilever deflection feedback. The basic principle of AFM operation is to scan the tip over the sample surface with feedback mechanisms that maintain the tip at a constant force or constant height above the sample surface. As the tip scans the surface of the sample, moving up and down following the topography of the surface, the laser beam deflected from the cantilever provides measurements of the difference in light intensities between upper and lower photo detectors. Feedback from the photodiode difference signal, through software control from the computer, enables the tip to maintain either a constant force or constant height above the surface. In the constant force mode, the piezoelectric element monitors real time height deviation. In the constant height mode, the deflection force between tip and surface is recorded. Figure 2.2B shows a SEM image of an uncoated silicon AFM probe tip. The

dimensions of the cantilever are in the scale of micrometers and the radius of the tip is in the scale of a few nanometers. The backside of the cantilever is often coated in order to increase the reflectance of the cantilever and to improve the deflection signal.

### 2.2.3 AFM operational and control modes

Typically there are three AFM operational and control modes[7]: non-contact mode, contact mode and tapping mode. The interaction forces between the tip and sample in all of these three modes can be distinctly identified on a force-distance curve as shown in Figure 2.3.When the interatomic distance is quite large, weak attractive forces are generated between the tip and the sample. As the tip is gradually brought closer to the sample surface, the attractive forces increase until the atoms become so close that the electron clouds begin to repel each other electrostatically. This repulsive force between the atoms progressively weakens the attractive forces as the interatomic distance decreases. The interaction force becomes zero when the distance between the atoms reaches a couple of angstroms and becomes repulsive when the atoms are in contact.

Figure 2.4 depicts a schematic diagram of the operation in all the three modes as well as the surface topography that would be generated in each mode. It can be seen that the tapping and non-contact modes reveal the surface topography of the sample to a greater extent comparing to the contact mode. Also, the operation of the AFM in contact mode can sometimes damage the sample surface due to the lateral dragging forces exerted by the probe tip. The detailed description and operational characteristics of each mode is described next.

#### 2.2.3.1 Contact AFM mode

In contact AFM mode (also known as repulsive mode), the tip is in close contact with sample as it scans the surface, where the interaction forces between the tip and sample are mainly repulsive. As shown in Figure 2.3 red curve, the slope of the curve in the contact regime is very steep. This is due to the electron clouds in the atoms repel each other electrostatically at such close interatomic distance. As a result, the repulsive van der Waals force dominates any other attractive force.

In contact AFM, the surface profile is generated by operating either of the two modes: constant height mode or constant force mode. In constant height mode, the piezoelectric scanner holding the AFM tip laterally scans the surface of the sample without moving in the z-direction. The cantilever deflection can be utilized to estimate the surface topography. The drawback of this technique is that the presence of any steep steps on the sample surface may damage the tip.

In the constant force mode, which is most widely utilized, the normal force acting between the tip and the sample is kept constant through a feedback loop. A piezoelectric positioning element is used to position the probe tip to keep the applied force a constant.

#### 2.2.3.2 Non-contact AFM mode

In this mode, the cantilever tip is about 5-15 nm above the sample surface (blue curve in Figure 2.3) to detect the attractive van der Waals forces between the tip and sample. Since the attractive forces are substantially weaker than the forces used in contact mode, the tip

must be given a small oscillation so that these small forces can be detected by measuring the change in amplitude, phase, or frequency of the oscillating cantilever.

Unlike the STM and contact AFM, the absence of repulsive forces in non-contact AFM permits the imaging of soft samples to provide topography with little or no contact between the tip and sample. The total force between the tip and sample in the non-contact regime is very low, generally about 10-12 pN. This low force is advantageous for studying soft or elastic samples. Another advantage is that the sample will not be contaminated through contact with the tip. Therefore, non-contact AFM mode does not suffer from tip or sample degradation effects sometimes observed after taking numerous scans with contact AFM.

2.2.3.3 Tapping AFM mode

In this mode, the piezoelectric actuator applies a force on the cantilever and causes the cantilever tip to vibrate near its resonance frequency similar to non-contact mode, but with a amplitude greater than 10nm, typically 100–200 nm. The vibrating tip is now moved close to the sample until it begins to lightly tap the surface. During scanning, the probe tip alternately touches the surface and lifts off at frequencies of about 50–500 k cycles/s. Owing to the energy losses caused due to intermittent contacting of the tip with the surface, the amplitude of vibration changes according to the surface topography of the sample.

During tapping mode operation, the oscillation amplitude is kept constant through a feedback loop. When the tip passes over a bump in the surface, its vibration amplitude decreases due to availability of less vibrating space. On the other hand, when it passes over a

depression, its vibration amplitude increases (approaching its free air amplitude)[8]. This change in oscillation amplitude is detected by the optical system and fed back to the controller which compares the measured value with the set reference value and generates an error signal. This signal actuates the piezoelectric element that adjusts the tip–sample separation to maintain constant amplitude and thereby constant force on the sample. The error signal applied to the piezoelectric element is expressed as a function of the tip's lateral position and used to plot the surface topography of the sample.

### 2.2.4 Conducting AFM

In the study of organic electronics, performing quantitative and reliable measurements of the electrical properties of molecular nanostructures and single molecules remains a big challenge. Conducting AFM is great tool to investigate both topography and electronic characteristics of the molecular surface simultaneously[9].

As a variation of conventional AFM, conducting AFM uses an AFM tip with an electrically conducting coating as a movable electrode in a conventional AFM setup. The tip is brought into contact with the surface at a position of interest with a user-specified applied force, which is maintained by the AFM's feedback electronics. Current-voltage (*I*–*V*) characteristics are acquired at fixed points on the surface by applying a voltage between the AFM tip and conducting substrate, and measuring the resulting current between the electrodes, as shown in Figure 2.5. Depending on the system under study, the measured currents can range from pico-Amperes to hundreds of nano-Amperes.

Conducting AFM can also be used for imaging. In this mode, a constant voltage is applied between the tip and the conducting substrate, and the current is recorded while the tip is scanning over the sample surface. This provides a spatial map of the local sample conductivity. The sample topography can also be measured simultaneously, making it possible to correlate spatial variations in the conductivity with the topography.

One of the strengths of conducting AFM is the ability to image a sample's structure using conventional AFM, and then use the AFM tip as a movable electrode to perform *I–V* measurements selected areas. The sample can then also be imaged again, following the *I–V* measurement, to verify that the sample structure was not perturbed during the measurement. This capability of visualizing structure and measuring *I–V* characteristics makes it possible to measure the *I–V* properties of specific nanostructures and to study the relationship between physical structure and electronic behavior.

A further advantage of conducting AFM is the use of force feedback for controlling the tip–sample separation. As a result, the vertical positioning of the tip is decoupled from the electrical measurements. This is not the case in STM, where the tunneling current is used for regulating the position of the tip. Owing to the typically unknown electrical properties of the material under investigation, the precise vertical position of the tip with respect to the sample is often unknown. A second advantage of using force feedback for regulating the force is the possibility of measuring electrical properties as a function of applied load. This allows for the investigation of the connection between mechanical and electrical contact, and the effect of compression and deformation on molecular transport.

## 2.3 Ultraviolet-Visible Absorption Spectroscopy

Ultraviolet-Visible Absorption Spectroscopy (UV-Vis) is a spectroscopy working in the ultraviolet (~180 to 400 nm) and visible (~400 to 750 nm) spectral region. UV-Vis spectroscopy is routinely used in analytical chemistry for the quantitative determination of different analytes, such as transition metal ions[10], highly conjugated organic compounds[11] and biological macromolecules[12]. In chapter 3, UV-Vis will be utilized to study the P3HT:$C_{60}$ thin films.

The working principle of UV-Vis spectroscopy is that molecules containing π-electrons or non-bonding electrons (n-electrons) can absorb ultraviolet or visible photons to excite these electrons to higher anti-bonding molecular orbitals. Figure 2.6 shows a schematic diagram of possible electronic transitions between different molecular orbitals. The three gray dotted arrows (σ to σ* transition, σ to π* transition, π to σ* transition) indicate the impossible transitions due to energy needed out of the range of UV-Vis spectral region. The n to σ* transition (grey arrow) is possible but often falls deep in the UV regions at energies higher than typically analyzed. The most important transitions are π to π * and n to π * (two black arrows), which are most favorable in electronic transitions in UV-Vis spectral range and commonly seen in UV-Vis spectroscopy as absorption peaks.

If the energy levels are isolated as shown in Figure 2.6, these electronic transitions should result in very narrow absorption bands at wavelengths corresponding to the difference between energy levels. However, vibrational and rotational energy levels are superimposed on the electronic energy levels. Due to these rotational and vibrational sub-levels, as well as structural disorder in the film, the electronic absorption bands are broadened. One more topic

is how film crystallinity could impact the position of absorption peaks, which will be important in chapter 3. This question could be explained by *Particle in a box* theory qualitatively[13]. The energy levels in an organic thin film could be represented as

$$\mathrm{E_n} = \frac{n^2\pi^2\hbar^2}{2mL^2}\,, \tag{2.1}$$

where n={1,2,3,4,…}, m is mass of the particle, ħ is the reduced Planck constant and L is the conjugation length of this organic film. The absorption peak position in UV-Vis will be related to

$$\Delta\mathrm{E}=\mathrm{E}_{n+1}-\mathrm{E}_n \propto \frac{1}{L^2}\,. \tag{2.2}$$

Larger conjugation length L will induce smaller ΔE, so the absorption peak will be red shifted; similarly, smaller conjugation length L will induce absorption peak blue shifted.

Figure 2.7 shows a schematic diagram of a typical UV-Vis spectrometer. A beam of light from a visible and/or UV light source (colored red) is separated into its component wavelengths by a prism or diffraction grating. Each monochromatic beam in turn is split into two equal intensity beams by a half-mirrored device. One beam, the sample beam (colored orange), passes through the sample (cuvette with a solution of the compound being studied or thin molecular film on transparent substrate). The other beam, the reference (colored blue), passes through the reference (cuvette with only the solvent or transparent substrate only). The intensities of these light beams are then measured by electronic detectors and compared. The intensity of the reference beam, which should have suffered little or no light absorption, is

defined as $I_0$. The intensity of the sample beam is defined as I. Over a short period of time, the spectrometer automatically scans all the component wavelengths in the manner described.

Most spectrometers display absorbance on the vertical axis, and corresponding light wavelength on the horizontal axis. Absorbance is defined as $A=\log (I_0/ I)$, and the commonly observed absorption range is from 0 ($I_0=I$) to 2 ($I=0.01\ I_0$).

## 2.4 Scanning tunneling microscopy and spectroscopy

### 2.4.1 Introduction to scanning tunneling microscopy

A scanning tunneling microscopy (STM) is an instrument for imaging surfaces at the atomic level by utilizing the quantum tunneling effect. It was invented by G. Binnig and H. Rohrer at IBM Zürich in 1981[14], and it earned its inventors the Nobel Prize in physics in 1986. Compared with other surface analytic techniques, such as scanning electron microscopy (SEM), transmission electron microscopy (TEM), X-ray photoemission spectroscopy (XPS) and ultraviolet photoemission spectroscopy (UPS), there are several advantages of STM[15]:

1. STM can achieve atomic-level resolution. The lateral and vertical resolution can reach 0.1 nm and 0.01 nm respectively.
2. STM can be performed in different environments, such as vacuum, air, low or high temperature, etc.. Due to no specific requirement for sample preparation needed and no damage to the sample during scanning in most situations, STM is especially suitable for in-situ electrochemical studies[16], biological studies[17] and the evaluation of sample surfaces[18] under various experimental conditions.

3. Rather than the averaged properties of the bulk phase or of a large surface area, STM will provide the truly local information on the atomic scale, which allows the study of individual surface adsorbates, surface defects, surface reconstructions and adsorption-induced surface reconstructions.
4. STM can obtain three dimensional images both in real space and real time. This capability allows in-situ imaging of some dynamical processes taking place on the surface.
5. STM-based techniques can provide local surface electronic properties such as the changes of surface barrier, energy gap and spectroscopic images.
6. STM can be employed for the manipulation of atoms and molecules through tip-sample interactions, which opens up the prospects of constructing nanoscale devices.

Figure 2.8 shows a schematic diagram of scanning tunneling microscope. An atomically sharp conducting metal tip, typically made of tungsten or platinum/iridium alloy, is brought within a short distance (~3-10 Å) of a conducting or semiconducting sample using a piezoelectric driver. This piezoelectric driver consists of three mutually perpendicular piezoelectric transducers to control tip moving in three dimensions (x and y parallel to the plane of sample surface, z perpendicular to the surface). When a voltage bias (tunneling voltage) is applied between the sample and tip, there will be a small tunneling current through the tip and sample (usually 1pA-10 nA). The STM tip is rastered across the surface in one of two modes: constant current or constant height. In constant-current mode, the feedback loop maintains the tunneling current a constant by adjusting the tip-sample

distance. The recorded topography is dependent on both the geometric structure and the local density of states (LDOS) of the tip and sample. Constant-current is able to measure surface features with higher precision (atomic resolution and better), but is generally slower due to the need for mechanical manipulation of the scanner in the z direction. In constant-height mode, the tip is maintained at a constant distance between tip and sample, recording the current and allowing for much faster measurements, but with the danger of intruding into tall structures on surface. Constant-current mode is most common in STM study and all the work done in the following chapters of this thesis is using constant-current mode. In the chapter 4 and 5, STM and STS will our powerful tool to study the structural and electronic disorder in different systems.

### 2.4.2 Background theory for STM/STS

#### 2.4.2.1 STM Theory

The principle STM operation relies on is quantum tunneling effect, which is one of the most fundamental features of quantum mechanics that distinguishes it from classical mechanics. In classical mechanics, an electron traveling between the tip and the sample would require energy greater than the work function of the tip/sample material to overcome the barrier between them. However, electrons are able to tunnel across the barrier in quantum mechanics. This can be explained by solving the time-independent Schrödinger equation of an electron through a one-dimensional junction with a rectangular barrier as shown in Figure 2.9,

$$\frac{-\hbar^2}{2m}\nabla^2\Psi(z)+V\Psi(z)=E\Psi(z), \tag{2.3}$$

where Ψ(z) is the wavefunction of the electron, z is the tip-sample separation, m is the electron mass, V is the potential energy of the barrier, E is the energy of the tunneling electron and ħ is Planck's constant.

The solution to equation (2.3) is

$$\Psi(z)=\Psi(0)e^{-\kappa z}\ , \tag{2.4}$$

where

$$\kappa=\frac{\sqrt{2m(V-E)}}{\hbar}\quad . \tag{2.5}$$

Through the Born interpretation of the wavefunction, the square of the wavefunction is proportional to the probability distribution of the electron. Therefore, the probability of tunneling yielding a tunneling current I:

$$\left|\Psi(z)\right|^2\propto e^{-2\kappa z}\propto I(z). \tag{2.6}$$

For small biases, the quantity (V-E) can be approximated as the work function of the metal (~5 eV)[19], thus, the tunneling current decreases by about one order of magnitude for every 1 Å change in z. This exponential decay of current enables the molecular and atomic resolution of the STM. Therefore, the tunneling current is extremely localized and the STM is sensitive to both lateral and vertical changes in topography[20,21].

2.4.2.2 STS Theory

Scanning tunneling spectroscopy (STS), as the most common modulation technique of STM, was first used by Binnig and Rohrer[22,23]. It has been used to characterize the electronic and vibrational properties of surfaces and adsorbed molecules. The advantage of STS lies in its ability of probing single atoms and molecules. In many cases, STS measurements are taken in ultrastable instruments in ultrahigh vacuum (UHV) so as to isolate the sample from acoustic and vibrational noise. STS is also done at cryogenic temperatures to reduce the thermal spread of electron energies.

Conventional STS is carried out at constant-height mode and extract electronic structures of the sample from normalized dI/dV curves. This theory starts from the expression of tunneling current that amounts to Fermi's golden rule using a tunneling transmission function calculated in the Wentzels-Kramer-Brillouin (WKB) approximation. For low temperature where the Fermi functions of both tip and sample are approximately step functions[24,25], the current can be represented as

$$I(z,V) = B\int_0^{eV} \rho_S(E)\rho_T(E-eV)T(z,V,E)dE\,, \tag{2.7}$$

where $\rho_S$ and $\rho_T$ are the LDOS of the sample and tip respectively, T(z,V,E) is the WKB tunneling transmission function, $B=(1/2)\,\pi e\hbar^3 m^{-2}A$ with A being the effective tunneling junction area and m the mass of tunneling electron. By taking derivative of I(z,V) and keeping in mind that z is a constant in the constant-height mode, we have

$$\frac{dI}{dV} = Be\rho_S(eV)\rho_T(0)T(z,V,eV) + B\int_0^{eV} \rho_S(E)\rho_T(E-eV)\frac{dT(z,V,E)}{dV}dE\,. \tag{2.8}$$

At this point, if we assume the transmission function is approximately constant in the integration range, we would have the result

$$\frac{V}{I}\frac{dI}{dV} \propto \rho_S(eV). \tag{2.9}$$

This normalized differential conductance is the conventional approach to extract sample density of states from STS measurements.

Another commonly-used STS mode is called constant-current STS or z(V) spectroscopy, and all the STS measurements in this thesis are using this mode. This mode has great advantages in that it allows tunneling spectroscopy to be carried out on physical systems that may be sensitive to high current injected from an STM, such as organic thin films. The use of small constant current can minimize the perturbation of the surface during the tunneling process and allow STS measurements routinely on the nanoscale system.

A differential equation for tip position z as a function of applied bias V has been deduced[26]:

$$\alpha\sqrt{\Phi}I\frac{dz}{dV} + \frac{\alpha eI}{4\sqrt{\Phi}}z - eB\rho_T\rho_S(eV)T(z,V,E=eV) = 0 \ . \tag{2.10}$$

In this expression, $\alpha = 2\sqrt{2m}/\hbar$, $\Phi$ is the apparent barrier height of the tunneling junction, m is the mass of tunneling electron, B=(1/2) $\pi e\hbar^3 m^{-2} A$ with A being the effective tunneling junction area, m is the mass of tunneling electron, $\rho_S$ and $\rho_T$ are LDOS of the sample and tip respectively.

Pronschinske et al. did numerical studies and to a good approximation they found[26]

$$\frac{V}{z}\frac{dz}{dV} \propto \rho_S(eV). \tag{2.11}$$

And they showed that this normalized dz/dV spectra has reproduced the peak positions in the sample LDOS usually to within 0.1eV. Hence the constant-current STS can be a valid alternative to the constant-height STS.

FIGURES

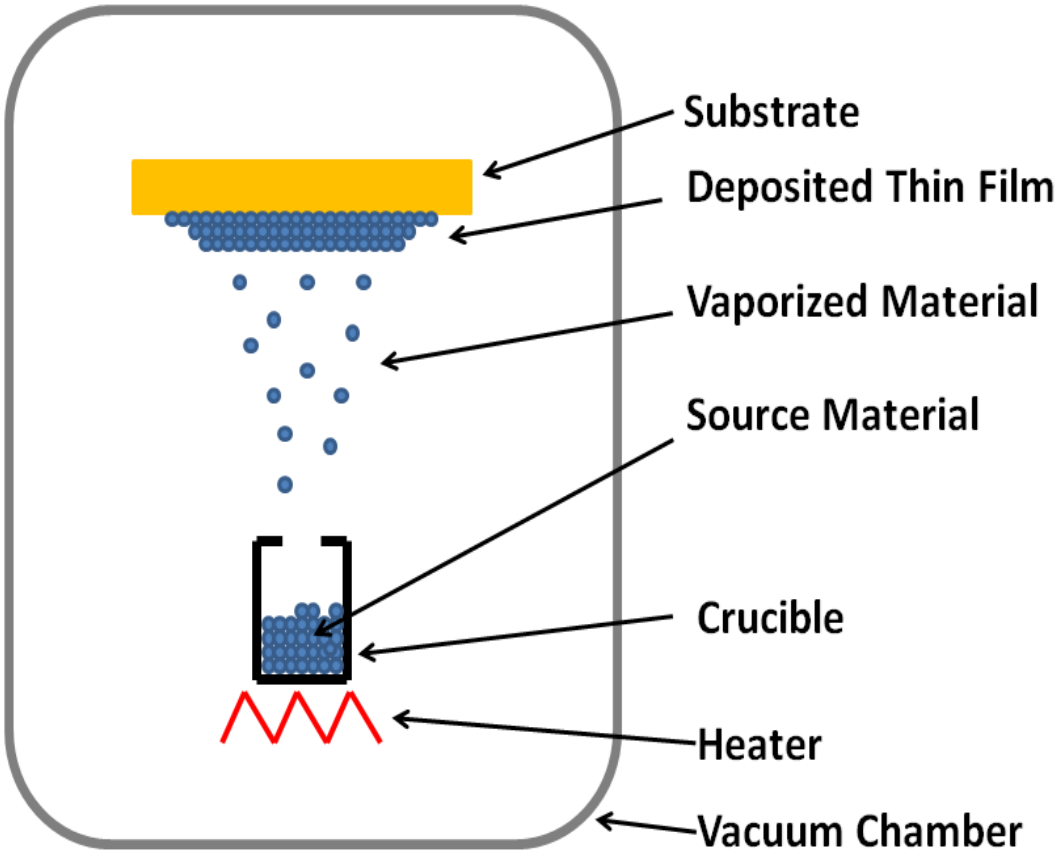


Figure 2.1 A schematic diagram of OMBD in vacuum.

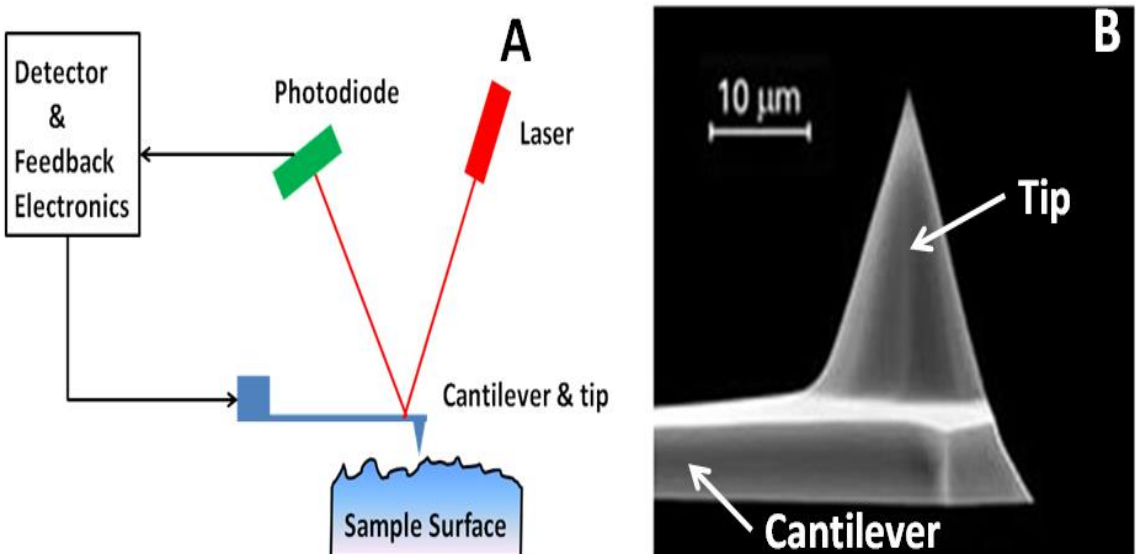


Figure 2.2 (A) Schematic diagram of AFM ;(B) SEM image of an uncoated silicon AFM probe tip.

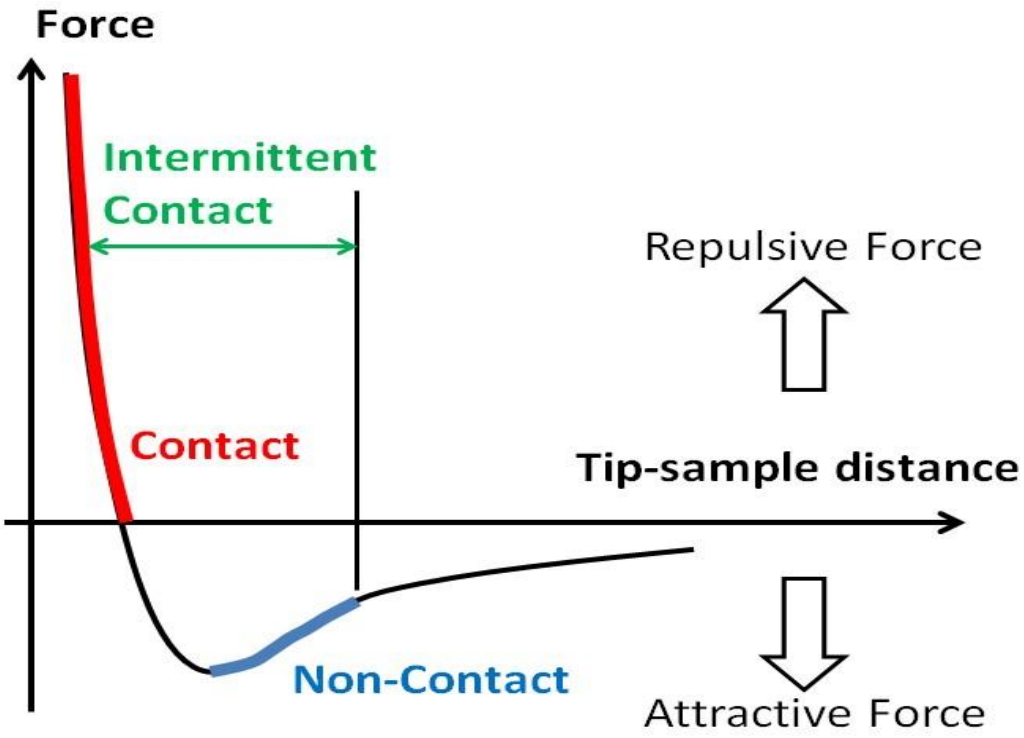


Figure 2.3 Interatomic force versus distance between the AFM tip and sample surface.

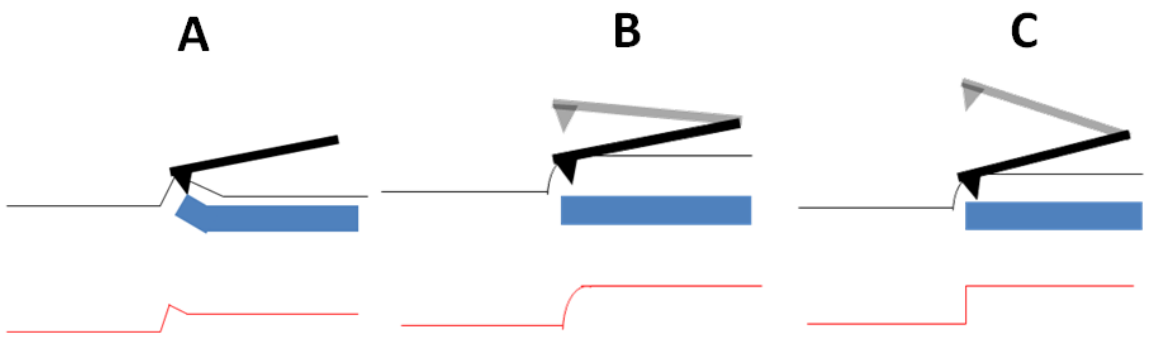


Figure 2.4 Comparison of (A) contact mode, (B) non-contact mode and (C) tapping mode AFM. The red curves under the images represent likely image data resulting from the three techniques.

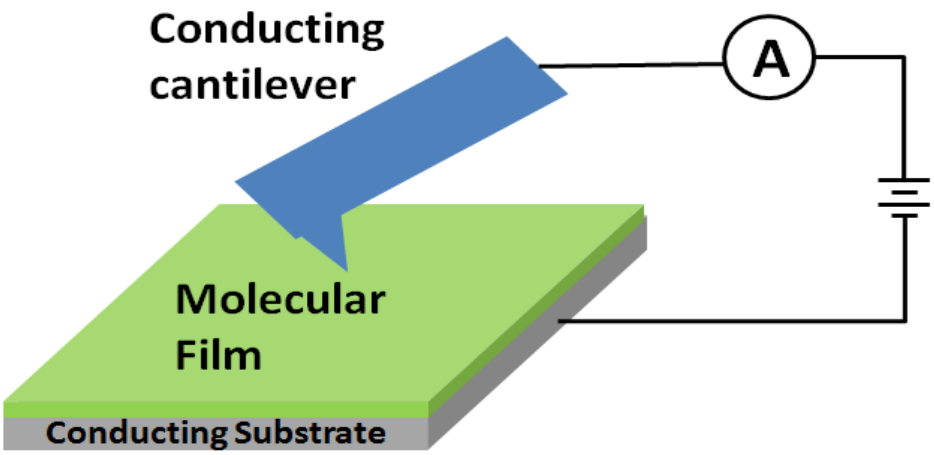


Figure 2.5 A schematic diagram of conducting AFM.

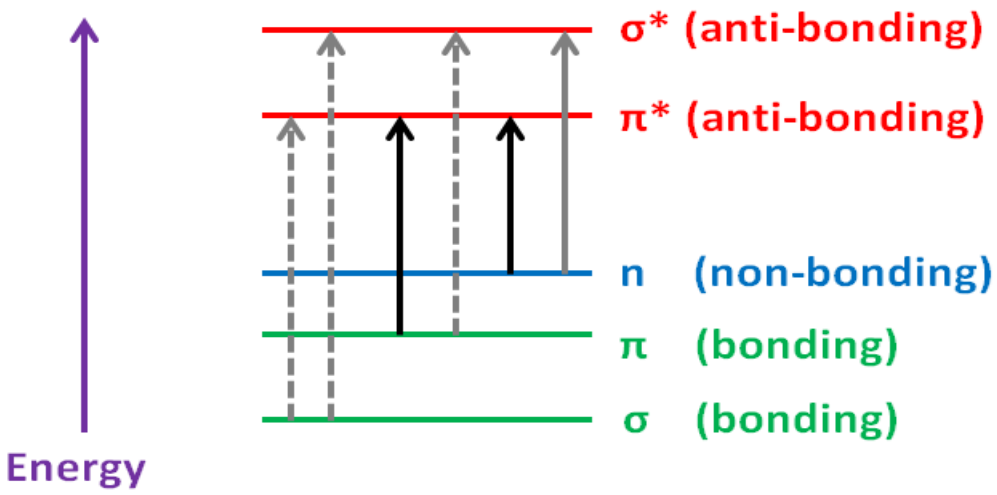


Figure 2.6 A schematic diagram of molecular orbitals and possible electronic transitions between them. The important jumps are shown in black, a less important one in grey and grey dotted arrows show jumps which absorb energy outside UV-Vis spectral range.

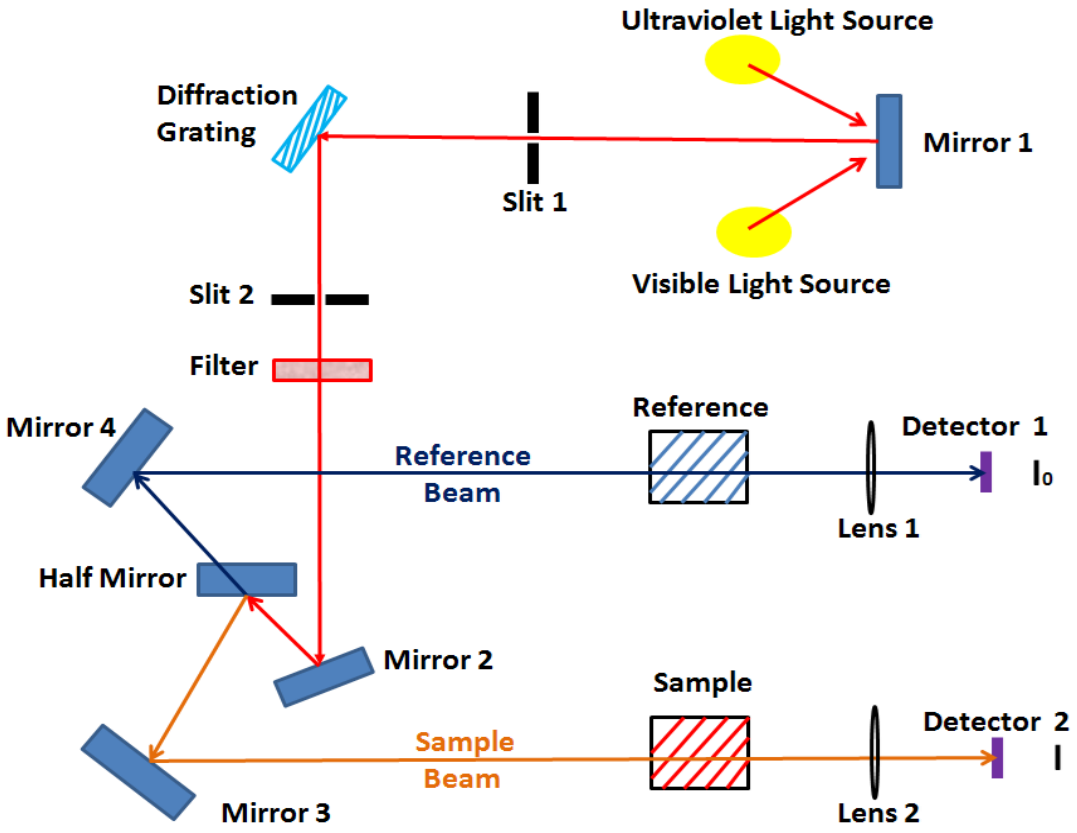


Figure 2.7 A Scheme of a typical UV-Vis absorption spectrometer.

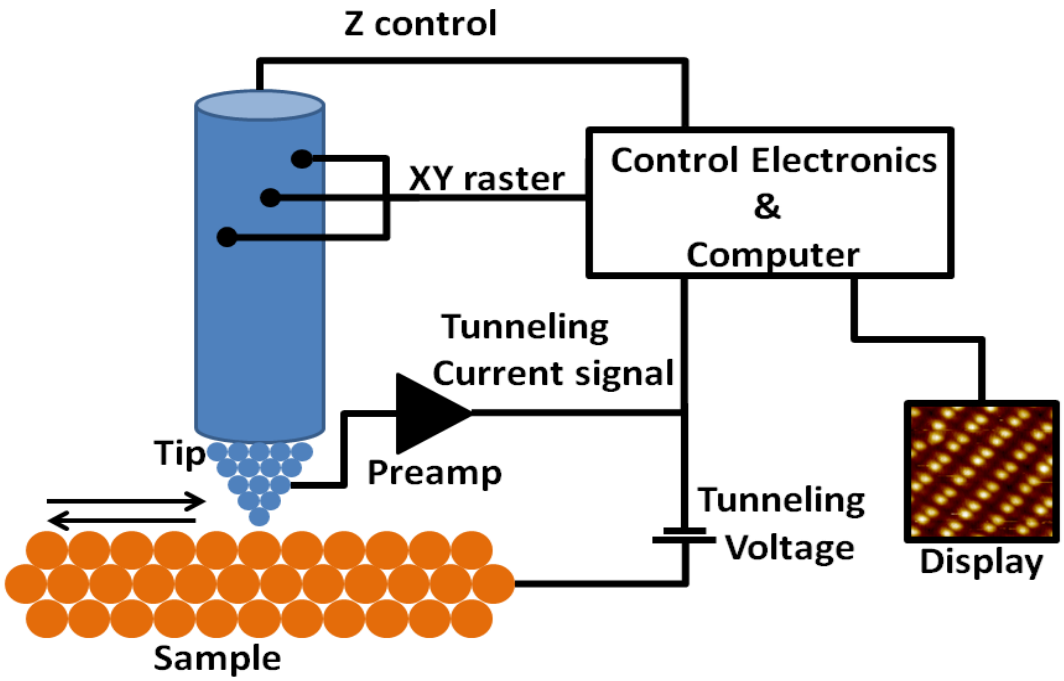


Figure 2.8 Schematic diagram of scanning tunneling microscope.

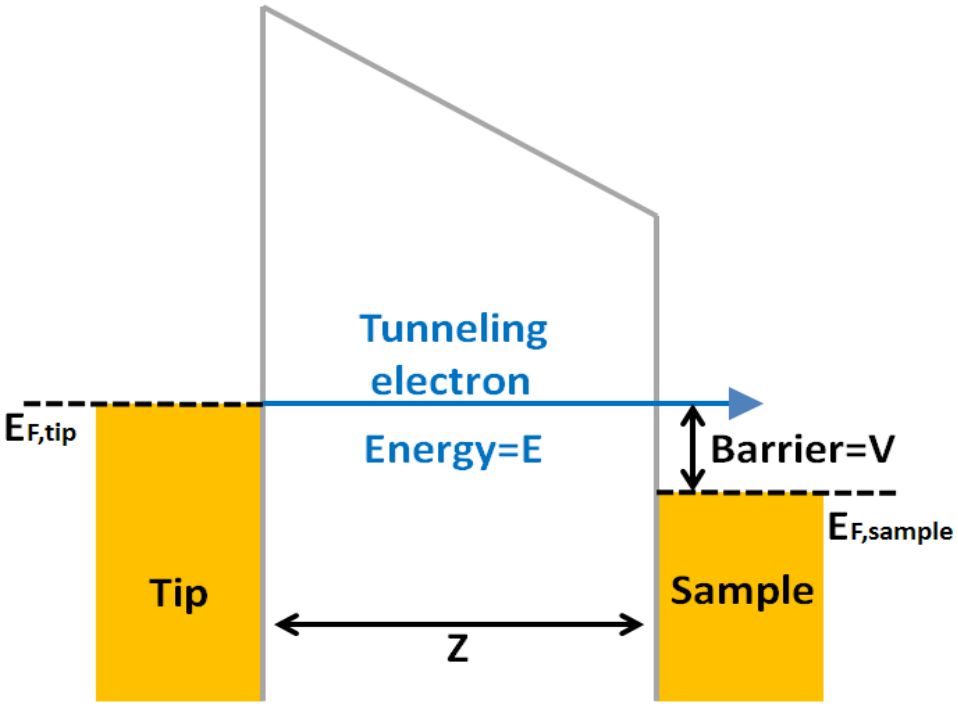


Figure 2.9 An energy level diagram of a one-dimensional electron tunneling junction between the tip and sample.

REFERENCES

(1)Forrest, S. R. *Chem. Rev.* **1997**, *97*, 1793.

(2)Kowarik, S.; Gerlach, A.; Schreiber, F. *J. Phys. Condens. Matter* **2008**, *20*, 184005.

(3)Binnig, G.; Quate, C. F.; Gerber, C. *Phys. Rev. Lett.* **1986**, *56*, 930.

(4)Giessibl, F.; Binnig, G. *Ultramicroscopy* **1992**, *42*, 281.

(5)Ohnesorge, F.; Binnig, G. *Science* **1993**, *260*, 1451.

(6)Giessibl, F. J. *Science* **1995**, *267*, 68.

(7)Bowen, W. R.; Hilal, N. *Atomic Force Microscopy in Process Engineering: An Introduction to AFM for Improved Processes and Products*; Butterworth-Heinemann, 2009.

(8)Prater, C. B.; Maivald, P. G.; Kjoller, K. J.; Heaton, M. G. *Digital Instruments Nanonotes, Santa Barbara, California, USA* **1995**.

(9)Bhushan, B.; Fuchs, H.; Tomitori, M. *Applied scanning probe methods VIII: Scanning probe microscopy techniques*; Springer, 2008; Vol. 8.

(10)Esquivel, D.; Cruz-Cabeza, A. J.; Jiménez-Sanchidrián, C.; Romero-Salguero, F. J. *Microporous Mesoporous Mater.* **2013**, *179*, 30.

(11)Wu, C. C.; Tsay, P. Y.; Cheng, H. Y.; Bai, S. J. *J. Appl. Phys.* **2004**, *95*, 417.

(12)Du, Z.; Yu, Y. L.; Wang, J. H. *Chemistry-A European Journal* **2007**, *13*, 2130.

(13)Bransden, B. H. *Quantum Mechanics, 2/E*; Pearson Education India, 2000.

(14)Binnig, G.; Rohrer, H.; Gerber, C.; Weibel, E. *Phys. Rev. Lett.* **1982**, *49*, 57.

(15)Bai, C. *Scanning tunneling microscopy and its application*; Springer, 2000; Vol. 32.

(16)Cavallini, M.; Bracali, M.; Aloisi, G.; Guidelli, R. *Langmuir* **1999**, *15*, 3003.

(17)Stemmer, A.; Engel, A. *Ultramicroscopy* **1990**, *34*, 129.

(18)Huston, S. M.; Wang, J.; Loth, M. A.; Anthony, J. E.; Conrad, B. R.; Dougherty, D. B. *The Journal of Physical Chemistry C* **2012**, *116*, 21465.

(19)Coombs, J.; Welland, M.; Pethica, J. *Surf. Sci.* **1988**, *198*, L353.

(20)Tersoff, J.; Hamann, D. In *Scanning Tunneling Microscopy*; Springer: 1993, p 59.

(21)Garcia, N. *IBM J. Res. Dev.* **1986**, *30*, 533.

(22)Binnig, G.; Frank, K. H.; Fuchs, H.; Garcia, N.; Reihl, B.; Rohrer, H.; Salvan, F.; Williams, A. R. *Phys. Rev. Lett.* **1985**, *55*, 991.

(23)Binnig, G.; Rohrer, H. *Surf. Sci.* **1985**, *152*, 17.

(24)Koslowski, B.; Dietrich, C.; Tschetschetkin, A.; Ziemann, P. *Phys.Rev. B* **2007**, *75*, 035421.

(25)Passoni, M.; Donati, F.; Bassi, A. L.; Casari, C.; Bottani, C. *Phys.Rev. B* **2009**, *79*, 045404.

(26)Pronschinske, A.; Mardit, D. J.; Dougherty, D. B. *Phys.Rev. B* **2011**, *84*, 205427.

# Chapter 3

# Current Paths in Vacuum-Codeposited Films of $C_{60}$ and P3HT

## 3.1 Introduction

Combinations of donor and acceptor organic materials are increasingly important candidates for optoelectronic devices like organic light emitting diodes (OLED's) and organic photovoltaics (OPV's). In the later class of device, there are two organic materials paradigms: small molecules[1,2] and polymers[3]. The most efficient OPV's to date are solution-cast films of intimately-blended polymers and small molecules based on fullerenes. This device morphology is referred to as a bulk heterojunction, so-called because it utilizes a 3D bicontinuous network of donor and acceptor materials with nanoscale domains that create interfaces throughout the film. Since interfaces are required for exciton dissociation into free carriers in OPV's, the high interfacial area in BHJ's is an obvious advantage. In addition, increasingly sophisticated control of nanoscale domain morphology in these complex blends is likely to allow maximal exciton dissociation efficiency by matching domain size to exciton diffusion length.

Many small molecules have poor solubility and thus are not readily incorporated into such 3D BHJ blends by solution casting. Organic molecular beam deposition (OMBD) of small molecules is very well-developed and has led to good efficiencies in *bilayer* film devices where donor and acceptor materials are deposited sequentially to create one (essentially planar) interface for exciton dissociation[1]. The ability to control film thickness with essentially single layer precision in OMBD is an advantage from the perspective of the possibility of multi-junction "tandem" solar cell architectures[4,5] that might provide important gains in total power conversion efficiency.

In addition to layered devices, significant improvements in efficiency have been reported using OMBD to create complex BHJ-inspired morphologies by co-deposition of mixed donor-acceptor films[6,7]. This takes advantage of the precise control of film composition and morphology by adjusting film growth parameters (substrate temperature, molecular flux etc.). An example of efficiency improvements by compositional control in OMBD is provided by the recent exploration of compositionally *graded* donor-acceptor films[8]. In these devices, control over the rate of change of donor-acceptor composition through the active device region is envisioned as a tool for performance optimization. Recent efforts have greatly increased power conversion efficiencies for small-molecule solar cells to greater than 6.8% by using novel vacuum-deposited "donor-acceptor-acceptor" molecules in conjunction with fullerene-$C_{70}$[9]. Importantly, these new devices control active layer morphology by depositing films in what is called a planar-mixed heterojunction (PM-HJ) cell[10]. This involves pure material films sandwiching a co-deposited mixed layer in an effort to merge the advantages of bilayer and heterojunction cells. The same PM-HJ

geometry has been used with less exotic donor materials coupled to $C_{70}$ to achieve power conversions efficiencies larger than 6%[11].

In addition to efficiency improvements in OPV's, mixed small-molecule films provide important insights into the physical processes controlling charge transport in donor-acceptor systems. Co-deposited mixtures have been shown to exhibit ambipolar transport that strongly suggests their value in understanding the percolative transport of photo-generated carriers in BHJ-like film morphologies[12,13]. Moreover, ambipolar transport observations in small molecule mixtures as well as polymer blends show modified carrier mobilities that do not simply reflect additive mobilities of the pure donor or acceptor materials in isolation[12]. Understanding the impact on charge transport of finely intermixing donor and acceptor organics is a critical fundamental goal in the ongoing search for practical organic photovoltaic technologies.

Recently, the possibility of thermally depositing films of poly-3-hexylythiophene (P3HT) in vacuum has been explored[14,15]. This offers the opportunity to study new morphologies in an important donor-acceptor couple: P3HT and $C_{60}$. Bulk heterojunction OPV's with routinely high power conversion efficiencies can be created by spin casting P3HT mixed with the fullerene-$C_{60}$ derivative [6,6] phenyl $C_{61}$-butyric acid methyl ester (PCBM) from the same solvent[3]. The vacuum co-deposited P3HT:$C_{60}$ analog of the P3HT:PCBM system is the subject of the present work.

Kovacik et al.[14] used vacuum deposition of P3HT to create a bilayer OPV device by sequentially growing first P3HT and then $C_{60}$ (which is likely to be similar from the standpoint of acceptor electronic properties to PCBM[16]). The films of P3HT were observed

to have pinholes and the resulting bilayer devices showed very low power conversion efficiencies, most likely due to shorting of the top $C_{60}$ layer through the P3HT film. In addition, UV-Vis and infrared spectroscopy show a probable reduction in molecular weight of the vacuum deposited P3HT films as well as probable partial decomposition of some alkyl side chains[14].

In this chapter, we report investigations of vacuum *codeposition* of $C_{60}$:P3HT films to create BHJ-like mixed films of varying composition. We observe that the codeposition of $C_{60}$ and P3HT results in smooth surfaces with poor crystallinity. Local transport in the mixed films is visualized by conducting atomic force microscopy (CAFM). It is substantially different than local transport in the canonical P3HT:PCBM blends cast from solution in which having a very sparse density of percolating charge paths. This observation highlights one of the most significant challenges associated with optimizing charge transport in complex heterogeneous molecular systems.

## 3.2 Experimental Methods

Substrates for film growth were 25mm × 25 mm ITO/Glass slides obtained from Sigma-Aldrich with a nominal sheet resistance of 30 Ω/□. The substrates were cleaned by 15 minute sonication in acetone and isopropanol followed by 10 minutes of UV-Ozone treatment. They were subsequently coated with the conducting polymer PEDOT:PSS (Sigma-Aldrich) by spin casting from aqueous solution followed by 15 minute anneal at 120˚C in air, resulting in a ~30 nm PEDOT:PSS film. Substrates were mounted in a turbomolecular-pumped high vacuum deposition system with base pressure ~$3\times10^{-7}$ torr.

Fullerene-$C_{60}$ (Sigma-Aldrich 98%) was loaded as-received into a quartz crucible with a tightly-wrapped tantalum wire heater and outgassed for 1-3 hours. The molecular flux from this source was measured with a quartz crystal microbalance and thickness was calibrated after growth with atomic force microscopy (AFM) across a film edge. Regioregular P3HT was obtained from Sigma-Aldrich and loaded as-received into an alumina crucible heated by a tungsten wire basket. Its flux was also monitored with a quartz crystal microbalance and large transient flux values were frequently observed during growth runs. As reported in other work[15], the pressure in the chamber during P3HT deposition rose to approximately $1 \times 10^{-5}$ torr during film growth. Co-deposited films were grown by heating both $C_{60}$ and P3HT crucibles simultaneously. The individual fluxes were estimated by the calibrated filament current established during individual material growth and the total thickness was estimated using the quartz crystal microbalance and later calibrated by AFM imaging across a film edge.

Solution cast P3HT:PCBM films were created in a dry nitrogen glovebox with < 10 ppm $O_2$ and $H_2O$, using similar processing conditions as reference 23. A solution of ~ 1.0:0.9 P3HT:PCBM in chlorobenzene was stirred overnight at ~70˚C to dissolve. Films were spun-cast from the warm solution at 800 rpm onto PEDOT: PSS/ITO substrates, directly followed by a 2 minute anneal at 110˚C, resulting in a $90 \pm 15$ nm P3HT: PCBM film. Ultraviolet-Visible spectroscopy was carried out on each film with a Shimadzu UV 1601 spectrophotometer using a PEDOT: PSS coated ITO/glass substrate as the transmission baseline. Atomic force microscopy was performed with a commercial instrument (Asylum Research MFP-3D) in ambient environment. Non-contact AFM (NC-AFM) measurements

were carried out using commercial probe tips (Budget Sensors TAP300Al-G) with nominal resonant frequency of 300 kHz and force constant of 40 N/m. Conducting AFM measurements employed a commercial preamplifier (Asylum Research, ORCA) with a fixed gain of $2 \times 10^8$ V/A and platinum-coated tips (Budget Sensors, ContE-G) with a nominal force constant of 0.05 N/m.

## 3.3 Results and Discussion

### 3.3.1 Absorption Spectra

Films were characterized by UV-Vis absorption spectroscopy as shown in Figure 3.1 where a typical spectrum for a $C_{60}$ film shows expected absorption bands at 346 nm and 455 nm. This is in agreement with previous results for vacuum-deposited $C_{60}$ films[17]. The absorption at 455 nm is assigned as the dipole forbidden transition from the HOMO to lower lying degenerate virtual orbitals and the absorption at 346 is assigned as the dipole-allowed transition into higher lying states[18-20].

The absorption spectrum for the vacuum-deposited P3HT film is shown at the bottom of Figure 3.1. In agreement with Kovacik et al.[14], the absorption peak at 420 nm is blue-shifted and broadened when compared with typical spectra measured for solution-cast P3HT thin films[21]. The general location and lack of vibronic structure suggests very poor crystalline order or aggregation in these films. Moreover, the blue shift compared to noncrystalline solution-grown films[21] supports the hypothesis of a decrease in conjugation length due to the vacuum evaporation process. In our experiments, P3HT films were

observed to be dark yellow while the material remaining in the alumina crucible after deposition was the dark red color typically observed for solution-cast P3HT films.

Mixed films with approximately 20% P3HT exhibit absorption spectra still dominated by the fullerene-derived absorption peaks. The only evidence for the P3HT content is a slight change in the shape of the weaker 455 nm peak that is consistent with a contribution from the 420 nm P3HT peak. There is no evidence of significant electronic interaction between the materials in the mixed film as expected for relatively weakly interacting organic molecular solids. However, there is a slight blue-shift of the sharp $C_{60}$ absorption from 346 nm in the pure $C_{60}$ film to 343 nm in the film with 20% P3HT co-deposition. We attribute this change to a reduction in $C_{60}$ crystallite size in the film due to intermixing with P3HT. The trends of enhanced contribution from the P3HT peak near 420 nm and small blue shifts of the $C_{60}$ absorption continue with increasing P3HT content as shown in Figure 3.1. For a 5:1 P3HT:$C_{60}$ composition, the fullerene absorption occurs at ~337 nm, indicating a blue shift of 9 nm compared to pure $C_{60}$ and thus a significant disruption of fullerene crystallinity.

### 3.3.2 Atomic Force Microscopy

Figure 3.2 shows film topography measured by NC-AFM for vacuum-deposited P3HT films. Figure 3.2a is a large scale (20 μm × 20 μm) image that shows a very smooth film surface with a root-mean-square (rms) roughness of only 0.71 nm and a few isolated holes. On smaller scales in regions with no holes, as shown in Figure 3.2b, the rms surface roughness is very low at only ~ 0.31 nm. This smoothness is distinct from the rougher

morphology reported by Kovacik et al[14], a difference which may be attributable to differences in roughness of the starting ITO on glass substrates in the two cases.

Figure 3.3 shows NC-AFM topography measurements for mixed films of increasing $C_{60}$ composition (Figure 3.3a-c) and a pure $C_{60}$ film (Figure 3.3d). Fullerene-$C_{60}$ films grown on a room temperature PEDOT: PSS/ITO substrate shows a granular surface morphology with typical grain size of about 20-50 nm and a typical rms roughness of ~ 1nm. The 1:1 and 5:1 mixed P3HT:$C_{60}$ films exhibit smooth morphologies that are similar to other finely intermixed vacuum codeposited films[7] and similar in rms surface roughness to the pure P3HT films. Surface roughness of the mixed films tends to increase with $C_{60}$ content and is particularly evident for the 1:5 P3HT:$C_{60}$ films in Figure 3.3c which exhibit mounds on the surface. This can be explained as the result of a strong tendency toward phase segregation of small fullerene crystallites. Such a picture is also consistent with the composition-dependent shift of the fullerene absorption peak near 345 nm in Figure 3.1. As $C_{60}$ segregates into nanoscale crystallites with increasing mass composition, this peak shifts to longer wavelengths. Fullerene phase segregation is a well-documented phenomenon in both bulk heterojunctions and mixed small molecule films[13].

### 3.3.3 Conducting Atomic Force Microscopy Measurements

One of the critical issues in the operation of an organic solar cell is to understand and optimize the charge conduction pathways out of the light-absorbing region. This is ultimately related to both the short circuit current and the fill factor, which each contribute linearly to the power conversion efficiency of the cell[2]. Conducting AFM can provide local

information about the spatial distribution of these crucial conducting pathways. This has been carried out very extensively for solution-cast BHJ solar cell materials and shows the strong inhomogeneity of current pathways in such devices[22,23]. It has also been used to visualize current pathways in nanostructured organic photovoltaic systems[24] and novel small-molecule fullerene blends[25].

An example of topography and CAFM images for a *solution-cast* P3HT:PCBM blend is shown in Figure 3.4. These measurements exhibit the essential features that have already been reported by Ginger and co-workers[23]. Significant charge transport at both tip polarities can be seen and there are spatially-varying current paths throughout the local area. The spatial distribution of current paths is different for different tip polarities dominantly reflecting the differences in percolated current paths for electrons compared to holes. Despite clear spatial inhomogeneity, almost every point in the CAFM image shows measureable dark current, indicating the presence of numerous efficient charge percolation paths. This high areal density of relatively efficient percolation paths will be seen below to contrast with vacuum-deposited films especially for negative polarities corresponding to electron injection from the tip.

The local current maps measured by CAFM for vacuum-deposited mixed films of P3HT:$C_{60}$ in an approximately 1:1 ratio are very different than their BHJ counterparts (Figure 3.5a-c). As seen in Figure 3.5b and 3.5c, the magnitude of the local current at both polarities in the mixed films is at least an order of magnitude lower than in the solution-cast films, even though the bias applied between the tip and sample is larger in absolute value. More significantly, the current pathways are sparser as a function of position across the film

and spatial variations in current correspond to a larger fraction of the area-averaged current than in Figure 3.4b-c. Many locations in the imaged area do not show a dark current above the (~ 1 pA) noise floor of the preamplifier. This suggests a much more limited number of percolation pathways and less efficient charge transport compared to the BHJ morphology in Figure 3.5. This sparseness of percolation paths is especially apparent for the negative bias CAFM image shown in Figure 3.5c. We attribute this fact to the poor crystallinity of the fullerene component of the films that was already indicated by optical spectroscopy.

The CAFM data in Figure 3.5 provide a nanoscale perspective on the generally poor charge transport properties that have been a serious problem in the use of vacuum-deposited small molecules in mixed film OPV's, as shown in references 2 and 7. This is intimately tied to the nanoscale film morphology and crystallinity in these often amorphous systems and highlights the crucial nature of polymer crystallinity in creating conduction pathways for the charges. For example, phthalocyanine: $C_{60}$ OPV's created by vacuum co-deposition can have low short-circuit currents and fill factors that were found to be improved by annealing processes that promote fullerene segregation and crystallization[26-28]. In our experiments, where crystallinity of both donor and acceptor materials is expected to be poor, charge extraction from active device regions would be expected to be a serious limiting factor in efficiency. The important insight here is the strongly filamentary nature of the conduction paths apparent in CAFM measurements. Such current paths are not only inefficient but also could promote device degradation due to local heating or current-induced reactivity.

## 3.4 Summary and Conclusions

In summary, we have prepared vacuum co-deposited films of P3HT and fullerene-$C_{60}$. Vacuum-deposited P3HT shows poor crystallinity and some evidence of reduced conjugation length in agreement with previous reports. Co-deposition with $C_{60}$ disrupts the fullerene crystallinity as evidenced by the shift of the fullerene absorption peak near 340 nm. AFM studies show smooth P3HT films that become progressively rougher at the surface with increasing $C_{60}$ content. Conducting AFM measurements show very low current levels and spatially-sparse percolation paths through 1:1 mixed films. This contrast sharply with the more uniform current paths through a solution cast heterojunction of P3HT: PCBM.

Our study provides the opportunity for comparison of local charge transport in vacuum-deposited mixed films with analogous solution-cast bulk-heterojunctions. The more tenuous current distributions in vacuum-deposited mixed films highlight the optimization of charge transport in this family of organic materials as a very significant challenge for ongoing efforts at organic solar cell creation. Importantly, it also suggests that electron transport through poorly-crystalline fullerene components could be a limiting factor in charge transport in mixed small molecules films.

FIGURES

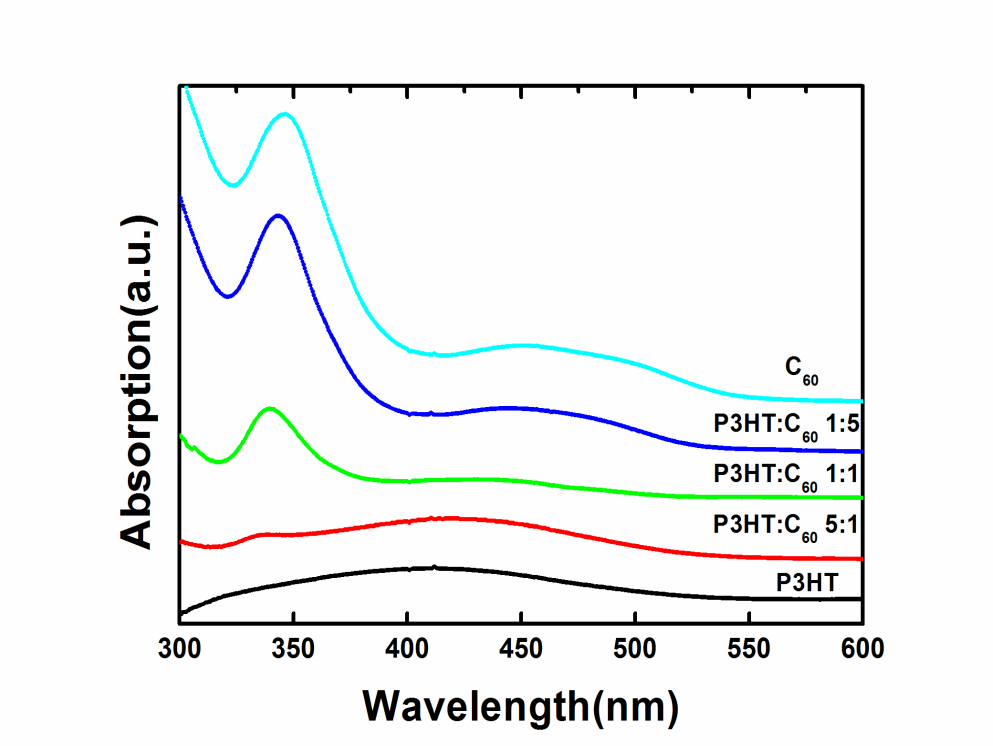


Figure 3.1 Ultraviolet-Visible absorption spectra for P3HT:$C_{60}$ films of different compositions. Fullerene content increases from bottom to top as indicated and curves are offset for clarity.

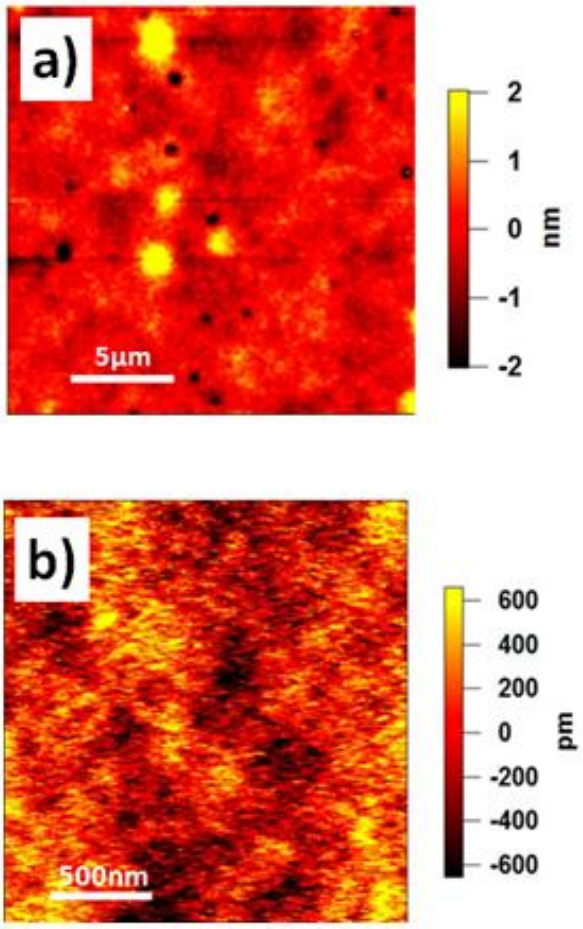


Figure 3.2 NC-AFM images of vacuum-deposited P3HT on PEDOT: PSS/ITO. (a) 20 µm × 20 µm image with a rms roughness of 0.70 nm; (b) 2 µm × 2 µm image with a rms roughness of 0.31 nm.

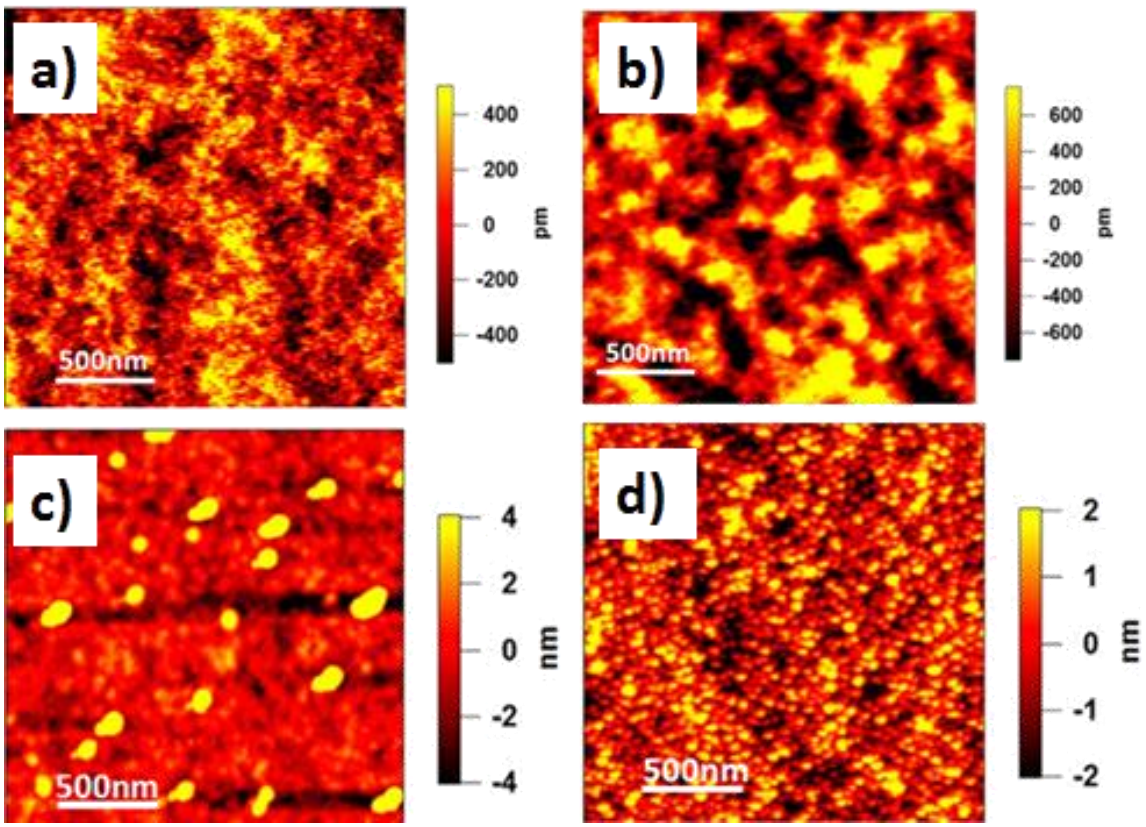


Figure 3.3 NC-AFM images (2 μm × 2 μm) of vacuum deposited P3HT:$C_{60}$ films with increasing fullerene content. (a) 5:1 P3HT:$C_{60}$; (b) 1:1 P3HT:$C_{60}$; (c) 1:5 P3HT:$C_{60}$; (d) pure $C_{60}$ film.

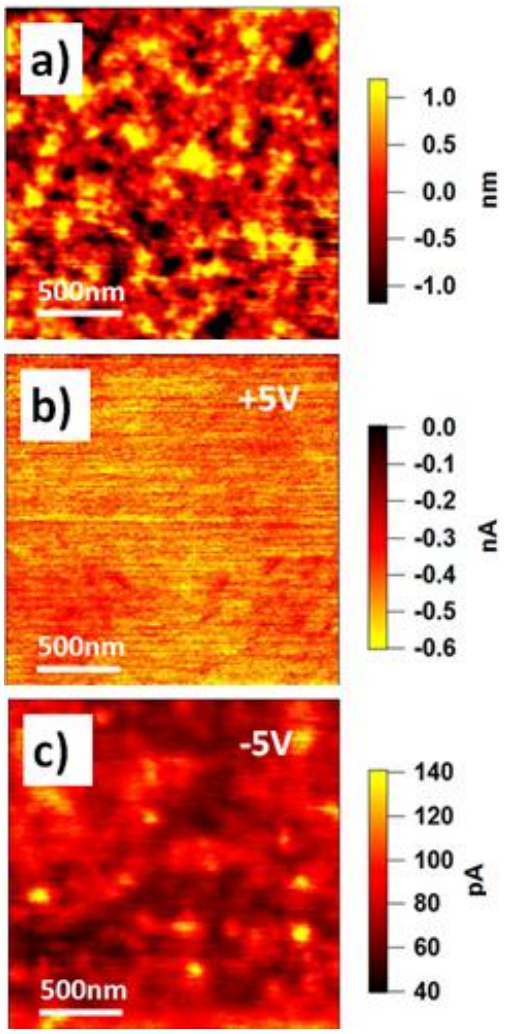


Figure 3.4 Contact-mode AFM and conducting AFM of a 2 μm × 2 μm region of 1:1 solution-cast films of P3HT:PCBM. (a)Topography measured at 0V; (b)Dark current maps measured by conducting AFM at +5V; (c)Dark current maps measured by conducting AFM at -5V.

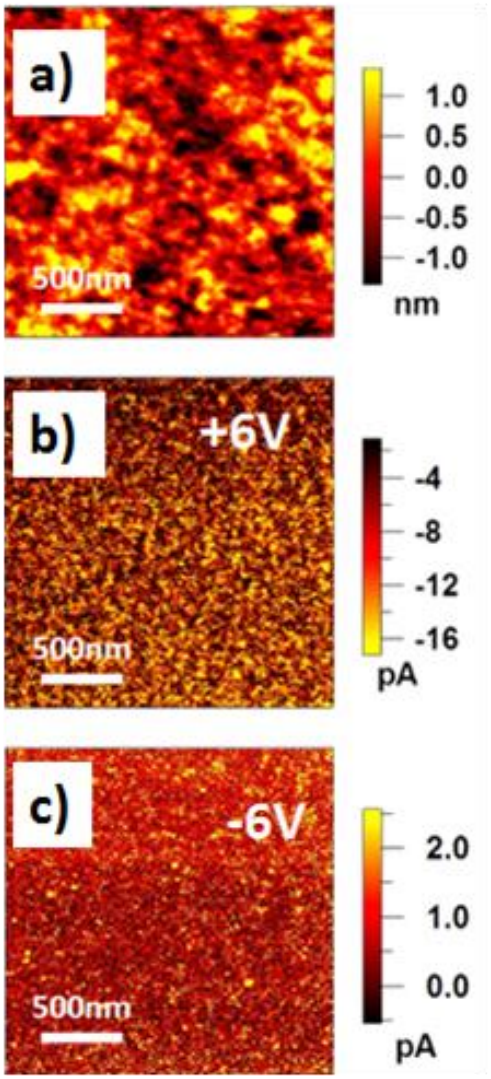


Figure 3.5 Contact-mode AFM and conducting AFM of a 2 μm × 2 μm region of 1:1 vacuum co-deposited films of P3HT: $C_{60}$. (a)Topography measured at 0V; (b)Dark current maps measured by conducting AFM at +6 V; (c) Dark current maps measured by conducting AFM at -6 V.

REFERENCES

(1)Peumans, P.; Yakimov, A.; Forrest, S. R. *J. Appl. Phys.* **2003**, *93*, 3693.

(2)Riede, M.; Mueller, T.; Tress, W.; Schueppel, R.; Leo, K. *Nanotechnology* **2008**, *19*, 424001.

(3)Deibel, C.; Dyakonov, V. *Rep. Prog. Phys.* **2010**, *73*, 096401.

(4)Drechsel, J.; Mannig, B.; Kozlowski, F.; Pfeiffer, M.; Leo, K.; Hoppe, H. *Appl. Phys. Lett.* **2005**, *86*, 244102.

(5)Xue, J. G.; Uchida, S.; Rand, B. P.; Forrest, S. R. *Appl. Phys. Lett.* **2004**, *85*, 5757.

(6)Peumans, P.; Uchida, S.; Forrest, S. R. *Nature* **2003**, *425*, 158.

(7)Rand, B. P.; Xue, J. G.; Uchida, S.; Forrest, S. R. *J. Appl. Phys.* **2005**, *98*, 124902.

(8)Pandey, R.; Holmes, R. J. *Adv. Mater.* **2010**, *22*, 5301.

(9)Chen, Y.-H.; Lin, L.-Y.; Lu, C.-W.; Lin, F.; Huang, Z.-Y.; Lin, H.-W.; Wang, P.-H.; Liu, Y.-H.; Wong, K.-T.; Wen, J.; Miller, D. J.; Darling, S. B. *Journal of the American Chemical Society* **2012**, *134*, 13616.

(10)Xue, J.; Rand, B. P.; Uchida, S.; Forrest, S. R. *Adv. Mater.* **2005**, *17*, 66.

(11)Xiao, X.; Zimmerman, J. D.; Lassiter, B. E.; Bergemann, K. J.; Forrest, S. R. *Appl. Phys. Lett.* **2013**, *102*, 073302.

(12)Tuladhar, S. M.; Poplavskyy, D.; Choulis, S. A.; Durrant, J. R.; Bradley, D. D. C.; Nelson, J. *Advanced Functional Materials* **2005**, *15*, 1171.

(13)Opitz, A.; Wagner, J.; Brutting, W.; Hinderhofer, A.; Schreiber, F. *Phys. Status Solidi A-Appl. Mat.* **2009**, *206*, 2683.

(14)Kovacik, P.; Sforazzini, G.; Cook, A. G.; Willis, S. M.; Grant, P. S.; Assender, H. E.; Watt, A. A. *ACS Appl. Mater. Interfaces* **2010**, *3*, 11.

(15)Wei, H.; Scudiero, L.; Eilers, H. *Appl. Surf. Sci.* **2009**, *255*, 8593.

(16)Kanai, Y.; Grossman, J. C. *Nano Lett.* **2007**, *7*, 1967.

(17)Kratschmer, W.; Lamb, L. D.; Fostiropoulos, K.; Huffman, D. R. *Nature* **1990**, *347*, 354.

(18)Ajie, H.; Alvarez, M. M.; Anz, S. J.; Beck, R. D.; Diederich, F.; Fostiropoulos, K.; Huffman, D. R.; Kraetschmer, W.; Rubin, Y.; et al. *The Journal of Physical Chemistry* **1990**, *94*, 8630.

(19)Gasyna, Z.; Schatz, P. N.; Hare, J. P.; Dennis, T. J.; Kroto, H. W.; Taylor, R.; Walton, D. R. M. *Chemical Physics Letters* **1991**, *183*, 283.

(20)Orlandi, G.; Negri, F. *Photochem. Photobiol. Sci.* **2002**, *1*, 289.

(21)Liu, W. L.; Liu, R. G.; Wang, W.; Li, W. W.; Liu, W. Y.; Zheng, K.; Ma, L.; Tian, Y.; Bo, Z. S.; Huang, Y. *J. Phys. Chem. C* **2009**, *113*, 11385.

(22)Coffey, D. C.; Reid, O. G.; Rodovsky, D. B.; Bartholomew, G. P.; Ginger, D. S. *Nano Letters* **2007**, *7*, 738.

(23)Pingree, L. S. C.; Reid, O. G.; Ginger, D. S. *Advanced Materials* **2009**, *21*, 19.

(24)Kamkar, D. A.; Wang, M. F.; Wudl, F.; Nguyen, T. Q. *Acs Nano* **2012**, *6*, 1149.

(25)Guide, M.; Dang, X. D.; Nguyen, T. Q. *Adv. Mater.* **2011**, *23*, 2313.

(26)Suemori, K.; Miyata, T.; Hiramoto, M.; Yokoyama, M. *Japanese Journal of Applied Physics* **2004**, *43*, L1014.

(27)Pfuetzner, S.; Mickel, C.; Jankowski, J.; Hein, M.; Meiss, J.; Schuenemann, C.; Elschner, C.; Levin, A. A.; Rellinghaus, B.; Leo, K.; Riede, M. *Organic Electronics* **2010**, *12*, 435.

(28)Schultes, S. M.; Sullivan, P.; Heutz, S.; Sanderson, B. M.; Jones, T. S. *Materials Science and Engineering: C* **2005**, *25*, 858.

# Chapter 4

# Intrinsic electronic disorder observed on α-NPD/Au(111) film by STM and STS

## 4.1 Background and Motivation

N,N'-Di-[(1-naphthyl)- N,N'-diphenyl]-1,1'-biphenyl)-4,4'-diamine (α-NPD) is a quite commonly used small molecule material in organic electronics, which has many applications. For instance, it can be utilized as a hole transport material in organic-inorganic semiconductor heterojunctions[1], a hole-transport emissive layer for organic light emitting diodes (OLED's)[2], an electron blocking layer between emissive layers in OLED's[3], and a host material for white-light-emitting organic electroluminescent devices[4].

It is an important question to address what factors will affect charge transport in organic electronics. It has been found that the first two molecular layers next to the dielectric interface dominate the charge transport and second layer is crucial as it provides efficient percolation pathways for carriers generated in both the first and second layers from quantitative analysis[5]. So the morphology, conformation and electronic states of organic molecules in the first few layers on a substrate will be of great interest to characterize in

order to find new methods to improve charge transport characteristics of organic electronic devices.

The α-NPD molecule is often observed to form strongly disordered thin films[6,7]. A recent study by van Mensfoort et al. took advantage of this fact to compare the use of different quantitative models of disorder to explain transport measurements through α-NPD diodes[8]. They found some evidence that there are energetic correlations in the electronic disorder in these films, which is different than the usual assumption of "Gaussian" disorder as described in detail in Chapter 1. Correlated disorder can arise due to direct dipole interactions between nearby molecules that lead to long-range electronic interactions[9]. However, the origin of this disorder at the molecular scale is still unknown and this information is quite important and necessary for future organic device performance improvement.

In this chapter, scanning tunneling microscopy (STM) and scanning tunneling spectroscopy (STS) will be utilized to study α-NPD molecules adsorbed on Au(111) surface. A wide variety of molecular conformations and local packing structures have been observed consistent with expectations of strong disorder in this system based on previous work. Electronic differences are identified between different conformations of α-NPD on Au(111) and we propose that variability in molecular conformations is the primary source of electronic disorder in α-NPD thin film devices.

## 4.2 Experimental Methods

α-NPD (assay:96%) was purchased from Sigma Aldrich and no further purification was done before use. α-NPD deposition was performed in the preparation chamber (base pressure $<1\times10^{-7}$ Torr) connected to the Omicron ultra-high vacuum main STM chamber (base pressure $\sim5\times10^{-11}$ Torr) by a gate valve described in Chapter 2. α-NPD was deposited on the clean Au(111) substrate by thermal evaporation from a quartz crucible with tantalum heater wire wrapped around it and the deposition rate was monitored by a quartz crystal microbalance(QCM). The Au(111) crystal substrate was cleaned by $Ar^+$ ion sputtering at 1kV and annealing to about 700K inside the main chamber. Deposition rates were approximately 0.1 Å/s and three sequential 4 sec depositions were performed to investigate the coverage-dependent structure and morphology of α-NPD molecular layers. All the Scanning Tunneling Microscopy (STM) and Scanning Tunneling Spectroscopy (STS) was carried out at 131K, with the STM cooled by liquid nitrogen (Introduced in Chapter 2).

## 4.3 Results and discussion

### 4.3.1 The $22\times\sqrt{3}$ R30° Au(111) Herringbone substrate

Before we deposited α-NPD on the Au(111) crystal substrate, the substrate itself was confirmed to be clean by direct STM imaging. After $Ar^+$ ion sputtering and annealing cycles, the substrate was scanned by STM both in large and small area scales. Figure 4.1 shows the morphology of clean Au(111) surface. In Figure 4.1A, a 279 nm $\times$ 279 nm area of the

Au(111) surface is shown, from which flat Au terraces can be seen with widths more than 100 nm. Also no impurities can be observed from the topographic image, which indicates that the substrate is clean. Smaller scale topographic images show the well-known herringbone reconstruction of the Au(111) surface with only minor possible point-like contaminants visible, as shown in Figure 4.1B.

In this 74.4nm ×74.4nm area of Figure 4.1B, the key features of the Au(111) 22x $\sqrt{3}$ R30 °herringbone reconstruction can be observed[10]. This herringbone reconstruction is the result of competition between two effects: (i) the preferred surface bond length is less than that in the bulk; (ii) the surface atoms prefer to sit in the minima of the potential due to the substrate atoms, so remain in registry with the bulk. On Au(111) surface, there are two kinds of competing sites for surface atoms: The fcc site (ABCABC… stacking) and hcp site (ABAB…stacking). The surface bond length can be reduced by occupying both fcc and hcp sites. The alternating domains of fcc and hcp structures are separated by soliton walls. The atoms in the soliton wall regions are packed closer together, resulting in the surface corrugation observed by STM. The width of fcc area is larger than that of hcp area due to the fact that fcc stacking is lower in energy than hcp stacking[11].

### 4.3.2 Survey of α-NPD Adsorption Structures on Au(111)

Growth of α-NPD on Au(111) results in multiple coexisting surface structures at the submonolayer coverage that we observed. This is the first indication that the structural disorder known to be present in many technologically-relevant α-NPD films is also reflected in the ultrathin films considered in our experiment. In this section, we provide a brief survey

of some of the different structures and morphologies that can be found in these adsorption systems and then focus attention on a comparison of ordered structures called "broad-single-row" and "disordered" structure.

In Figure 4.2, three different surface structures arising from α-NPD are observed in one single image simultaneously. The region outlined in green indicates the first layer where a 2D molecular "gas" domain coexists with small patches of locally stable molecular aggregates. The regions outlined in blue and red indicate the "single-row" and "double-row" structures respectively.

The molecules in the low density "2D gas phase" move rapidly during each STM line scan and so cannot be clearly resolved in topographic images. Nevertheless, their presence is evident by the modification of the appearance of the substrate herringbone reconstruction. Comparison of Figure 4.1 and 4.2 shows that low coverage α-NPD adsorption results in the soliton walls of the herringbone pattern inverting contrast. The presence of the 2D gas moving rapidly in the fcc and hcp domains makes the soliton walls appear as apparent depressions in Figure 4.2 and also in Figure 4.3, while on a clean surface they are always observed as apparent protrusions (Figure 4.1 B). The presence of 2D gas phase at low molecular surface coverage is common for adsorption of organic molecules on metals and has been reported for many molecules, such as pentacene[12] and acridine carboxylic acid[13].

Figure 4.3 shows a STM image of low density region of α-NPD in which the 2D gas phase as well as stable clusters can both be viewed on the Au(111) surface. If we look more closely at Figure 4.3, we can notice that only the molecules on the wider fcc areas can be clearly imaged as stable clusters.

Figure 4.4 shows STM images in which we can observe a single α-NPD molecule and propose plausible conformations of molecules in stable clusters on the Au(111) surface.

We have identified two different varieties of stable clusters of α-NPD molecules: (1) three-lobe pattern, as shown in the blue square in Figure 4.4A; Each lobe is one molecule, the higher potion of the molecule gather in the middle; and (2) windmill pattern, as shown in the yellow square in Figure 4.4A. In Figure 4.4(B) and 4.4(C), we propose a plausible molecule conformation for each type of cluster. For the three-lobe pattern, as indicated by front and top view shown in Figure 4.4(D), α-NPD molecule stands both on phenyl and naphthyl groups of one side (highlighted by red circles), the other pair of phenyl and naphthyl groups will point up and be the highest portion of molecule (highlighted by blue circle), brightest in the middle as observed in our STM measurements. On the other hand, we propose the windmill pattern is formed from molecules in the conformation as shown in Figure 4.4(C). Each elongated bright feature in Figure 4.4C is a single molecule, and each molecule is orientated like the one shown in Figure (E). Both the phenyl groups will be standing on the surface while naphthyl groups on the far-from-surface side and try to align with the biphenyl backbone. The difference between the brighter and darker tubes may be due to the situation in which both naphthyl groups on the surface side instead of phenyl groups.

One more thing to be mentioned is that the molecule alignment is fixed with only three directions and the angle between each direction is 120 °. This comes from the templating effect of the underlying Au(111) fcc area. This surface templating effect is very common, for example the second pentacene monolayer orientation on Ag(111)[14] and bithiophene on Ni(110) 4×1-S surface[15].

After introducing the gas-phase pattern on the α-NPD first molecule layer, exploring other more dense condensed-phase patterns will be our next goal. Three different patterns will be surveyed below: narrow-single-row, broad-single-row and disordered structures.

Figure 4.5(A) is a large-area STM image of 27.9nm×27.9nm dimensions of narrow-single-row structure. The molecular conformation can be illustrated more explicitly from the zoom-in area of Figure 4.5(A) as shown in Figure 4.5(B), with crystal parameters a~1.75nm and b~1.45 nm shown in Figure 4.5(B). The α-NPD molecule will lie down on Au(111) surface with the biphenyl backbone, staying flat to acquire a large contact between molecule and substrate. On the other side, the two pairs of phenyl and naphthyl groups will point up to be the highest portion of the molecule, as circled in Figure 4.5(C), and are imaged as bright lobes in STM similar to the side-arms in our recent diF-TES-ADT study[16]. For α-NPD there are numerous ways to have molecule-substrate interaction between π-electrons and the metal substrate, which leads to different conformations. That is to say, standing and lying molecules can both provide comparably strong substrate-molecule interaction, even though standing up may have slightly smaller interaction but it allows more molecules per unit area.

Another first layer pattern is called the "broad-single-row" pattern, as shown in Figure 4.6. Figure 4.6(A) is a large area image which shows single-row pattern and 4.6(B) is a zoom-in area with our assignment of a molecular conformation. The 2D crystal parameters of broad-single-row are a~ 1.14nm along the row and b~2.45nm between rows, approximately 1nm larger than that of narrow-single-row pattern. Detailed side view and top view of molecule conformation is shown in Figure 4.6(C). Instead of lying down, each

molecule in this pattern is standing up on one side of phenyl and naphthyl groups, while the other side groups are protruding out, shown as bright dots.

The last pattern to be discussed in first layer is disordered structure as shown in Figure 4.7. The molecules are assembled together in a disorderly arrangement and no specific molecular conformation could be assigned. This disordered pattern is brighter than surrounding single-row patterns, indicating that molecules are standing up rather than lying down similar to the broad-double-row pattern in Figure 4.6. In addition, height variations for features within the disordered structure suggest variable molecular confirmation within these domains.

### 4.3.3 Electronic Impact of Structural Disorder in the first layer of α-NPD/Au(111)

With so many different structural domains coexisting on the same sample, we have the opportunity to study the molecular-scale origins of electronic disorder and the relationship between local molecular packing, molecular conformation, and interfacial electronic structure. Due to the fact that α-NPD is an efficient hole-transporting molecule, we will focus on its Highest Occupied Molecular Orbital (HOMO) in the following discussions.

No HOMO states can be observed by STS measurements of the narrow-single-row pattern shown in Fig. 4.5. This can be explained by the broadening of molecular orbitals due to electronic interactions with the metal substrate[17] as described in Chapter 1 of this thesis. In the narrow-single-row pattern, molecules are lying down on the Au(111) surface and this good contact will induce strong molecular orbital broadening effects so that HOMO states will not be observed in our STS study.

In contrast, due to the weaker molecule-metal interaction in the more upright conformations inferred from Figure 4.6 and 4.7, molecular π states are decoupled from the substrate, the HOMO can be clearly measured as shown in Figure 4.8 for the broad-single-row and disordered molecules.

In Figure 4.9, histograms of HOMO locations on broad-single-row pattern and disordered pattern are shown. HOMO locations are determined from normalized dz/dV curves using the method proposed by Pronschinske et al.[18], and introduced in Chapter 2 of this thesis. The number of different molecules measured is 49 for the broad-single-row and 133 for the disordered pattern. To help us understand the distribution of HOMO positions, fits of each histogram to a Gaussian distribution are also shown in Figure 4.9. For the broad-single-row pattern, the best fit results in a center =-0.80±0.01 eV, σ=0.03±0.01 eV with a reduced chi squared of 0.31; for the disordered pattern, the fit results in a center=-0.90±0.01 eV, σ=0.09±0.01 eV with a reduced chi squared of 0.71. But the width of distributions σ stated above ($\sigma_{observed}$) involves the effect of experimental uncertainty $\sigma_{experiment}$. Assuming electronic disorder and experimental uncertainty both follow a Gaussian distribution, the width of electronic disorder

$$\sigma_{electronic} = \sqrt{\sigma^2_{observed} - \sigma^2_{experiement}} \,. \qquad (4.1)$$

We obtain $\sigma_{experiment}$ by measuring HOMO energy on one single site of each molecule repeatedly for 64 different molecules, plotting the histogram of single site energy deviations from their mean value and fitting the histogram by Gaussian distribution, as shown in Figure 4.10. The experimental uncertainty $\sigma_{experiment}$ acquired from this fitting is

$\sigma_{experiment} = 0.02 \pm 0.01$ eV with a reduced chi squared of 3.4.

We can notice the measured disorder parameter of broad-single-row pattern is very close to the experimental uncertainty, and it suggests no electronic disorder in this pattern. This is consistent with the long range order evident from direct STM imaging. For the disordered structure, application of equation (4.1) leads to a value $\sigma_{electronic} = 0.09 \pm 0.01$ eV, indicating a negligible contribution of intrinsic measurement uncertainty to the width of the HOMO distribution. We therefore infer that the value of $\sigma_{electronic}$ for the disordered structure is of significant physical interest in understanding the microscopic origin of electronic disorder in α-NPD devices. It is interesting to note that the value of this parameter is similar to the range of values reported in the literature reported Gaussian density of electronic states ($\sigma$=0.05-0.12 eV)[7,8,19-21] in a-NPD device experiments. This indicates that the STM/STS captures some of the essential origin of disorder in typical films. As already mentioned, the STM observation in Fig. 4.7 suggest a distribution of molecular conformations. We propose that this is the origin of the broad HOMO distribution.

In addition, the likelihood of variable molecular conformation can be used to explain the observation that the HOMO of disordered pattern is approximately 0.1 eV farther away from Fermi level than ordered broad-single-row pattern. The Gaussian fit provides an intuitive impression that the HOMO positions are different for broad-single-row and disordered patterns. Further statistical evidence is obtained by using a Welch t-test[22]. This confirms that the mean HOMO position for broad-single-row and disordered patterns are quite different: the means of the two sets of data are not equal in 99% confidence interval with negligibly small p-values for the null hypothesis of equal means.

The origin of the different HOMO positions for these two structures is the difference in molecular conformation that was already proposed based on STM imaging. We infer that the conformation of molecules in Fig 4.6 is different than the majority of conformations present in the molecules and thus leads to a different HOMO energy. In our system of α-NPD on Au(111), the phenyl and naphthyl groups of the α-NPD molecule can rotate around the σ bonds and the biphenyl backbone can twist around its axis as well. These conformational differences could induce different overlap of π states of the backbone and the phenyl/naphthyl groups, inducing energetic change for different adsorption conformations.

We finally remark that the impact of conformational differences on electronic structure, has also been observed for the HOMO in the rubrene/Au(111) system[23]. Due to the fact that the tetracene backbone of the rubrene molecule can twist around its axis and the phenyl groups can rotate around the σ bonds, different conformers exist. STS measurements of the different molecular conformers show that they are characterized by different HOMO energies. Combined with our study it is thus reasonable to suggest that organic semiconductors with significant flexibility in bond angles will often exhibit energetic disorder due to random molecular conformations in thin films.

More quantitatively, the HOMO shifts in α-NPD are significantly smaller than those observed for different conformers of rubrene[23]. The HOMO difference for different rubrene conformers is larger than 1eV while our observation of HOMO difference is only up to 0.5 eV for the α-NPD molecule. This difference can be understood based on the fact that the twisting reported in rubrene is a much more dramatic disruption of the π system[24] than the bond rotations in α-NPD.

As stated above, our observation on HOMO energy change on different conformers of α-NPD molecules, has contributed another evidence that intrinsic conformational effects can be a significant molecular scale source of energetic disorder.

## 4.4 Summary and Conclusions

In this chapter, we have reported observations of the topography of different conformations of α-NPD molecules on Au(111) substrate using scanning tunneling microscopy. The most important conclusion is that variable conformations can be clearly identified in the same film and that these changes in molecular geometry lead to a distribution of electronic states consistent with the electronic disorder inferred in macroscopic devices. By utilizing scanning tunneling spectroscopy, we find that HOMO of an ordered broad-single-row structure and the HOMO of a disordered pattern are different due to different conformations of molecules in these two structures. Within the disordered structure, a very broad distribution of HMO energies is found that is similar to that seen in device measurements. This observation provides a clear view that energetic disorder in organic electronics could come from the intrinsic molecular conformational differences. This recognition will contribute to a predictive understanding of how single molecule structure determines macroscopic device characteristics in the complex and still growing field of organic electronics.

FIGURES

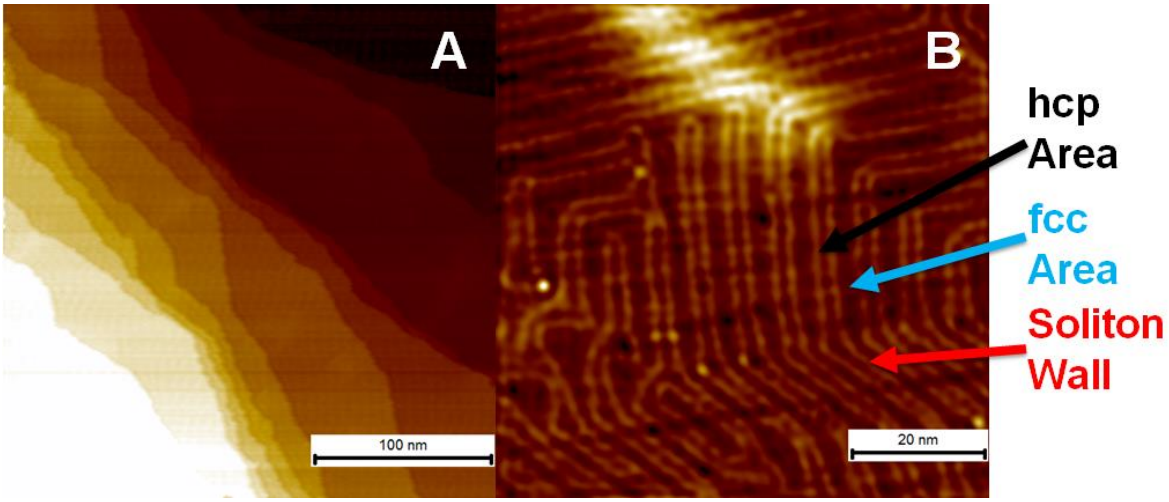


Figure 4.1: STM images of clean Au(111) substrate. (A) 279nm ×279nm, acquired at 10pA with 1V bias at 131K; (B) 74.4nm ×74.4nm, acquired at 1pA with 1V bias at 131K.

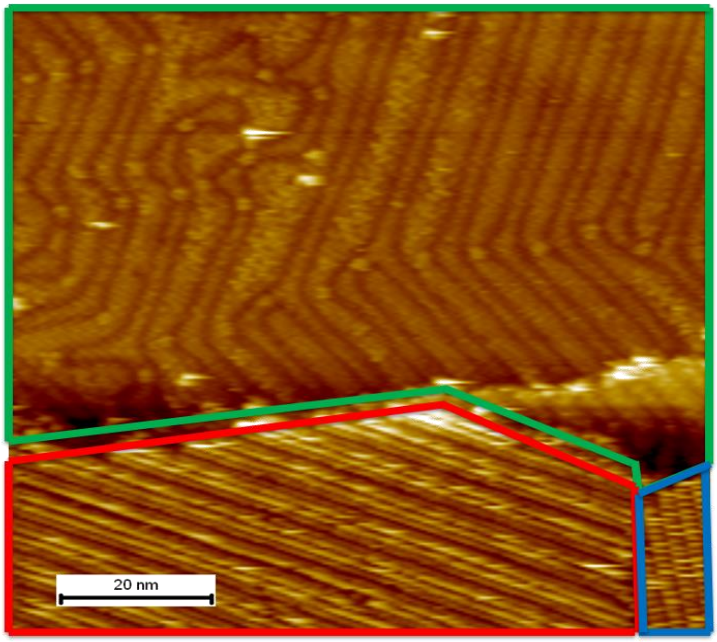


Figure 4.2: STM images of submonolayer α-NPD on Au(111) substrate. Size=93nm×93nm, acquired at 1pA with -1V bias at 131K, three different phase domains are indicated by different color squares.

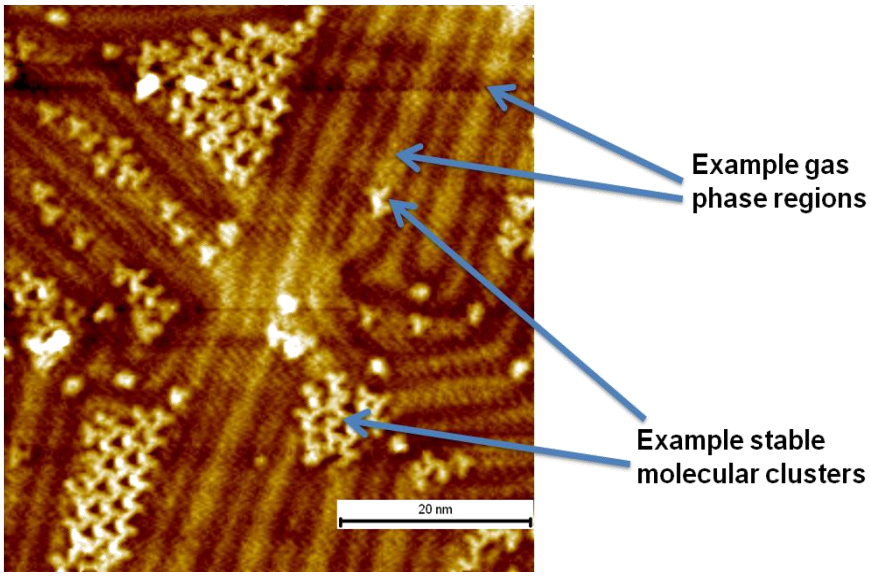


Figure 4.3: Zoom-in STM images of submonolayer α-NPD on Au(111) substrate. Size= 55.8nm ×55.8nm, acquired at 1pA with -1V bias at 131K.

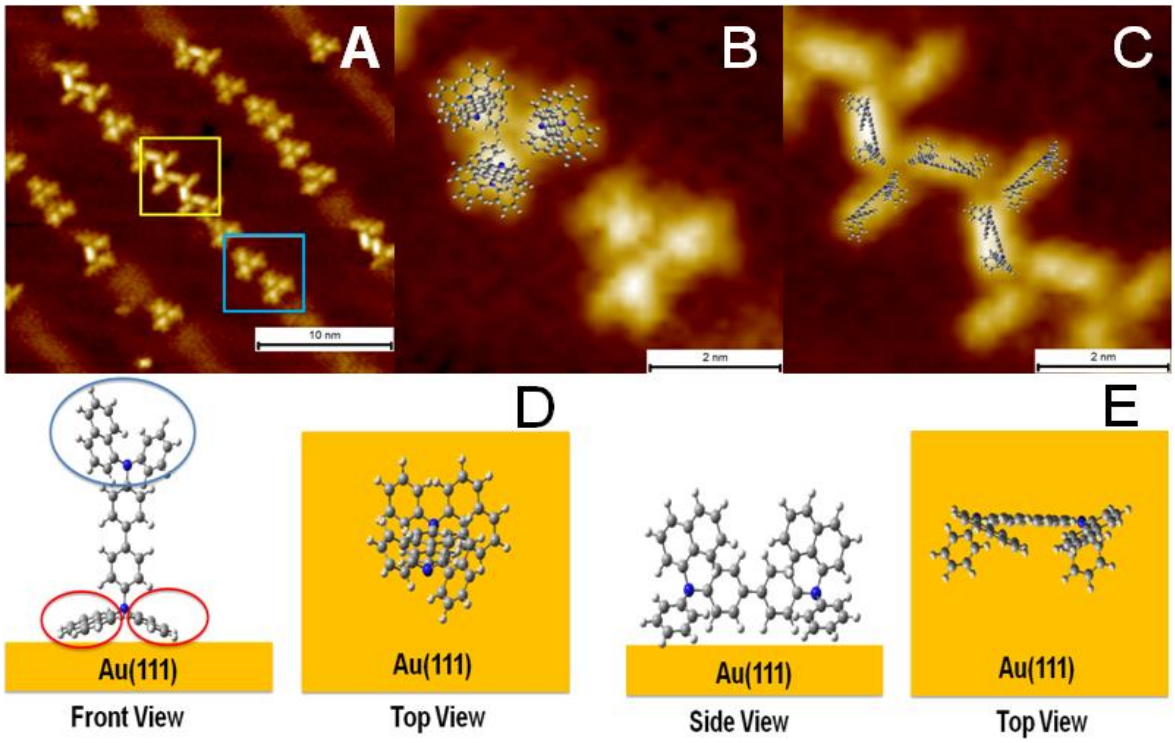


Figure 4.4: STM images of α-NPD stable clusters on Au(111) substrate and molecule conformations at two separate areas. (A) 29.1nm ×29.1nm, acquired at 1pA with -1.5V bias at 131K; (B) 6nm ×6nm zoom-in area (blue square in A) and molecule conformation; (C) 6nm ×6nm zoom-in area (yellow square in A) and molecule conformation; (D) and (E) schemes of front view and top view of α-NPD molecule on Au(111) in these two patterns.

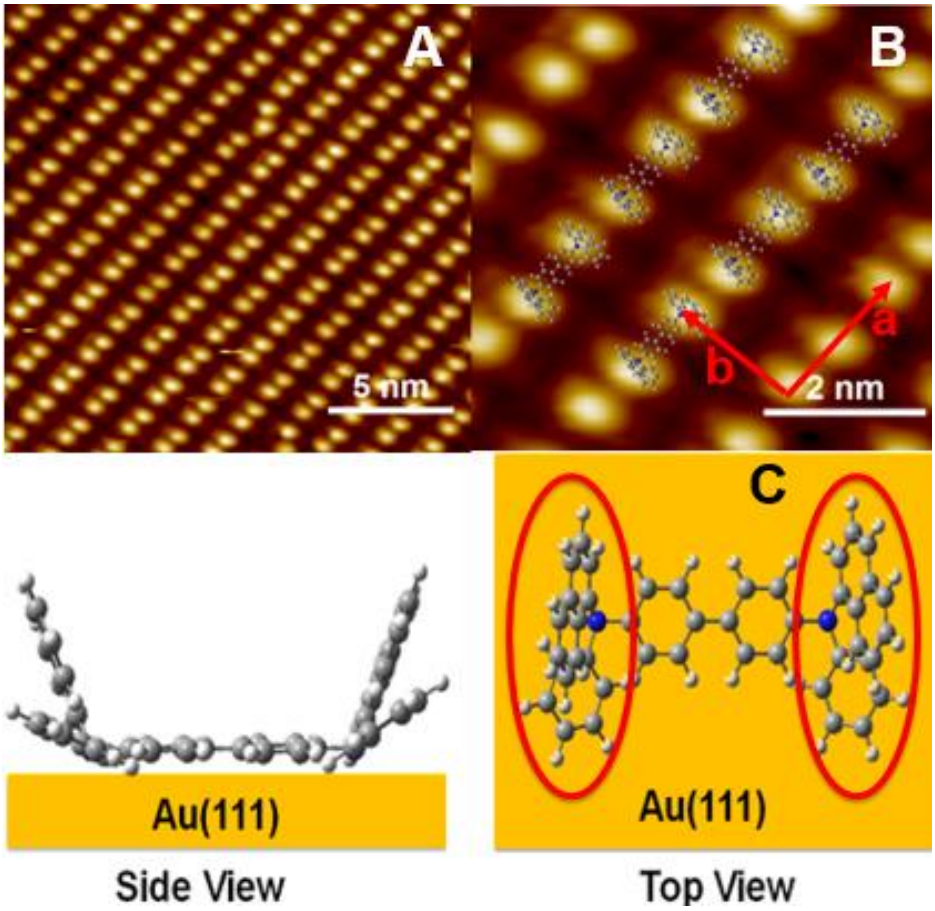


Figure 4.5: STM images of first layer narrow-single-row pattern of α-NPD on Au(111) substrate and molecule orientation. (A) 27.9nm×27.9nm, acquired at 10pA with 1V bias at 131K; (B) zoom-in area from (A) of 5.7nm×5.7nm, fitted with proposed molecule orientation; (C) scheme of side view and top view of α-NPD molecule on Au(111) in this narrow-single-row pattern.

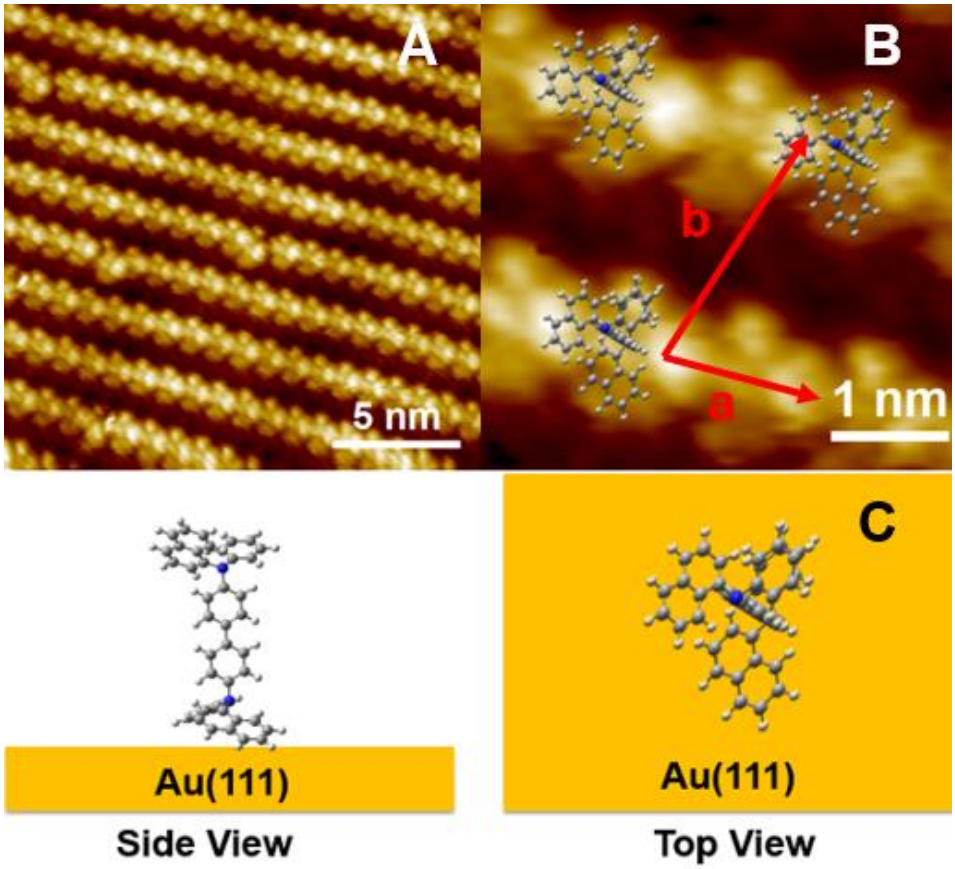


Figure 4.6: STM images of first layer broad-single-row pattern of α-NPD on Au(111) substrate and molecule orientation. (A) 18.6nm×18.6nm, acquired at 5pA with -1V bias at 131K; (B) zoom-in area from (A) of 4nm×4nm, fitted with proposed molecule orientation; (C) scheme of side view and top view of α-NPD molecule on Au(111) in this broad-single-row pattern.

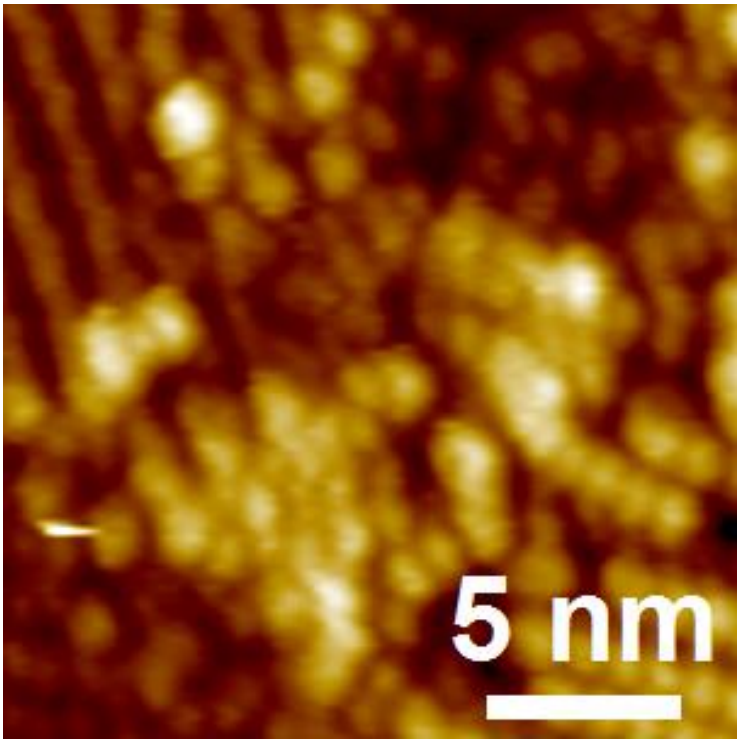


Figure 4.7 STM images of first layer disordered pattern of α-NPD on Au(111) substrate. Size=19nm×19nm, acquired at 1pA with -1V bias at 131K.

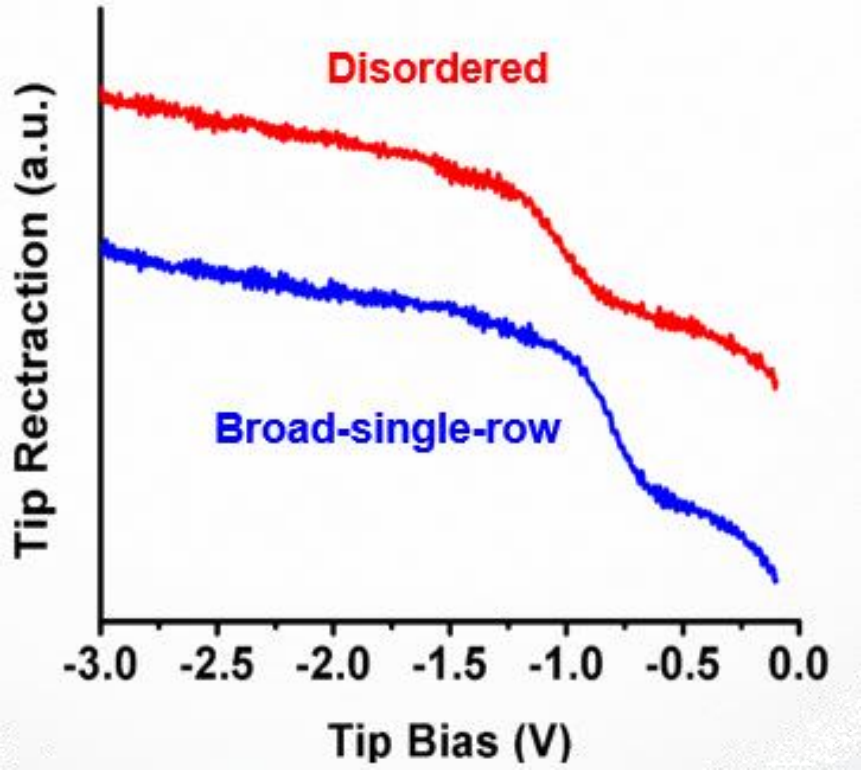


Figure 4.8 Representative constant-current z(v) spectra for broad-single-row and disordered pattern.

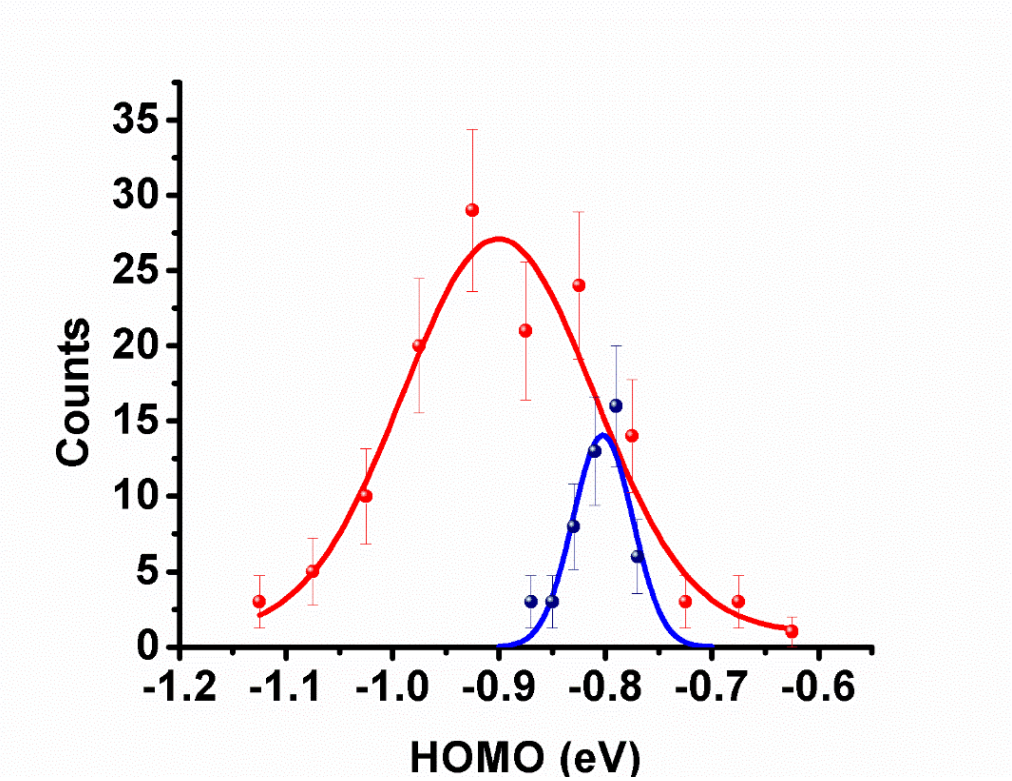


Figure 4.9 Histograms of HOMO positions of the α-NPD molecule and their Gaussian Distribution fit for both broad-single-row pattern (blue curve) and disordered pattern (red curve).

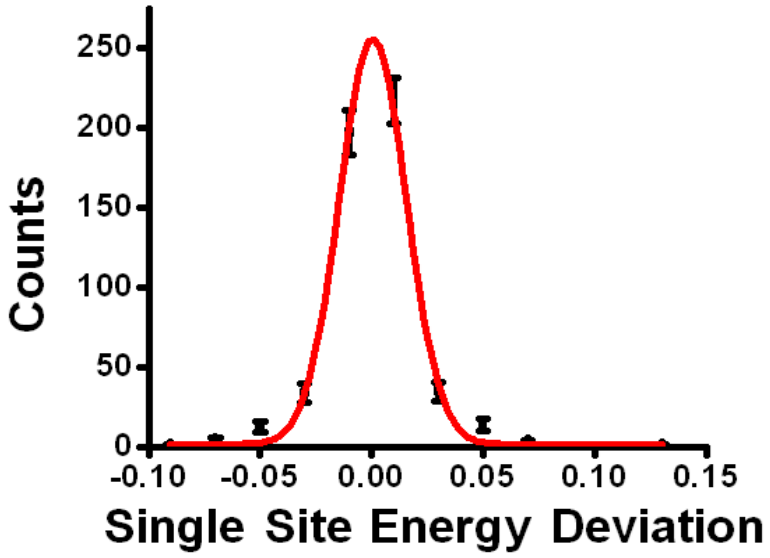


Figure 4.10 Gaussian distribution fit of single site energy deviations from their mean values.

REFERENCES

(1)Chasse, T.; Wu, C. I.; Hill, I. G.; Kahn, A. *J. Appl. Phys.* **1999**, *85*, 6589.

(2)Kijima, Y.; Asai, N.; Tamura, S.-i. *Japanese journal of applied physics* **1999**, *38*, 5274.

(3)Lee, S. S.; Song, T. J.; Cho, S. M. *Materials Science and Engineering: B* **2002**, *95*, 24.

(4)Deshpande, R. S.; Bulovic, V.; Forrest, S. R. *Appl. Phys. Lett.* **1999**, *75*, 888.

(5)Dinelli, F.; Murgia, M.; Levy, P.; Cavallini, M.; Biscarini, F.; de Leeuw, D. M. *Phys. Rev. Lett.* **2004**, *92*, 116802.

(6)Chu, T.-Y.; Song, O.-K. *J. Appl. Phys.* **2008**, *104*, 023711.

(7)Borsenberger, P. M.; Magin, E. H.; Shi, J. *Physica B* **1996**, *217*, 212.

(8)Mensfoort, S. L. M. v.; Shabro, V.; Vries, R. J. d.; Janssen, R. A. J.; Coehoorn, R. *J. Appl. Phys.* **2010**, *107*, 113710.

(9)Gartstein, Y. N.; Conwell, E. M. *Chem. Phys. Lett.* **1995**, *245*, 351.

(10)Barth, J. V.; Brune, H.; Ertl, G.; Behm, R. J. *Phys.Rev. B* **1990**, *42*, 9307.

(11)Narasimhan, S.; Vanderbilt, D. *Phys. Rev. Lett.* **1992**, *69*, 1564.

(12)Dougherty, D. B.; Jin, W.; Cullen, W. G.; Reutt-Robey, J. E.; Robey, S. W. *The Journal of Physical Chemistry C* **2008**, *112*, 20334.

(13)Xu, B.; Tao, C.; Cullen, W. G.; Reutt-Robey, J. E.; Williams, E. D. *Nano Lett.* **2005**, *5*, 2207.

(14)Eremtchenko, M.; Temirov, R.; Bauer, D.; Schaefer, J. A.; Tautz, F. S. *Phys.Rev. B* **2005**, *72*, 115430.

(15)Koller, G.; Surnev, S.; Netzer, F. P.; Ramsey, M. G. *Surf. Sci.* **2002**, *504*, 11.

(16)Huston, S. M.; Wang, J.; Loth, M. A.; Anthony, J. E.; Conrad, B. R.; Dougherty, D. B. *The Journal of Physical Chemistry C* **2012**, *116*, 21465.

(17)Selzer, Y.; Allara, D. L. *Annu. Rev. Phys. Chem.* **2006**, *57*, 593.

(18)Pronschinske, A.; Mardit, D. J.; Dougherty, D. B. *Phys.Rev. B* **2011**, *84*, 205427.

(19)Fleissner, A.; Schmid, H.; Melzer, C.; Von Seggern, H. *Appl. Phys. Lett.* **2007**, *91*, 242103.

(20)Tong, K. L.; Tsang, S. W.; Tsung, K. K.; Tse, S. C.; So, S. K. *J. Appl. Phys.* **2007**, *102*, 093705.

(21)Chu, T.-Y.; Song, O.-K. *J. Appl. Phys.* **2008**, *104*, 023711.

(22)Yuen, K. K. *Biometrika* **1974**, *61*, 165.

(23)Blüm, M.-C.; Pivetta, M.; Patthey, F.; Schneider, W.-D. *Phys.Rev. B* **2006**, *73*, 195409.

(24)Käfer, D.; Ruppel, L.; Witte, G.; Wöll, C. *Phys. Rev. Lett.* **2005**, *95*, 166602.

# Chapter 5

# Extrinsic Origins of Electronic Disorder in 2D Organic Crystals

## 5.1 Background and Motivation

Organic semiconductors are among the most promising electronic materials under development for new applications in low cost photovoltaics, low power lighting, and advanced display technologies[1-3]. At present, a significant basic scientific challenge associated with these materials is to find the new ways to improve film structure and morphology for specific applications. The classic example is the ongoing effort to optimally match donor-acceptor domain sizes to exciton diffusion lengths for organic photovoltaics[4,5]. In the case of organic field effect transistors (OFET's), large scale crystallinity and molecular packing are crucial and single crystal OFET's have indeed revealed very high carrier mobilities[6] that set the scale for performance limits in the entire material class[7].

An interesting recent adaptation of the OFET can be found in the consideration of two-dimensional field effect transistors including self-assembled monolayer FET's[8]. In these devices, charge transport occurs in a single (quasi) two-dimensional (2D) layer of molecules in contact with a gate dielectric. Self-assembly is used to establish optimal molecular π-π

stacking for efficient charge transport throughout the 2D layer. This packing results in very good ("bulk-like") carrier mobilities and patterned films can be used to implement complex logic functionality[9]. Moreover, coverage-dependent studies make it clear that if a complete 2D layer can be created between source and drain electrodes, then efficient transport through this layer can be achieved for large channel lengths[10].

Brondijk et al. have very recently reported a unique impact of disordered 2D transport on the temperature dependence of current-voltage characteristics of FET's made from single layer films of α-sexithiophene (α-6T) and related SAMFET's[11]. The power law scaling of current as a function of voltage changes more slowly with temperature in 2D FET's compared to thicker 3D FET's. This comparison provides a compelling experimental rationale for the identification of 2D organic crystals as unique in comparison to traditional organic thin films. By focusing on the 2D self-assembly, it may be possible to combine the advantages of high crystallinity associated with single crystal OFET's with advantageous thin film processing that allows device pattering, versatile substrate choice, and better mechanical properties.

The observation of Brondijk et al. about unique scaling in 2D organic crystals is explained by consideration of transport in the tails of the electronic density of states associated with disorder in the film[12]. More generally, electronic disorder in organic semiconductor materials is ubiquitous due to weak intermolecular interactions and significantly impacts the charge transport characteristics in many organic thin films. To accurately predict or explain current-voltage characteristics for organic thin film electroluminescent diodes[13] or organic field effect transistors[14], it is necessary to incorporate

some phenomenological model of electronic disorder such as transport in the tail of a Gaussian or exponential density of states[15].

The microscopic molecular origins of electronic disorder are poorly characterized. It is clear from a general view that structural disorder in organic thin films can have electronic impacts by inducing variable local intermolecular polarizations around a charge carrier[16]. In addition, impurities have long been implicated as "charge traps" in organic semiconductor films[17]. However, particularly in the case of SAMFET's which are designed to be well-ordered over micrometer length scales it is desirable to identify the specific microscopic mechanisms that control the disordered density of electronic states. Recent molecular dynamics simulations of SAMFET's illustrate the potential impact of conformational disorder on transport[18] but this possibility may not be relevant to rigid layers assembled from planar aromatics such as α-6T or functionalized acenes.

In this chapter, we report scanning tunneling microscopy and spectroscopy observations that demonstrate that disorder in 2D crystals of α-6T is dominated by extrinsic effects, even in the presence of structural disorder. By considering single layer islands of α-6T grown on top of $C_{60}$ monolayers on Au(111), we establish an system analogous to the 2D FET investigated by Brondijk et al.. We find that the highest occupied molecular orbital energy of α-6T is unusually sensitive to random changes in STM probe tip. In this experiment, the STM tip serves as a model of extrinsic disorder analogous to charge traps in a gate dielectric in a 2D FET. The implication of our observations is that electronic disorder may be minimized in 2D FET's by employing high quality gate dielectric with a low density of charged impurities.

## 5.2 Experimental Methods

Experiments were carried out in a multichamber UHV system with a sample preparation and STM chamber (base pressure ~ $5 \times 10^{-11}$ torr ) connected by a gate valve to organic deposition chamber (base pressure ~ $1 \times 10^{-8}$ torr) housing fullerene-$C_{60}$ and α-6T evaporators and two independent quartz crystal microbalances for monitoring molecular deposition flux. The raw α-6T material (Sigma Aldrich) was loaded as-received into a quartz crucible heated with a helical Ta wire. It was outgassed extensively to remove low vapor pressure impurities and deposition flux was monitored with a quartz crystal microbalance. Deposition of high purity α-6T was confirmed by creation of a complete, flat-lying monolayer of this molecule on Au(111) as reported[19].

Substrates were Au(111)-oriented films on mica (SPI supplies) that were sputtered in the STM chamber with 1 keV Ar+ ions and then annealed at ~700 K. Multilayer films of $C_{60}$ (Sigma-Aldrich) were deposited in the organic deposition chamber onto the cleaned Au film substrate held at room temperature. These films were then annealed at ~ 600 K to desorb the multilayers and leave behind a perfect $C_{60}$ monolayer. After this 1 ML $C_{60}$/Au(111) substrate was created, α-6T was deposited with the substrate held at room temperature.

Scanning tunneling microscopy measurements were carried out using home-etched tungsten tips with the sample cooled to 130 K using a liquid nitrogen bath cryostat. Scanning tunneling spectroscopy was carried out in constant-current distance voltage mode at current set point of typically 1 pA. This low current value is employed to avoid perturbation of the molecular film during spectroscopic measurements. Spectra are reported as raw relative tip height versus voltage traces or their logarithmic derivative [20] as shown in Chapter 2.

## 5.3 Results and Discussion

Figure 5.1 shows the STM image of $C_{60}$ monolayer on Au(111)/Mica. Seen from large area image (93nm ×93nm) Figure 5.1(A), the $C_{60}$ overlayer follows the Au terraces, no underlying Au surface and C60 second layer are observed, indicating a $C_{60}$ monolayer is achieved. Fig5.1(B) is an image of zoom-in area (41.8nm ×41.8nm), and $C_{60}$ pattern in molecular resolution is resolved. The $C_{60}$ on Au(111) monolayer follows the close-packed $38 \times 38$ or $(2\sqrt{3} \times 2\sqrt{3})R30°$ unit cell, as reported in Altman's papers[21,22]. However, the type of our $C_{60}$ film unit cell is still unknown, since it will need the information of Au(111) crystal orientation. In the image each spot is a $C_{60}$ molecule with different brightness. This contrast comes from the difference in bonding between the $C_{60}$ molecule and the Au substrate due to $C_{60}$ molecules bound in different rotational orientation on the surface[23].

The result of subsequent deposition of α-6T onto this substrate is shown in Figure 5.2(A) in the form irregularly-shaped islands of typical size 40000 $nm^2$. These are very similar to the pentacene islands reported on top of a $C_{60}$ monolayer[24] and most importantly are reminiscent of the α-6T islands in 2D FET's on $SiO_2$ dielectrics (see supplemental information in Ref 11). In a smaller STM image Figure 5.2(B), a typical line profile is plotted across the island of α-6T and $C_{60}$ monolayer underneath, and the result is shown in Figure 5.2(C). The island height is about 2.2 nm, which is similar to the length of α-6T along its long axis (=2.4 nm)[25]. Although apparent height measurements in STM also include convolution of electronic structure effects, the observations in Figure 5.2 are suggestive of a nearly upright orientation of α-6T molecules on the $C_{60}$ monolayer, similar to pentacene on $C_{60}$[24] and on benzenethiol SAM[26]. This orientation is consistent with expectations based on

relatively weak interaction between the close-packed $C_{60}$ layer and the α-6T molecules which results in an energetic preference to maximize interaction between α-6T molecules by forming a packed, upright layer.

To understand the α-6T structure on $C_{60}$ monolayer, zoom-in STM images are essential. Figure 5.3 shows the typical STM images of $C_{60}$ monolayer on Au/Mica and α-6T on $C_{60}$ on Au/Mica in molecular resolution respectively. Unlike the compact pattern of $C_{60}$ (shown in Figure 5.3(A)), the α-6T on $C_{60}$ shows a double-row pattern, as indicated by blue lines in Figure 5.3(B). The structure within the double rows is reminiscent of the molecular arrangement in the a-b plane of the α-6T bulk crystal structure and the molecules make a locally oblique net with sides of length.

To quantitatively analyze the structure of α-6T on $C_{60}$ monolayer, two dimensional Fast Fourier Transform (2D-FFT) method is utilized. Figure 5.4(A) show the typical α-6T on $C_{60}$ monolayer STM topography. The parameters to demonstrate the crystal structure are defined in Figure 5.4(B). By averaging FFT images of six different positions, the parameters are: distance between two parallel double rows c=1.60±0.04nm, distance between two closest α-6T molecules b=0.62±0.04nm, distance between two α-6T molecules along the row direction a=0.92±0.02nm. It is interesting to see b=0.62nm is similar to the lattice distance 0.6029nm reported in α-6T bulk crystals[27], and it indicates the α-6T bulk crystal structure still kept to some extent during aligning on the $C_{60}$ monolayer. But a=0.92nm is close to the $C_{60}$ bulk crystal lattice distance=1 nm[22], this reflects the templating effect of the $C_{60}$ substrate, adjusting the α-6T to follow the underlying $C_{60}$ pattern. Conclusively this ordered

structure can be rationalized in a straightforward manner as a bulk-like crystal packing of α-6T modulated to have by the influence of the hexagonal $C_{60}$ monolayer substrate.

One more apparent feature of α-6T on $C_{60}$ monolayer on Au/Mica is the bright and dark spots disorderly across the surface. The height difference between bright and dark spots is $0.08 \pm 0.02$ nm by averaging 120 profiles over different molecules. These apparent height variations are not present on the starting $C_{60}$ monolayer substrate. We attribute the random apparent heights of α-6T molecules on $C_{60}$/Au(111) to random molecular sliding defects where the planar, rod like molecules are slightly slipped along their long axis with respect to one another, as demonstrated in Figure 5.5. These sliding defects have been observed with similar apparent height variations for upright pentacene layer on $C_{60}$/Ag(111) [24] and for upright pentacene on thiolate self-assembled monolayers[26]. In the latter case, computational studies suggested that the defects could lead to molecular orbital energy modifications of up to 0.1 eV, a sizeable possible contribution to electronic disorder.

The observation of molecular sliding defects shown in Figure 5.3 and 5.4 is the first example other than for pentacene films. Sliding defects in our α-6T layers are distinct from the known examples in pentacene in that α-6T molecules which are slipped along their long axis do not tend to aggregate into the domains seen for pentacene. This suggests the possibility that such defects are common in 2D organic layers and their predicted electronic impact in pentacene suggests them as microscopic sources of disorder in 2D α-6T films. We investigated this possibility by carrying out local scanning tunneling spectroscopy of the α-6T layers on $C_{60}$/Au(111). In this case we can measure the energy of the highest occupied molecular orbital for molecules with different apparent heights.

In Figure 5.6, we show representative constant current spectra measured locally on molecules spanning the full 0.1 nm range of apparent height variations. Remarkably, there is no observable correlation in energy of the HOMO with local apparent height. In addition to the spectra in Figure 5.6, we have considered total 82 different molecules in other images and did not find any significant dependence of HOMO energy on apparent height. We also found no correlations between local HOMO energy and the average apparent height of adjacent near neighbor molecules in the α-6T film. This suggests that the sliding defect in α-6T have a negligible electronic effect.

Given this insensitivity to intrinsic structural defects, what is the origin of electronic disorder in such a 2D organic crystal? To answer this question, we report on the observation of large variability in measured HOMO energy position in response to random variations in STM tip condition. In a typical STM experiment, the details of tip condition are unknown and often change in response to uncontrolled tip-sample interactions, atomic-scale thermal or field-induced rearrangements of tip atoms, or adsorption of residual gas molecules. This can have the effect of changing tip apex, shape, and/or tip work function. In these cases, the net result can be understood as the creation of variable electrostatic field distributions around the probe tip.

Within a given STM image such as Figure 5.6(A) where tip condition is evidently stable based on stable imaging conditions, we observed a very narrow distribution of HOMO energies with variations only on the order of 0.05 eV. However, on different days (after in-situ tip processing steps) larger variations of up to 0.25 eV were observed. In Figure 5.7 the z(V) spectra taken from 7 different days on the same sample is shown. The spectroscopy is

measured under constant-current mode (I=1pA) to achieve HOMO of α-6T on $C_{60}$. Each spectrum contains an average of at least 29 different molecules. The peak position is seen to vary from 0.7 eV to 0.45 eV below the Fermi level for these different conditions. Comparing this result with the HOMO of ~ -1eV by UPS reported by Mäkinen [28] from α-6T monolayer on Au substrate, where α-6T molecules tend to lie down on Au substrate, the HOMO state of our standing-up molecules moves toward the Fermi level. This is consistent with the result of Duhm *et al.* [29]. Due to the interface dipole of α-6T lying on Au substrate generating a higher electrostatic potential region above the α-6T π-system, electron from HOMO will be difficult to push into this region to make HOMO level of lying-down molecules move farther away from Fermi level than standing-up α-6T molecules. This observation further approved our argue that α-6T molecules stand up on $C_{60}$ monolayer.

After the intuitive illustration of HOMO shift due to random tip status as shown in Figure 5.7, a statistical analysis is carried out in Figure 5.8. Total number of 412 HOMO spectra measured under all kinds of tip conditions (stable and unstable) are averaged and deviations from the mean value are fitted to Gaussian distribution as shown of the black curve in Figure 5.8. On the other hand, total number of 275 HOMO spectra are measured under stable tip conditions only (on one single image and no perturbance due to tip found on image), and deviations from their separate mean values are fitted to a Gaussian distribution as shown of the red curve in Figure 5.8. The distribution probability is normalized for both situations for clarity. The experimental uncertainty acquired from stable tip is $\sigma_{exp}=0.032\pm0.003$ eV, while the width of distribution from all tip conditions is

$\sigma_{all}$=0.078±0.013 eV, by assuming all the distributions follow Gaussian distribution, disorder induced by tip is

$$\sigma_{tip} = \sqrt{\sigma_{all}^{\ 2} - \sigma_{\exp}^{\ 2}} = 0.071eV \quad . \qquad (5.1)$$

This disorder induced by tip is significant comparing with the pure experimental uncertainty.

We interpret the large variations shown in Figure 5.8 as originating from the impact of variations in the large electrostatic field of the STM tip (e.g. ~ 0.5 V/nm) on the energy of the HOMO orbital. This essentially represents a "Stark shift" of the molecular orbital. Such field effects are usually strongly screened in STM studies of monolayer films by proximity of a metallic substrate. However, in the case of α-6T on $C_{60}$/Au(111) the spatial decoupling of the α-6T layer from the polarizable metal substrate should significantly diminish screening efficiency.

The STM tip in our experiment plays the role essentially of a movable local top gate. This analogy is important because it leads to the conclusion that, in a 2D crystals of α-6T such as those considered here, the dominant source of electronic disorder will be *extrinsic* to the organic film. This notion was posited by Brondijk et al. on intuitive geometric grounds[11] and our observations provide direct experimental evidence. The implication is that if 2D FET's can be created on an electrostatically perfect gate dielectric, electronic disorder may be negligible and charge transport may approach the limits expected based on single crystal FET studies.

It is interesting to draw a parallel between the dominant extrinsic disorder in 2D α-6T film and the impact of charged impurity scattering in graphene. The carrier mobility in graphene is limited by scattering from charged impurities[30], many of which arise from

defects in the gate dielectric (typically $SiO_2$)[31]. By either suspending graphene[32] or using extremely high quality hexagonal boron nitride (h-BN) gate dielectrics[33] extraordinarily high charge carrier mobilities may be obtained. On this basis we suggest that an interesting transport experiment is to grow a 2D organic FET on an h-BN gate to search for evidence of disorder-free charge transport. In the context of this comparison with graphene, it is interesting to consider whether 2D organic crystals may be included within the growing panoply of 2D electronic materials (e.g. MoS2, Bi2Se3, etc.) that have emerged beginning with recent progress in graphene[34,35]. Organic semiconductors could bring to this layered materials paradigm useful optical absorption properties as well as band gaps suitable for logic functions.

## 5.4 Summary and Conclusions

In summary, we report STM and STS observations of 2D layers of α-6T grown on top of $C_{60}$ in an upright orientation that is likely similar to 2D FET films. Molecular packing reflects the tendency for bulk-like intermolecular interactions modulated by the $C_{60}$ substrate. We identify molecular sliding defects from random apparent height variations but show that these defects have a negligible electronic effect on the HOMO. By contrast random variations in probe tip results in very significant shifts of the HOMO energy. This provides experimental evidence that a dominant source of disorder in 2D organic crystals can be extrinsic to the molecular film. In such situations, careful attention to use of high quality defect-free gate dielectrics could lead to charge carrier mobilities in 2D FET's that approach established single crystal limits. Elimination of extrinsic sources of electronic disorder

would integrate 2D organic crystals into the growing class of high performance 2D materials such as graphene, h-BN, and $MoS_2$.

FIGURES

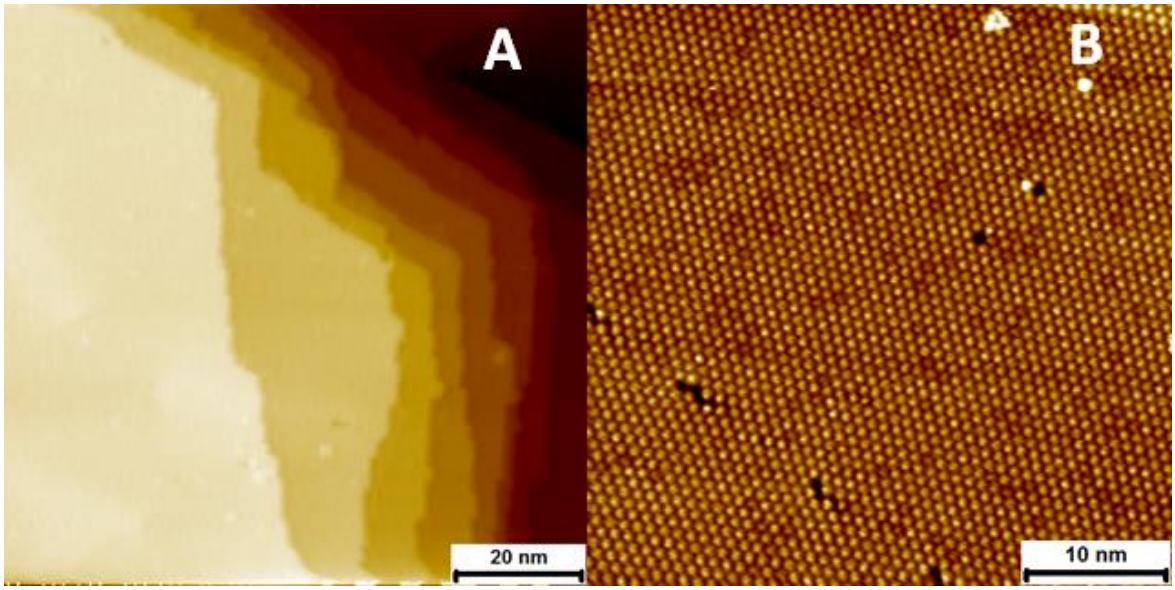


Figure 5.1 STM images of $C_{60}$ monolayer on Au(111)/Mica. (A) 93nm ×93nm, acquired at 10pA with -1V bias at 131K; (B) 41.8nm ×41.8nm, acquired at 10pA with -1V bias at 131K.

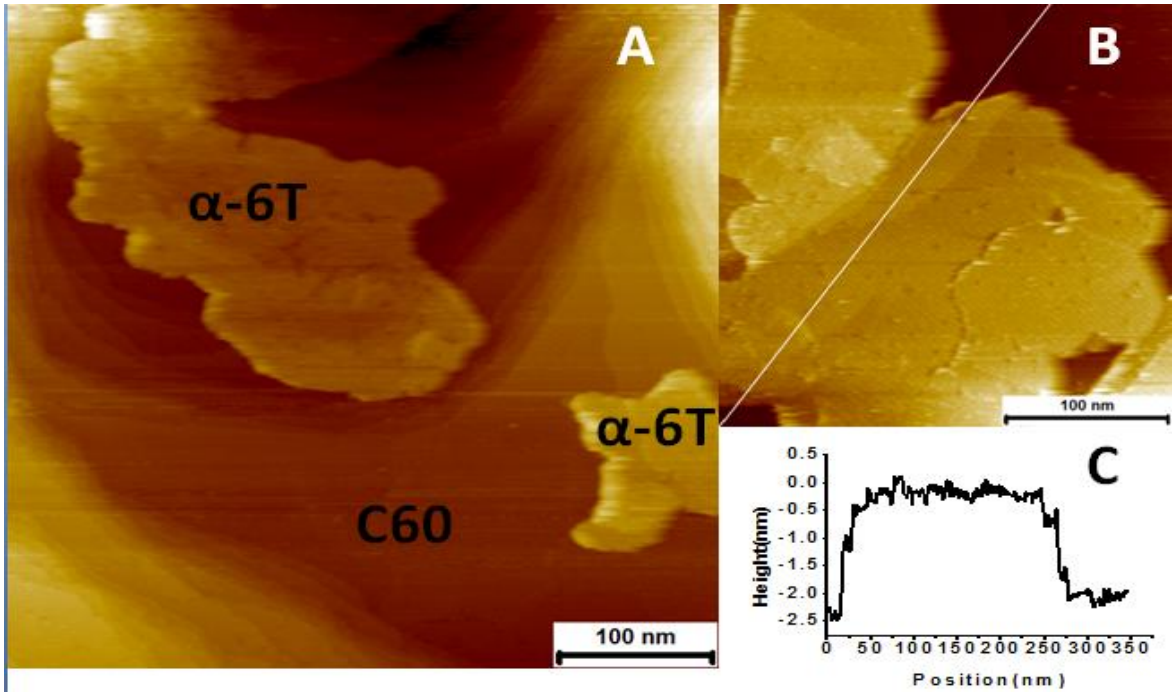


Figure 5.2 STM images of α-6T on $C_{60}$ monolayer on Au/Mica. (A) 465nm ×465nm, acquired at 100pA with -0.8V bias at 131K; (B) 279nm ×279nm, acquired at 100pA with -0.8V bias at 131K;(C)profile of the white line shown in (B).

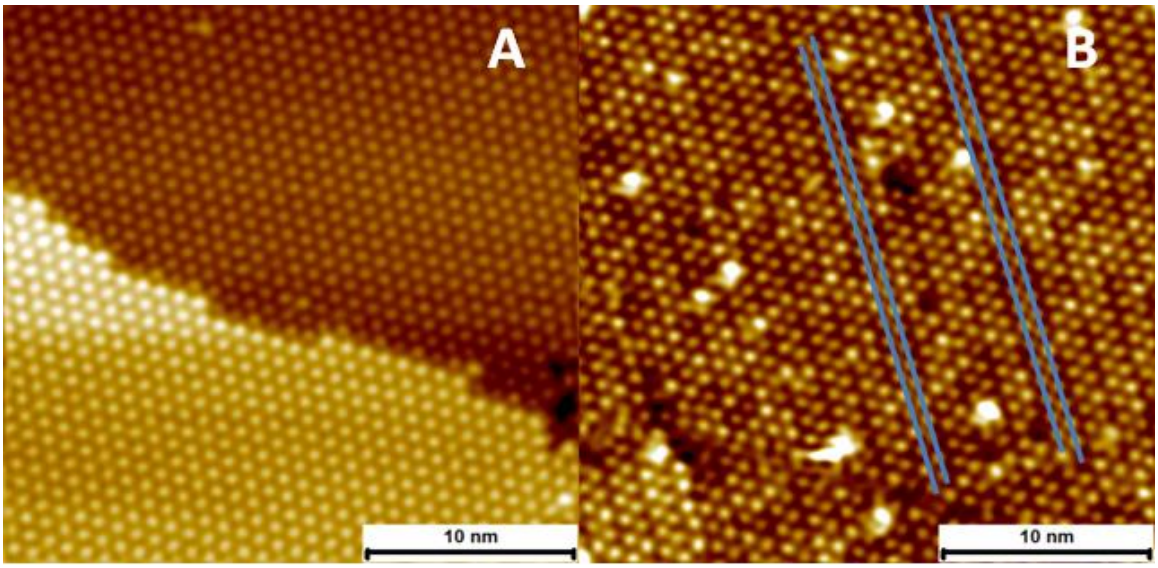


Figure 5.3 STM image comparison of (A) $C_{60}$ monolayer on Au/Mica and (B) α-6T on $C_{60}$ monolayer on Au/Mica. Both are acquired at same condition: 27.9nm×27.9nm,-0.8V bias, 1pA, 131K, using the same tip. Blue lines in (B) highlight the α-6T double row pattern.

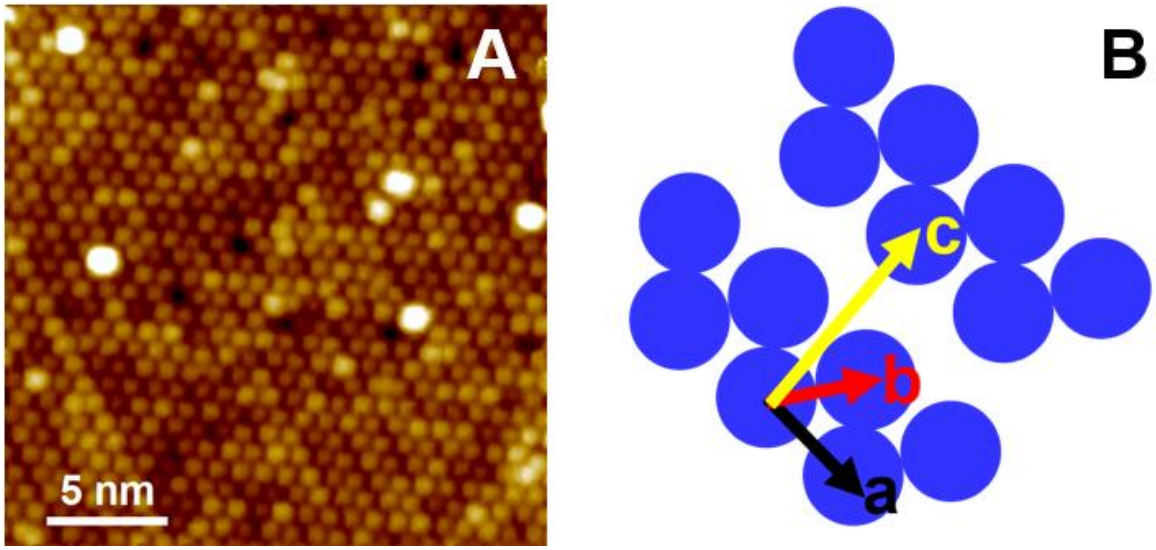


Figure 5.4 Structure determination of α-6T on $C_{60}$ using FFT method. (A) Typical STM image of α-6T on $C_{60}$ monolayer on Au/Mica, (22.3nm×22.3nm,-0.8V bias, 1pA, 131K) and (B) Scheme of structure of α-6T on $C_{60}$.

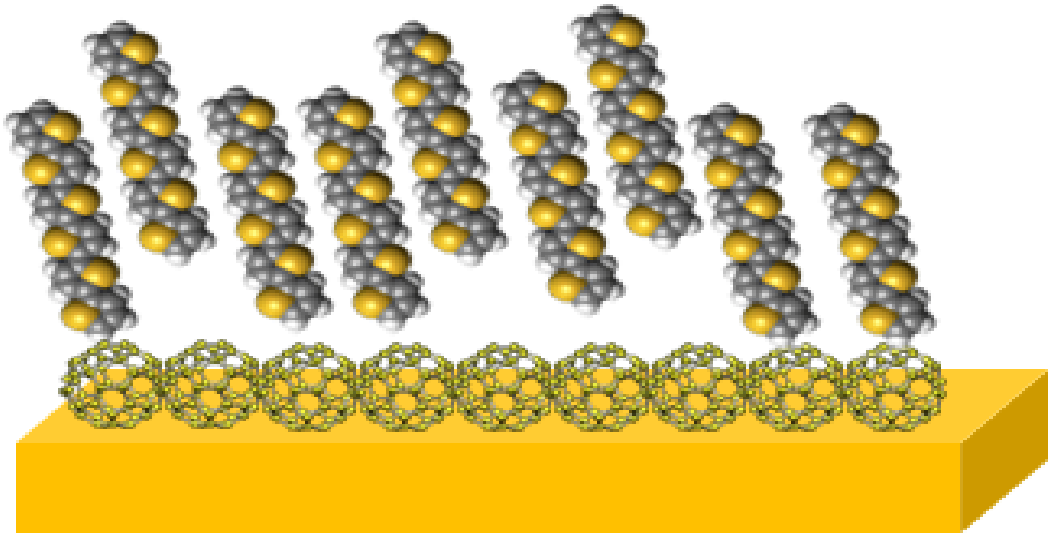

Figure 5.5 Scheme of crystal structure of α-6T on $C_{60}$ monolayer on Au/Mica.

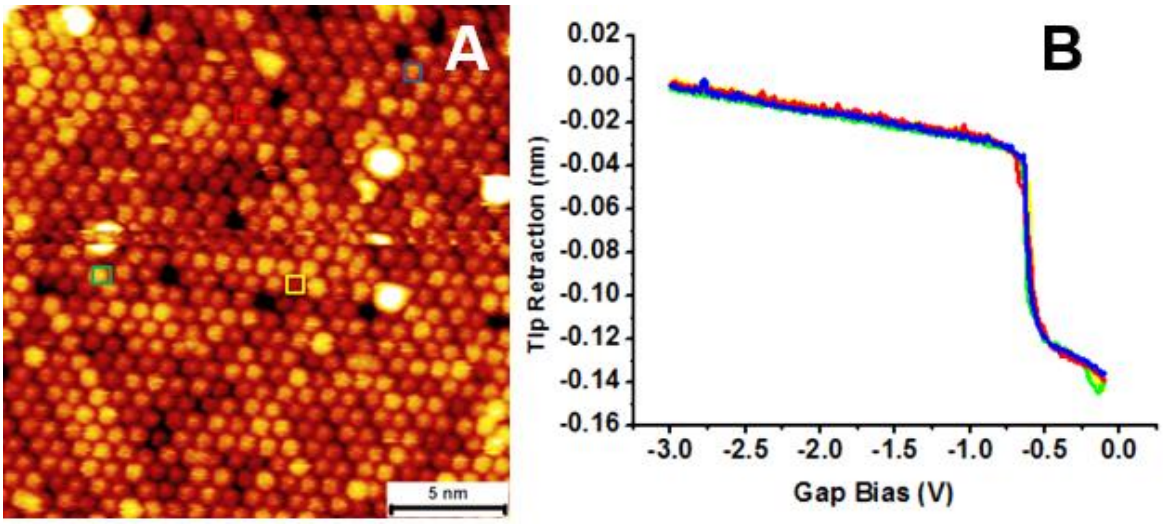


Figure 5.6 Representative z(V) spectra of HOMO side on four different α-6T molecules with various heights. (A) is the topography with squares indicating where spectra taken, (B) is the corresponding spectra.

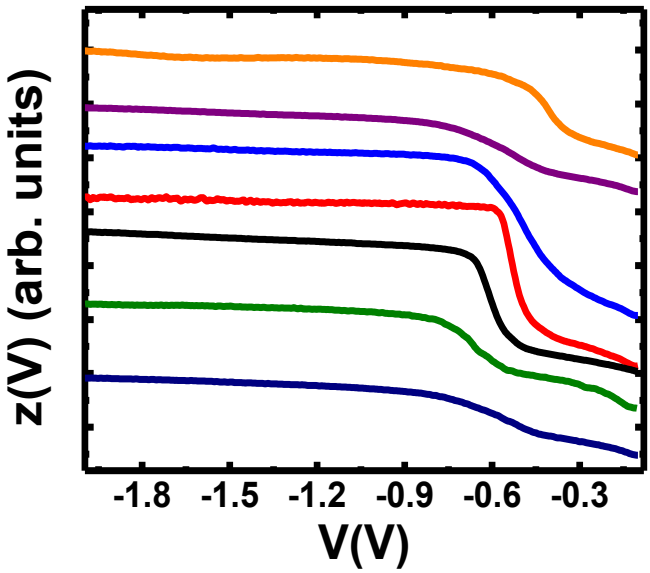


Figure 5.7 Scanning Tunneling Spectroscopy of α-6T on $C_{60}$ monolayer on Au/Mica at HOMO side under constant-current mode (I=1pA) during different days.

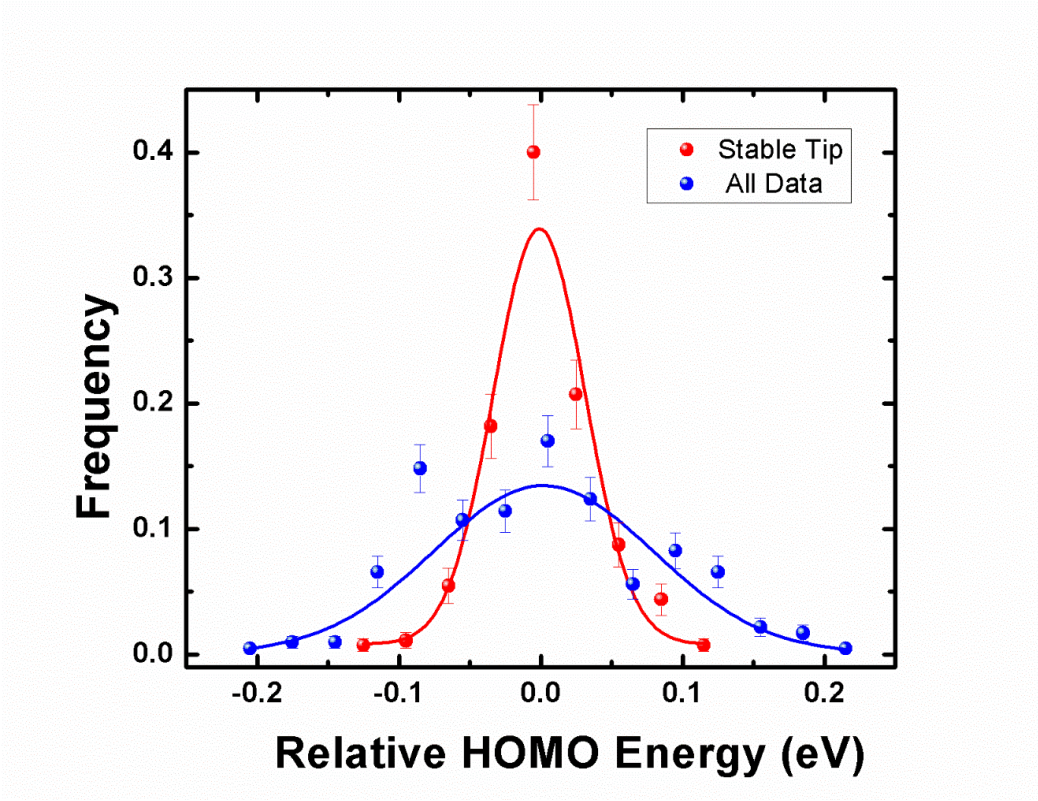


Figure 5.8 Comparison between statistical distribution of relative HOMO energies using a stable tip condition and the distribution for all data including different tip conditions. Data points are observed frequency of occurrence in 0.03 eV energy bins with Poisson error bars and solid lines are fits to a Gaussian distribution.

REFERENCES

(1)Gang, L.; Shrotriya, V.; Jinsong, H.; Yan, Y.; Moriarty, T.; Emery, K.; Yang, Y. *Nat. Mater.* **2005**, *4*, 864.

(2)Friend, R. H.; Gymer, R. W.; Holmes, A. B.; Burroughes, J. H.; Marks, R. N.; Taliani, C.; Bradley, D. D. C.; Dos Santos, D. A.; Bredas, J. L.; Lögdlund, M. *Nature* **1999**, *397*, 121.

(3)Forrest, S. R. *Nature* **2004**, *428*, 911.

(4)Yang, X.; Loos, J.; Veenstra, S. C.; Verhees, W. J. H.; Wienk, M. M.; Kroon, J. M.; Michels, M. A. J.; Janssen, R. A. J. *Nano Lett.* **2005**, *5*, 579.

(5)Lassiter, B. E.; Zimmerman, J. D.; Panda, A.; Xiao, X.; Forrest, S. R. *Appl. Phys. Lett.* **2012**, *101*.

(6)Kawasugi, Y.; Yamamoto, H. M.; Hosoda, M.; Tajima, N.; Fukunaga, T.; Tsukagoshi, K.; Kato, R. *Appl. Phys. Lett.* **2008**, *92*, 243508.

(7)Podzorov, V. *MRS Bull.* **2013**, *38*, 15.

(8)Tulevski, G. S.; Miao, Q.; Fukuto, M.; Abram, R.; Ocko, B.; Pindak, R.; Steigerwald, M. L.; Kagan, C. R.; Nuckolls, C. *J.Am.Chem.Soc.* **2004**, *126*, 15048.

(9)Love, J. C.; Estroff, L. A.; Kriebel, J. K.; Nuzzo, R. G.; Whitesides, G. M. *Chem. Rev.* **2005**, *105*, 1103.

(10)Mathijssen, S. G. J.; Smits, E. C. P.; van Hal, P. A.; Wondergem, H. J.; Ponomarenko, S. A.; Moser, A.; Resel, R.; Bobbert, P. A.; Kemerink, M.; Janssen, R. A. J. *Nat. Nanotechnol.* **2009**, *4*, 674.

(11)Brondijk, J. J.; Roelofs, W. S. C.; Mathijssen, S. G. J.; Shehu, A.; Cramer, T.; Biscarini, F.; Blom, P. W. M.; de Leeuw, D. M. *Phys. Rev. Lett.* **2012**, *109*, 056601.

(12)Vissenberg, M.; Matters, M. *Phys.Rev. B* **1998**, *57*, 12964.

(13)Tang, C. W.; VanSlyke, S. A. *Appl. Phys. Lett.* **1987**, *51*, 913.

(14)Ong, B. S.; Wu, Y.; Liu, P.; Gardner, S. *J.Am.Chem.Soc.* **2004**, *126*, 3378.

(15)Coehoorn, R.; Bobbert, P. A. *physica status solidi (a)* **2012**, *209*, 2354.

(16)Amy, F.; Chan, C.; Kahn, A. *Org. Electron.* **2005**, *6*, 85.

(17)Jurchescu, O. D.; Baas, J.; Palstra, T. *Appl. Phys. Lett.* **2004**, *84*, 3061.

(18)Jäger, C. M.; Schmaltz, T.; Novak, M.; Khassanov, A.; Vorobiev, A.; Hennemann, M.; Krause, A.; Dietrich, H.; Zahn, D.; Hirsch, A. *J.Am.Chem.Soc.* **2013**, *135*, 4893.

(19)Glowatzki, H.; Duhm, S.; Braun, K. F.; Rabe, J. P.; Koch, N. *Phys.Rev. B* **2007**, *76*, 125425.

(20)Pronschinske, A.; Mardit, D. J.; Dougherty, D. B. *Phys.Rev. B* **2011**, *84*, 205427.

(21)Altman, E. I.; Colton, R. J. *Phys.Rev. B* **1993**, *48*, 18244.

(22)Altman, E. I.; Colton, R. J. *Surf. Sci.* **1992**, *279*, 49.

(23)Altman, E. I.; Colton, R. J. *Surf. Sci.* **1993**, *295*, 13.

(24)Dougherty, D. B.; Jin, W.; Cullen, W. G.; Reutt-Robey, J. E.; Robey, S. W. *Appl. Phys. Lett.* **2009**, *94*, 023103.

(25)Lin, R.; Galili, M.; Quaade, U. J.; Brandbyge, M.; Bjornholm, T.; Esposti, A. D.; Biscarini, F.; Stokbro, K. *J.Chem.Phys.* **2002**, *117*, 321.

(26)Kang, J. H.; Filho, D. d. S.; Bredas, J.-L.; Zhu, X.-Y. *Appl. Phys. Lett.* **2005**, *86*, 152115.

(27)Horowitz, G.; Bachet, B.; Yassar, A.; Lang, P.; Demanze, F.; Fave, J.-L.; Garnier, F. *Chem. Mater*. **1995**, *7*, 1337.

(28)Makinen, A. J.; Long, J. P.; Watkins, N. J.; Kafafi, Z. H. *J. Phys. Chem. B* **2005**, *109*, 5790.

(29)Duhm, S.; Heimel, G.; Salzmann, I.; Glowatzki, H.; Johnson, R. L.; Vollmer, A.; Rabe, J. P.; Koch, N. *Nat Mater* **2008**, *7*, 326.

(30)Chen, J. H.; Jang, C.; Adam, S.; Fuhrer, M. S.; Williams, E. D.; Ishigami, M. *Nat. Phys.* **2008**, *4*, 377.

(31)Pacchioni, G.; Skuja, L.; Griscom, D. L. *Defects in SiO2 and related dielectrics: science and technology*; Kluwer Academic Pub, 2000; Vol. 2.

(32)Bolotin, K. I.; Sikes, K. J.; Jiang, Z.; Klima, M.; Fudenberg, G.; Hone, J.; Kim, P.; Stormer, H. L. *Solid State Commun.* **2008**, *146*, 351.

(33)Dean, C. R.; Young, A. F.; Meric, I.; Lee, C.; Wang, L.; Sorgenfrei, S.; Watanabe, K.; Taniguchi, T.; Kim, P.; Shepard, K. L. *Nat. Nanotechnol.* **2010**, *5*, 722.

(34)Shi, Y.; Zhou, W.; Lu, A.-Y.; Fang, W.; Lee, Y.-H.; Hsu, A. L.; Kim, S. M.; Kim, K. K.; Yang, H. Y.; Li, L.-J. *Nano Lett.* **2012**, *12*, 2784.

(35)Liu, Y.; Weinert, M.; Li, L. *Phys. Rev. Lett.* **2012**, *108*, 115501.

# APPENDIX

Appendix A

# Surface-Controlled Thermal Oligomerization of Terthiophene on Ag(111)

## Preface

This appendix is devoted to report the work of research on surface-controlled thermal oligomerization of terthiophene on Ag(111) in the format of paper. This work is put into appendix due to that it is not closely related to the topic of this dissertation but still quite valuable.

# Surface-Controlled Thermal Oligomerization of Terthiophene on Ag(111)

Jiuyang Wang, Jingying Wang, Daniel B. Dougherty*

Department of Physics, North Carolina State University, Raleigh, North Carolina 27695-8202, United States

**ABSTRACT:** In this paper we report a surface template approach to the synthesis of long thiophene oligomers. By scanning tunneling microscopy (STM) the oligomerization of terthiophene (3T) on Ag(111) surface after annealing at 600K was studied. A distribution of oligomers is formed due to a complex competition between desorption, decomposition, and oligomerization. For oligothiophene with lengths greater than 5 units, classic Flory-Schulz distribution is observed.

Conjugated organic semiconductors have attracted attention for electronic and optoelectronic applications[1] due to easy fabrication, mechanical flexibility and low cost.[2-4] An important example, the substituted polythiophene poly (3-hexylthiophene-2, 5-diyl) (P3HT) is a widely used soluble donor semiconductor in organic solar cell fabrication whose electronic and optical properties are dominated by the aromatic electron system in the linked thiophene rings. The alkyl side-chains in this material are required for good solubility but can also be a source of morphological disorder.[5] Moreover, polymerization reactions used to create this material can lead to highly variable conjugation lengths along the thiophene backbone. It is of

interest to obtain long thiophene oligomers with optical absorption properties well-matched to the solar spectrum that could be employed in vacuum-deposited tandem organic solar cells.

To synthesize an unsubstituted oligothiophene, the two most common procedures are the famous Suzuki[6] and Stille[7] reactions that can join thiophene rings. Each of these reactions involves a homogeneous Pd catalyst in solution to couple halogenated thiophene rings and the result is limited by product solubility that decrease rapidly with oligomer length. In this communication we show that a surface-catalyzed oligomerization can lead to the creation of very long oligothiophenes on surfaces.

Thiophene oligomerization has been reported to be promoted by adsorption on metal surface,[8] visible light exposure[9] and x-ray exposure.[10] It is particularly interesting to consider the possibility of surface-catalyzed oligomerization, which was previously-inferred from surface-enhanced Raman spectroscopy of terthiophene on a roughened Ag foil surface.[8] Such a procedure could be adapted to provide an easy route to unsubstituted long thiophenes of interest for optoelectronic applications.

Furthermore, there is a strong interest in developing methodology for surface-controlled chemical synthesis. This vision is intermediate between single-molecule chemistry[11,12] and large-scale catalysis and combines catalytic impacts of surface adsorption with surface templating effects on reaction products. Recent work has used Ullman-coupling schemes to create epitaxial polyethylene dioxide chains on Cu(110)[13] and macromolecular porphyrin structures on Au(111)[14] surfaces. In addition, this kind of nanochemical synthesis has been demonstrated as a route to bottom-up graphene nanoribbon synthesis by a multi-step process involving halogenated anthracene derivatives.[15] Here, we report scanning tunneling

microscopy (STM) observations of a new example in the spirit of these recent discoveries: annealing-induced oligomerization of terthiophene adsorbed on an Ag(111) surface. The substrate promotes the creation of very long thiophene chains (up to 18 units) and templates the chain direction epitaxially along substrate crystallographic directions.

The experiment was carried out in a combined STM and molecular deposition chamber described in a previous paper.[16] Terthiophene was obtained as low temperature outgassing product from as-received α-sexithiophene ("α-6T", Sigma-Aldrich) deposited onto a room temperature Ag(111) surface cleaned by standard sputtering/annealing cycles. STM imaging was carried out with the sample held at 131 K to promote stable imaging.

Figure 1(A) shows a STM image of a long-range ordered overlayer of terthiophene on Ag(111). As seen in figure 1(B), two different shapes of molecules are evident on the surface, bent and straight, each with a length of ~ 1.2 nm consistent with the known length of terthiophene.[17] These two shapes may indicate coexisting molecular orientations on the surface that arise either from surface-induced *trans*-to-*cis* isomerization reactions or from nearly equivalent adsorption energies for the same isomer as a function of bonding orientation. The bent shape suggests a flat-lying orientation where the predominant *trans* arrangement of thiophene sulphurs results in the bend.[18] The apparent dimerization strongly suggests assignment as a *trans* isomer. It was previously observed for terthiophene adsorbed on $MoS_2$ and can be attributed to electrostatic interactions between the central and end portions of adjacent *trans* molecules.[19]

The straight species with somewhat larger apparent height may be attributable to upright terthiophene adsorbates (such as suggested in Ref. 8 for surface-induced *cis* isomers)

with directed interactions between heteroatomic S atoms and the Ag(111) surface. The apparent height difference compared to the bent species includes contributions from the differences in molecular height as well as electronic structure differences. It is impossible to directly ascertain whether the straight molecules are *cis* using STM measurements. Even if they are all *trans*, the different bonding orientations would be expected to give rise to different highest occupied molecular orbitals and local work functions near the different molecules that would combine to determine the apparent height.

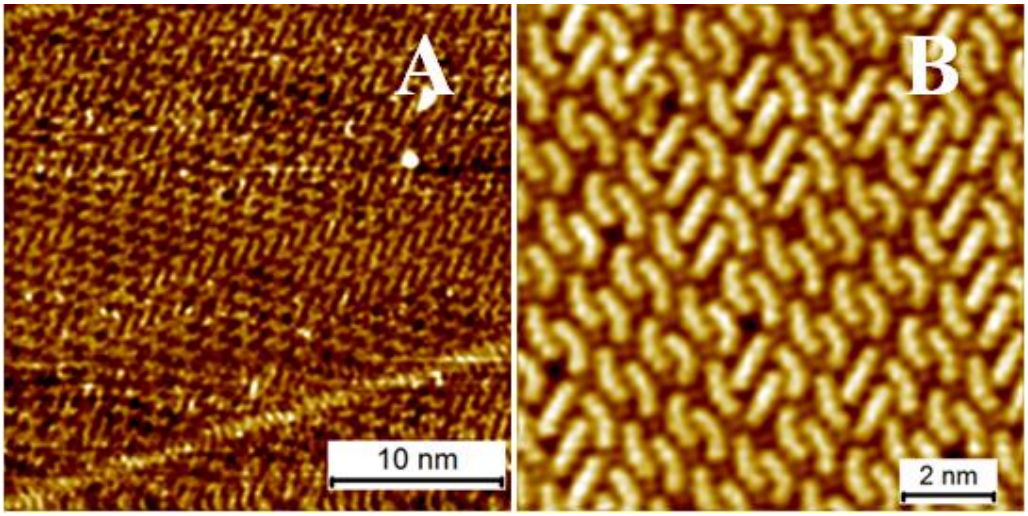


**Figure 1.** STM images of Terthiophene on Ag(111) as deposited at room temperature. (A)Large-scale $(29.8\ nm)^2$ STM image, acquired at 10 pA with -1 V bias at 131 K. (B)Small-scale $(11.2\ nm)^2$ STM image, acquired at 10 pA with -0.5 V bias at 131 K.

We annealed the sample shown in Figure 1 to ~600K. The result of this procedure is a complex combination of desorption, dissociation, and re-polymerization on the Ag(111) surface. Figure 2(A) is a large-scale STM image $(93\ nm)^2$ of the terthiophene film after annealing. Many molecules were desorbed from the Ag substrate at high temperature, leaving

behind only small islands near step edges. A high resolution STM image measured for one of these islands is shown in Figure 2(B). This immediately highlights the coexistence of different length molecular features on the surface. Instead of the uniform terthiophene (3T) film, after annealing we observe a series of thiophene oligomers, ranging from 2T to 18T.

The oligomers after annealing are assumed to be lying flat on the surface by observation of apparent size and comparison with other oligothiophene STM observations.[20,21] They are aligned mainly in three directions: one direction parallel to the step edge and other two directions that make 60 °angles with the first. This is consistent with templating of the product molecules by substrate crystallographic directions as reported for thiophenes on a number of metal surfaces. For example, α-6T shows a preference to align along close-packed [1-10] directions on Ag(100).[22] Both the correlations between reaction product locations and reactive step edges and the correlations with surface symmetry indicate the crucial role of the substrate in catalyzing the reaction and in templating the structure of the products. We hypothesize that the same reaction would proceed at lower temperature and with a more crystallographically homogeneous templating effect on the more open, less symmetric Ag(110) surface.

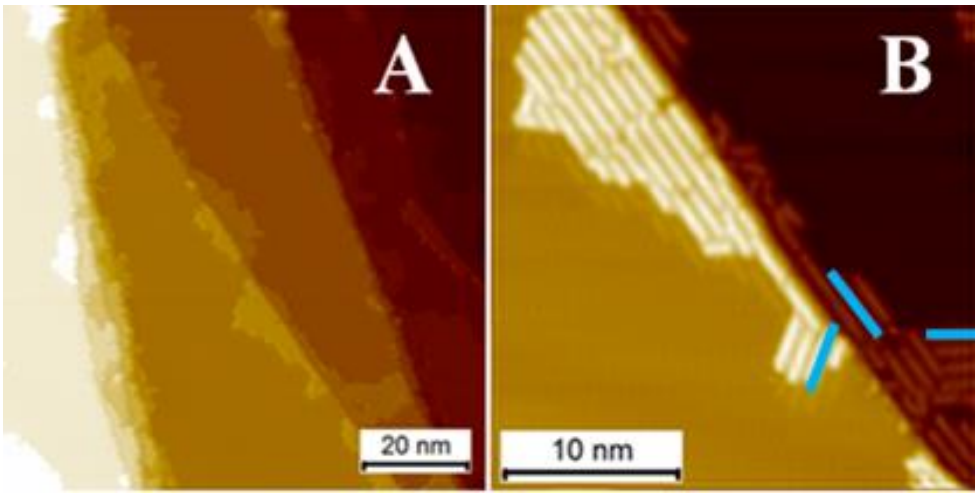


**Figure 2.** STM image of oligothiophenes adsorbed on Ag(111) after annealing the terthiophene monolayer at~600 K. (A)Large-scale $(93\ nm)^2$ STM image, acquired at 10 pA with -1 V bias at 131 K. (B)Small-scale $(27.9\ nm)^2$ STM image, acquired at 10 pA with -1 V bias at 131 K. (Three oligomers in equivalent crystallographic directions are labeled by blue lines.)

To quantify the decomposition and polymerization due to the annealing process, we measured the length distribution after annealing as shown in Figure 3. Before annealing we observed essentially 100% terthiophene on the surface as indicated in Figure 1. After annealing we observed a total 530 oligomers over several different local regions on the surface. Nearly one third of all these were still terthiophenes (3T), and a range of longer thiophene oligomers were also seen, including quaterthiophene (4T), sexithiophene (6T) and heptathiophene (7T) and longer oligomers.

The distribution of lengths in Figure 3 allows insights into the mechanism of oligomerization on the surface. In particular, the appearance of 2T indicates decomposition

of 3T or other oligomers during annealing. Furthermore, the presence of oligomers that are not multiples of 3T also shows that the reaction does not occur by simple fusion of pre-existing surface-bound 3T reactants. Finally, the absence of single thiophene monomers suggests that this small molecule has strong tendency to desorb from the surface, consistent with previous temperature-programmed desorption measurements that show desorption of thiophene from Ag(111) is complete above 250 K.[10]

The most important process occurring during annealing may therefore be summarized as follows. Terthiophene decomposes to yield a population of thiophene monomers. These have a high probability to desorb thermally from the surface. Nevertheless, the thiophene monomers have an enhanced residence time near step edges[23] that leads to the possibility of reaction with other monomers to re-form thiophene oligomers in these local regions. If sufficiently long oligomers form (see discussion below), they are stabilized on the surface even at elevated temperatures. Otherwise shorter oligomers may continue to undergo thermal decomposition followed by desorption or surface reaction.

We focus now on quantifying the thiophene oligomerization using the length distribution in Fig. 3. Under the assumption of a fixed rate of this process, the observed decay in number of longer thiophenes with increasing length is expected based on simple considerations of Flory-Schulz type polymerization reaction kinetics.[24] In fact, a reasonable fit ($\chi^2/\nu$=1.76793 and $R^2$=0.93105) to the Flory-Schulz distribution can be made as shown in Figure 3, if we hypothesize that the "monomers" are simple thiophenes (1T) dissociated from 3T. This distribution is given by

$$N_x=N_0(1-p)^2p^{x-1}$$

where $N_x$ is the number of "x-mer" molecules composed of x monomers, $N_0$ denotes the total number of initial monomers, p is called the extent of reaction, indicating the fraction of monomers which have reacted. The fit to this model is only good for oligomers of 6T and longer. We attribute this fact to the result of the unknown contribution of non-dissociated starting material (3T) and competitive dissociation and desorption of smaller thiophenes mentioned above. As a result of this competition, the only lengths in the distribution in figure 3 that arise solely from oligomerization are those longer than 5T.

The fit to the Flory-Schulz distribution is consistent with a reaction mechanism in which the Ag surface catalyzes dehydrogenation of 2 positions on the thiophene molecules and oligomerization proceeds *via* condensation. From the Flory-Schulz fit for this process, the total number of initial monomers $N_0=5553\pm1153$ and the extent of reaction is $p=0.55\pm0.02$, indicating approximately half of the thiophenes created by decomposition of 3T subsequently polymerizes to longer oligomers.

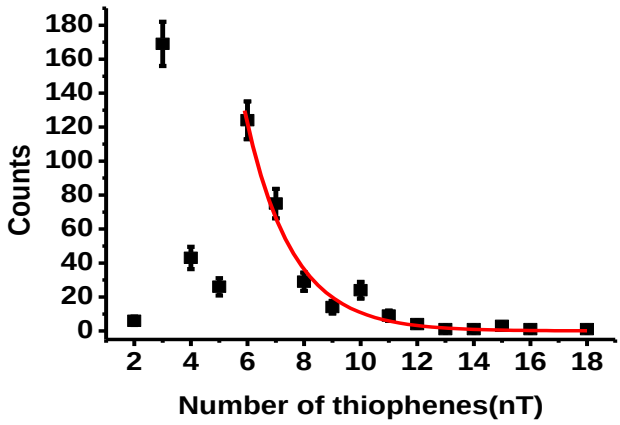


**Figure 3.** Histogram of the number of monomer units in different thiophene oligomers after the 600 K annealing process. The solid red line is a fit to the Flory-Schulz distribution for oligomers longer than 5T.

In conclusion, we report STM observations showing surface-controlled thermal oligomerization of terthiophene on Ag(111). Annealing a uniform terthiphene overlayer on Ag(111) induces a combination of desorption, dissociation, and oligomerization that results in a distribution of long-chain thiophenes (up to 18T) on the surface. The chain directions follow the 3 equivalent close-packed Ag atom directions on the surface, suggesting Ag as an important substrate for epitaxial control of thiophene oligomerization.

## AUTHOR INFORMATION

**Corresponding Author**

*Email:Dan_Dougherty@ncsu.edu

**Notes**

The authors declare no competing financial interests.

## ACKNOWLEDGMENT

We acknowledge useful discussions with professors D.A. Shultz and H.W. Ade. This work was supported by an NSF CAREER grant: CHE -1056861

REFERENCES

(1) Forrest, S. R. *Nature* **2004**, *428*, 911.

(2) Blanchet, G.; Rogers, J. *J. Imaging Sci. Technol.* **2003**, *47*, 296.

(3) Sun, J.; Zhang, B.; Katz, H. E. *Adv. Funct. Mater.* **2011**, *21*, 29.

(4) Sheats, J. R. *J. Mater. Res.* **2004**, *19*, 1974.

(5) Tashiro, K.; Ono, K.; Minagawa, Y.; Kobayashi, M.; Kawai, T.; Yoshino, K. *J. Polym. Sci., Part B: Polym. Phys.* **1991**, *29*, 1223.

(6) Suzuki, A. *J. Organomet. Chem.* **1999**, *576*, 147.

(7) Stille, J. K. *Angew.Chem.Int.Ed.Engl.* **1986**, *25*, 508.

(8) Compagnini, G.; De Bonis, A.; Cataliotti, R. S.; Marletta, G.*Phys.Chem.Chem.Phys.* **2000**, *2*, 5298.

(9) Alaverdyan, Y.; Johansson, P.; Kall, M. *Phys.Chem.Chem.Phys.* **2006**, *8*, 1445.

(10) Väterlein, P.; Schmelzer, M.; Taborski, J.; Krause, T.; Viczian, F.; Bäßler, M.; Fink, R.; Umbach, E.; Wurth, W. *Surf. Sci.* **2000**, *452*, 20.

(11) Hla, S.-W.; Bartels, L.; Meyer, G.; Rieder, K.-H. *Phys. Rev. Lett.* **2000**, *85*, 2777.

(12) Ho, W. *J.Chem.Phys.* **2002**, *117*, 11033.

(13) Lipton-Duffin, J.; Miwa, J.; Kondratenko, M.; Cicoira, F.; Sumpter, B.; Meunier, V.; Perepichka, D.; Rosei, F. *PNAS* **2010**, *107*, 11200.

(14) Lin, T.; Shang, X. S.; Adisoejoso, J.; Liu, P. N.; Lin, N. *in press J.Am.Chem.Soc.*,DOI: 10.1021/ja311890n.

(15) Cai, J.; Ruffieux, P.; Jaafar, R.; Bieri, M.; Braun, T.; Blankenburg, S.; Muoth, M.; Seitsonen, A. P.; Saleh, M.; Feng, X.; Mullen, K.; Fasel, R. *Nature* **2010**, *466*, 470.

(16) Wang, Z.; Pronschinske, A.; Dougherty, D. B. *Org. Electron.* **2011**, *12*, 1920.

(17) Lin, R.; Galili, M.; Quaade, U. J.; Brandbyge, M.; Bjornholm, T.; Esposti, A. D.; Biscarini, F.; Stokbro, K. *J.Chem.Phys.* **2002**, *117*, 321.

(18) Diaz-Quijada, G. A.; Weinberg, N.; Holdcroft, S.; Pinto, B. M. *J.Chem.Phys. A* **2001**, *106*, 1266.

(19) Stecher, R.; Drewnick, F.; Gompf, B. *Langmuir* **1999**, *15*, 6490.

(20) Azumi, R.; Mena-Osteritz, E.; Boese, R.; Benet-Buchholz, J.; Bauerle, P. *J. Mater. Chem.* **2006**, *16*, 728.

(21) Glowatzki, H.; Duhm, S.; Braun, K. F.; Rabe, J. P.; Koch, N. *Phys.Rev. B* **2007**, *76*, 125425.

(22) Chen, L.-g.; Zhang, C.; Zhang, R.; Dong, Z.-c. *Chin. J. Chem. Phys.* **2012**, *24*, 659.

(23) Chen, X.; Frank, E. R.; Hamers, R. J. *J.Vac.Sci.Tech.B* **1996**, *14*, 1136.

(24) Flory, P.J. *J.Am.Chem.Soc.* **1936,** 58,1877.